Experimentation, Modeling, and Optimization Studies on Forward Osmosis and Pressure Retarded Osmosis Processes

A thesis submitted in partial fulfilment of the requirements for the degree of

DOCTOR OF PHILOSOPHY

by

HABTOM TEKLU ASEFFA

ROLL No.: 156107036

Department of Chemical Engineering

Indian Institute of Technology,

Guwahati-781039, Assam, India

June 2021

DEDICATION

This Thesis is Dedicated to My Late Father Mr. Teklu Aseffa Hagos

--- Your advice will be there forever ---

Department of Chemical Engineering
Indian Institute of Technology,
Guwahati-781039, India

STATEMENT

This is to certify that I have carried out all the research work in this thesis entitled "**Experimentation, Modeling, and Optimization Studies on Forward Osmosis and Pressure Retarded Osmosis Processes**", at the Department of Chemical Engineering, Indian Institute of Technology Guwahati, under the supervision of Prof**. Senthilmurugan Subbiah**. The results documented in this thesis are achieved by me and have not been submitted to any other University or Institute for the award of any degree or diploma.

In keeping with the general practice of reporting scientific observation, due acknowledgement has been made wherever the work described is based on the findings of other investigations.

Habtom Teklu Aseffa

Roll No.: 156107036

Department of Chemical Engineering

Indian Institute of Technology

Guwahati-781039, Assam, India

June 2021

Department of Chemical Engineering

Indian Institute of Technology,

Guwahati-781039, India

CERTIFICATE

This is to certify that the work contained in this thesis entitled "**Experimentation, Modeling, and Optimization Studies on Forward Osmosis and Pressure Retarded Osmosis Processes**" being submitted by **Mr. Habtom Teklu Aseffa** (Roll No. 156107036) for the award of Ph.D. degree, is a record of bonafide research carried out by him at Department of Chemical Engineering, Indian Institute of Technology Guwahati, under my guidance and supervision. The work documented in this thesis has not been submitted to any other University or Institute for the award of any degree or diploma.

Digitally signed by Prof. Senthilmurugan Subbiah
DN: cn=Prof. Senthilmurugan Subbiah, o=IIT Guwahati, ou=Department of Chemical Engineering, email=senthilmurugan@iitg.ac.in, c=IN
Date: 2021.06.14 11:03:10 +05'30'

Date: June 2021

(Signature of Thesis Supervisor)

Prof. Senthilmurugan Subbiah

Department of Chemical Engineering

Indian Institute of Technology Guwahati

Guwahati-781039, Assam, India

ACKNOWLEDGMENTS

At foremost, I would like to express my sincere and heartfelt gratitude to my supervisor **Prof. Senthilmurugan Subbiah** for his invaluable guidance, continuous support, motivation, kindness, and patience with me. His advice helped me in all the ways of doing research and writing this thesis. His preplanning nature in completing the experiments, data analysis, writing manuscripts, and thesis within the stipulated period helped me a lot in completing my research work. He provided me enough facilities that I needed for my research works towards the successful completion of my thesis work. He trained me much to handle any kind of critical situation in my life. I could not imagine having a better person than him for my stay at IIT Guwahati.

I am grateful to **Prof. Uppaluri Ramgopal V.S,** chair of my doctorial committee, **Prof. Mohanty Kaustubha,** and **Dr. Senthilkumar S.,** members of my doctorial committee, for continually reviewing the progress of my research work with their valuable comments and suggestions towards improving the quality of my research work.

I wish to express my sincere thanks to all the faculty members and technical staff in the Department of Chemical Engineering for their kind help to carry out the experiments throughout the research time. Also, Alumni of External Affairs of IIT Guwahati for their help regarding visa and related issues.

I want to express my sincere gratefulness to Wachemo University collaborating with the Ministry of Education, Government of Ethiopia, for their constant Ph.D. scholarship support.

I would like to thank Mr. **Dinesh Kumar Gautam** for helping me through all my experimental, coding and paper writing times. He is really a good guy with good hearts. Thank you mate!

I would like to thank my lab mates Mrs. Aanisha Akhtar, Miss. Nivedhitha Swaminathan, Miss. Neelam Dutta, Miss. Ananya Bardhan, Miss. Seema Bharati, Dr. Vishal Kumar Verma, Dr. Vigneshwaren K., Dr. Arunkumar Chandrasekaran, Mr. Senthil Selva, Mr. Viswanth Ramba, Mr. Munubarthi Kranthi Kumar, Mr. Muniraja Tippa, Mr. Pryemjeet Deka, Mr. Balakumara Vignesh, Mr. Naveen Kumar Yarnal,

Mr. Bharat S. Rajput, Mr. Banajit Saloi and Mr. Vishnu for their friendly support and timely assistance whenever needed.

I would like to acknowledge my Ethiopian friends; Mr. Mesfin Ashebir, Mr. Henok Lemma, Mr. Henok Tesfaye, Mr. Henok Adnew, Dr. Ali Shemsedin, Mr. Andualem Tsegaye, Mr. Sileshi Bekele, Mr. Dawit Mekonnen and Mr. Tarikayehu Amanuel, for your encouragement at different stages of my work.

Last but not least, I would like to thank my family: my beloved parents Mr. Teklu Aseffa and Mrs. Shewaye Tiku, my sister Mrs. Eyerusalem Teklu, my brothers Mr. Kibrom Teklu, Mr. Meried Teklu, Mr. Dawit Teklu and Mr. Tesfu Teklu for supporting and encouraging me throughout my thesis and my life in general. I especially thank my late father, Mr. Teklu Aseffa as my role model and as my best friend, for inspiring and encouraging me to do hard work. He taught me about life by his examples, through his courage, and his strength taught me to have faith in myself. I also do not have words to express my mother, Mrs. Shewaye Tiku, for being there no matter the situation is. Without her, I might not be the person I am today.

Finally, I express my sincere thanks to all who helped me in all the forms during my stay at IIT Guwahati and the successful completion of this thesis.

Sincerely,

Habtom Teklu Aseffa

June 2021

Abstract

As per the "United Nations World Water Development Report 2019", the global water demand is increasing by about 1% every year since the 1980s. And this global water demand rate is expected to continue until 2050. The global water demand increment might be due to a combination of dramatic population and economic growth. Unless an alternative method of producing clean water from the seawater and wastewater comes to picture, over 6 billion people will suffer from clean water scarcity by 2050. In addition, the global energy demand had increased by 0.9% in 2019, which is 40% the rate of growth observed in 2018. This unfortunate reduction in the energy demand was due to slower economic growth and weather conditions which were felt across many countries. However, the average energy demand since 2011 was 1.28%. Various researchers are working on alternative sources such as renewable sources to meet global water and energy demand.

Production of clean water and energy from renewable sources via an innovative technology is very important to minimize the freshwater usage and greenhouse effect. Considering the recent innovations in membrane development activities, membrane technologies such as forward osmosis (FO) and pressure-retarded osmosis (PRO) are becoming exceptional and emerging technologies. Though in the last two decades, many researchers are engaged in improving the membranes and membrane processes, still, the outputs related to the production of clean water and energy are not satisfactory. Therefore, the work in this thesis focuses on the performance evaluation of the existing FO/PRO process and development of a mathematical model that accurately replicates the actual FO/PRO process. The former reduces the effect of experimental uncertainty on the FO/PRO processes, and the latter helps to get an optimal result from the FO/PRO processes through simulation and optimization studies.

The first stage of the research focused on analyzing the errors in membrane characterization experiments due to the experimental uncertainties such as water evaporation, variation in solution volume and concentration, for low and high flux FO membranes is presented in this thesis. For the low flux FO membrane, various experiments are performed in this work, and for the high flux FO membrane, the experimental data are simulated using the parameters adopted from literature. The water evaporation from the solution tank is measured

experimentally and incorporated in the tank mass balance equation. The unsteady state mathematical model of the FO test cell is developed by combining unsteady state tank mass balance, steady-state membrane transport, and concentration polarization. For the case where the water evaporation was not considered, the maximum error in water flux (J_W) was found to be 744 %. The steady-state based model parameters were also found to have maximum deviations of 390.5 and 6.9 % in the solvent and solute permeability, respectively, compared to the parameters estimated using the unsteady state model in the presence of water evaporation. The mass and concentration variations based on the proposed model were 3.7 and 5.7 %, respectively.

In the next stage of the research, since the design and optimization of the FO module is a promising aspect in improving the performance of commercial hollow fiber (HF) FO modules, it is necessary to predict the performance using a well-defined mathematical model. However, developing the precise model to describe all phenomena occurring during the FO process is one of the major challenges. In this thesis, a mathematical model was developed for the axial flow HF FO module and validated with unsteady-state FO experimental data of sodium chloride - water system. Membrane parameters estimation followed by simulation at various module length and operating condition were made. A maximum of 0.7 and 12% deviation in draw solution (DS) and feed solution (FS) concentration shows a good agreement between experimental results and model outputs. Simulations were carried out at various module length and operating conditions to analyze their effects on permeate flow rate and power consumption. Based on the simulation results, a multi-objective optimization (MOO) was formulated to get optimal Pareto between FO water flux and power supplied to the pump by considering the module length, DS and FS pressure, and flow rate as decision variables. The optimization analysis revealed the exponential behaviour of power consumption with respect to the permeate flow rate. Finally, a procedure to optimize the FO plant performance using MOO optimal Pareto is presented.

In the final stage of this research, energy production estimation using the axial flow HF FO module for the PRO process is presented in this study. The combination of long coastline (about 7500 km) and abundant river water (9.76 x 10^{11} m^3/year) flowing into the sea across the southern peninsula of the Indian sub-continent provides the best and suitable conditions for blue energy extraction. This study is aimed to calculate the Indian blue energy potential

by mixing Indian river water and seawater before discharging into the sea through the optimized PRO process. Further, the model-based optimization approach is solved to establish an optimal process condition for integrated PRO + ERD (energy recovery device) process with respect to actual Indian river and seawater salinity. The PRO experiments are performed using syntactic seawater and river water as a DS and FS, respectively. The PRO model proposed in this work is validated with experimental data generated from the commercial PRO module. The PRO process optimization strategy is proposed to maximize the net power produced from the PRO process by manipulating operating conditions (such as flow rate and pressure to the PRO system) and module length. Three different objective functions are evaluated to maximize the extraction of the blue energy generation. The optimized PRO process was able to generate a net power of 0.07 kWh per 1 m^3 of river water supplied to the PRO system. The estimated blue energy generation from the Indian major rivers discharging along the Indian coastal area is 12.34 TWh/year, which is equal to 4.72 % of the Indian renewable power generation capacity during the 2018-19 fiscal year, i.e., 261.7 TWh/year.

Table of Contents

List of Figures

List of Tables

List of Abbreviations and Symbols

abs. : Absence

ALDS : Active layer facing draw solution

ALFS : Active layer facing feed solution

CECP : Concentrative external concentration polarisation

CICP : Concentrative Internal Concentration Polarization

Conc. : Concentration

CP : Concentration Polarisation

CTA : Cellulose triacetate

DECP : Dilutive External Concentration Polarization

DI : De-Ionized water

DICP : Dilutive Internal Concentration Polarisation

DS : Draw Solution

ECP : External Concentration Polarisation

ERD : Energy Recovery Device

evap. : Evaporation

FCP : Friction Concentration Polarization

FO : Forward Osmosis

FS : Feed Solution

GA : Genetic Algorithm

HF : Hollow Fiber

HP_{factor} : Hagen-Poiseuille correction factor

ICP	: Internal Concentration Polarisation
ID	: Inner Diameter
MD	: Membrane Distillation
MOO	: Multi-Objective Optimization
NF	: Nano-filtration
OD	: Outer Diameter
ODMP	: Osmotically Driven Membrane Process
pres.	: Presence
PAO	: Pressure Assisted Osmosis
PRO	: Pressure Retarded Osmosis
PX	: Pressure Exchanger
Re	: Reynolds number
RED	: Reverse electro-dialysis
RO	: Reverse Osmosis
RSD	: Reverse Solute Diffusion
Sc	: Schmidt number
SD	: Solution Diffusion
SEC	: Specific Energy Consumption
SEM	: Scanning Electron Microscopy
Sh	: Sherwood number
SK	: Spiegler – Kedem
SW	: Spiral Wound
SWRO	: Seawater Reverse Osmosis

TEM : Transmission Electron Microscopy

TFC : Thin-film Composite

TWh : Tera Watt hour

UF : Ultra-filtration

Nomenclature

A_M : Membrane surface area (m^2)

A : Water permeability coefficient ($m^3/(m^2\ s\ Pa)$)

$A_{FS\text{-}Air}$: Feed solution surface area in contact with the Air (m^2)

$A_{DS\text{-}Air}$: Draw solution surface area in contact with the Air (m^2)

B : Solute permeability coefficient ($m^3/(m^2\ s)$)

b : Van't Hoff osmotic coefficient (m^4/s^2)

b_0 : Y-intercept for concentration Vs. solute permeability plot ($m^3/(m^2\ s)$)

C : Concentration (kg/m^3)

C* : Critical concentration (kg/m^3)

$Cost_P$: Cost of permeate per unit volume ($/L)

$Cost_{energy}$: Cost of energy per kwh ($/kwh)

D_{diff} : Diffusivity coefficient (m^2/s)

D_f : Darcy's law constant in feed side

$d_{i,fiber}$: Inner diameter of hollow fiber (m)

$d_{o,fiber}$: Outside diameter of hollow fiber (m)

D_s : Solute diffusivity (m^2/s)

E_{DS} : Rate of evaporation loss from DS ($kg/(m^2\ s)$)

E_{FS} : Rate of evaporation loss from FS ($kg/(m^2\ s)$)

e_1 : Ergun constant for viscous term

e_2 : Ergun constant for kinetic term

F^* : Parameter which depends on water flux (-)

H : Channel Height (m)

J_S : Solute flux (kg/(m^2 s))

J_W : Water flux (m^3/(m^2 s))

k : Mass transfer coefficient (m/s)

K : Solute resistivity (s/m)

k_a, k_b : Mass transfer coefficient correlation constants (-)

L : Channel length or Module length (m)

Lp : Water permeability coefficient (m^3/(m^2 s Pa))

M : Mass (kg)

M_W : Molecular weight (kg/kmol)

m : Slope of solute permeability before critical concentration (m^4/(s kg))

P : Pressure (Pa)

Pw_{inp} : Input Power (watt)

Pow : Power produced from PRO (watt)

Q : Flow rate (L/h)

R : Gas constant (m^3 Pa)/(K mol))

S : Structural parameter (m)

SEC : Specific Energy consumption (MJ/m^3)

t : Time (s)

t_S : Support layer thickness (m)

T	: Temperature (K)
T_{DS}	: Draw solution temperature (K)
T_{FS}	: Feed solution temperature (K)
V_{DS}	: Volume of draw solution (m^3)
V_{FS}	: Volume of feed solution (m^3)
u	: Velocity (m/s)
x,y	: Constants in mass transfer coefficient equation
z	: Coordinate in the axial direction of the hollow fiber module, m

Greek

α, β, γ	: Mass transfer coefficient correlation constants (-)
ρ	: Density (kg/m^3)
ε	: Porosity (-)
Φ	: Concentration polarization constant (-)
λ	: Flow rate ratio between ERD and HF PRO module (-)
Π	: Osmotic pressure (Pa)
σ	: Reflection coefficient (-)
τ	: Tortuosity of support layer (-)
μ	: Viscosity (Pa s)
ν	: Van't Hoff factor (-)

Superscript

b	: Bulk phase
DS	: Draw solution
DS-FS	: Difference between DS and FS

DS,inlet	: Inlet draw solution
DS,outlet	: Outlet draw solution
fiber	: Hollow fiber
Final	: Final condition
FS	: Feed solution
FS,inlet	: Inlet feed solution
FS,outlet	: Outlet feed solution
Initial	: Initial condition
inp	: Input
lumen	: Lumen side
m	: Membrane surface
P	: permeate
p	: Porous support layer
shell	: Shell side

Chapter 1 Introduction

Backgrounds, Motivation, Objectives, and Organization of the Thesis

This chapter presents the background related to osmotically driven membrane processes. Followed by the motivation section, which will cover a brief summary about the reasons behind (i) studying the uncertainty analysis during membrane characterization techniques, and (ii) developing a mathematical model for axial flow hollow fiber (HF) forward osmosis (FO), and pressure retarded osmosis (PRO) module. Studying the experimental uncertainties is very important while designing large-scale FO/PRO processes, as it reduces the error in the estimated membrane transport parameters. Developing a mathematical model is crucial to evaluate the performance of commercially available FO/PRO modules. It also plays a vital role in getting an optimal result from the FO/PRO processes through simulation and optimization studies. Moreover, the PRO study is used to estimate the blue energy potential that can be generated by mixing Indian river water into the seawater through an optimized PRO process. In this chapter, the objectives and scope of the thesis are also framed. Finally, the organizations of the thesis are highlighted.

1.1 Introduction to Membrane Processes

1.1.1 Definition of Membrane

Membrane is one of the separation techniques which stops ions, molecules, solute, etc. while allowing other substances (for example, water) to pass through it. As depicted in Figure 1-1, the solution which is going to be separated is called a feed. The substances that are stopped by the membrane are called a reject and pass through the membrane are called a permeate.

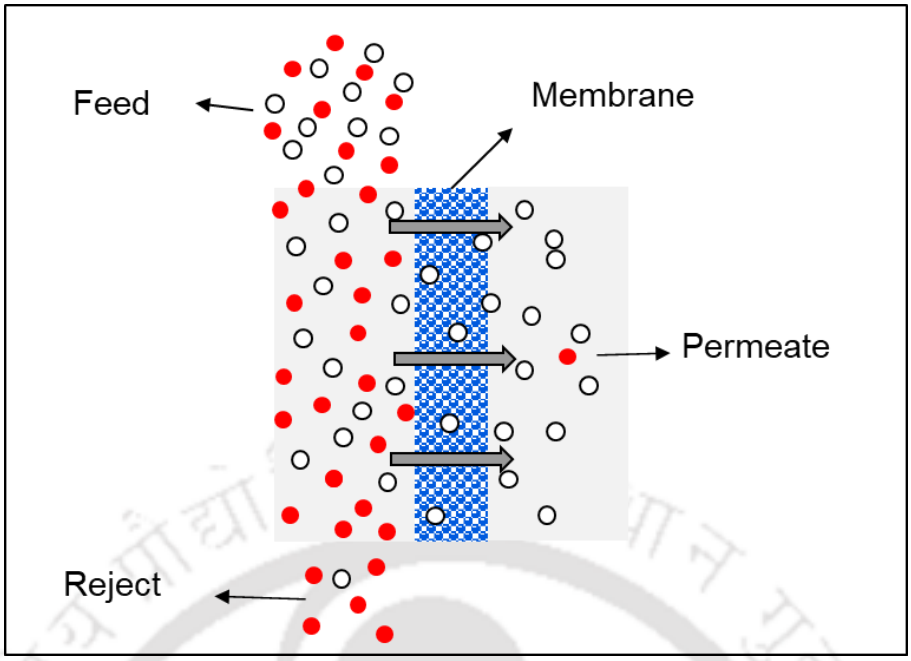

Figure 1-1. Separation of the feed solution using membrane

1.1.2 Classification of Membrane Process

Membrane processes can be classified into the following four categories based on the driving force used for the separation.

1. Pressure-driven processes (microfiltration, ultrafiltration, reverse osmosis, etc.)
2. Temperature-driven processes (membrane distillation, thermo-osmosis, etc.)
3. Concentration-driven processes (forward osmosis, pressure retarded osmosis, etc.)
4. Electrical potential driven processes (electrodialysis, electro-filtration, etc.)

In this study, we are going to focus on concentration-driven membrane processes. In various literature [1–8], the concentration-driven processes are commonly referred

as osmotically driven membrane processes. The detail about the osmotically driven membrane processes will be discussed in the subsequent sections.

1.2 Introduction to Osmotic Driven Membrane Processes

1.2.1 Definition of Osmotic Driven Membrane Processes

The idea of osmotically-driven membrane processes (ODMPs) comes from the so-called osmosis process. The osmosis process is the movement of water from a low concentrated solution (for example, freshwater) to a highly concentrated solution (for example, salt water). In ODMPs, we commonly use the term "feed solution (FS)" to represent the less concentrated solution and "draw solution (DS)" to represent the highly concentrated solution. Therefore, in ODMPs, the movement of water will be from the FS to the DS side. Osmotically-driven membrane processes are among the emerging membrane technologies that showed great promise to address the global challenges in desalination, water treatment, and energy generation [9–12].

1.2.2 Classification of Osmotic Driven Membrane Processes

Osmotically-driven membrane processes can be classified into three, namely i) Forward osmosis (FO), ii) Pressure assisted osmosis (PAO), and iii) Pressure retarded osmosis (PRO). The basic difference lies in the driving force they possess, as shown in Figure 1-2. In FO, the driving force is the osmotic pressure (ΔΠ) gradient between the draw and feed solution as shown in Figure 1-2 (a). The osmotic pressure can be calculated using Eq. 1

$$\Delta\Pi = \frac{iRT}{M_W}\left(C_{DS,m} - C_{FS,m}\right) \tag{1.1}$$

Where i, R, T, and M_W are ionization number of the salt (-), universal gas constant in [(m^3 Pa)/(mol K)], the temperature of the solution in [°K], and molecular weight of DS in [g/mol], respectively. $C_{DS,m}$ and $C_{FS,m}$ are the concentration of DS and FS at the membrane surface in [kg/m^3], respectively.

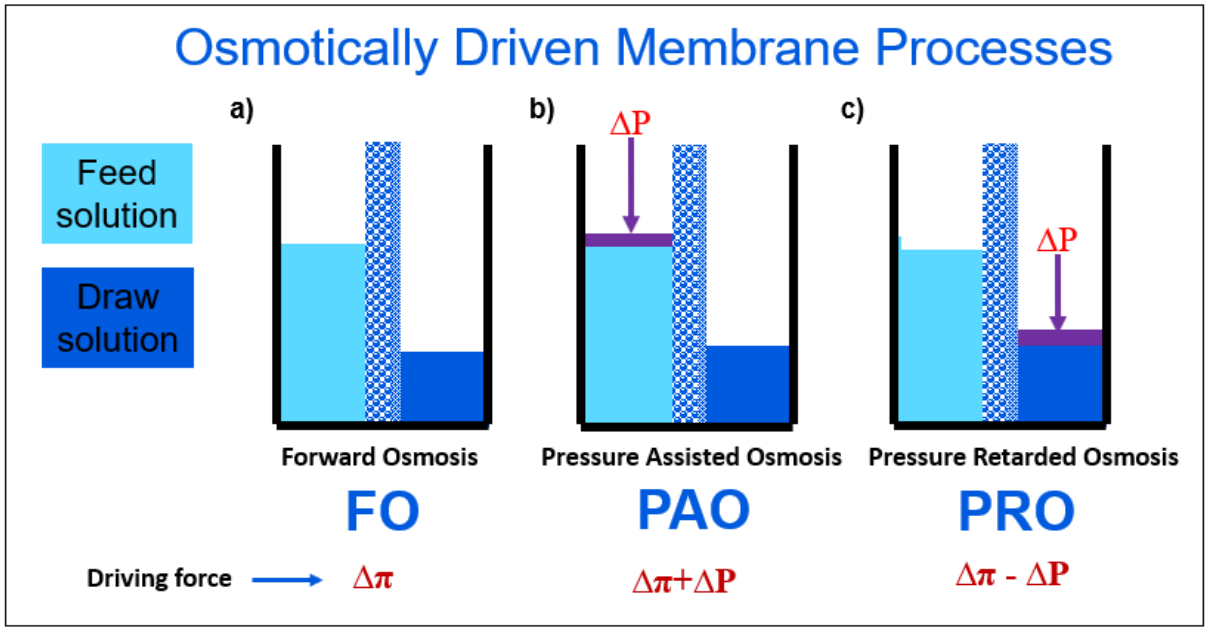

Figure 1-2. Classification of osmotically driven membrane processes a) forward osmosis, b) pressure assisted osmosis, and c) pressure retarded osmosis

In PAO, the osmotic pressure (ΔΠ) gradient will be assisted by the external pressure (ΔP) applied on the FS side. Hence the total driving force will be ΔΠ + ΔP as shown in Figure 1-2 (b). Whereas in PRO, the osmotic pressure gradient will be retarded by the external pressure applied in the DS side (refer to Figure 1-2 (c)). Hence the net driving force will be ΔΠ - ΔP. The detailed explanation for each ODMPs will be covered in the next sub-sections.

1.2.2.1 Forward Osmosis (FO) Process

Forward osmosis process is a natural transport of water from a low concentrated side (feed solution) to a high concentrated side (draw solution) through a semipermeable barrier called membrane. FO process is a membrane-based phenomenon which occurs naturally when two solutions with different concentration are present on either side of the semi-permeable membrane. The membrane selectively passes the solvent while retaining the solute [13]. Unlike the pressure-driven processes such as reverse osmosis (RO), which requires external pressure for the process to happen, FO processes are spontaneous processes. It uses the advantage of high osmotic pressure present in the DS to draw the water from the FS to the DS side [14]. The schematic diagram that represents the FO process is depicted in Figure 1-3.

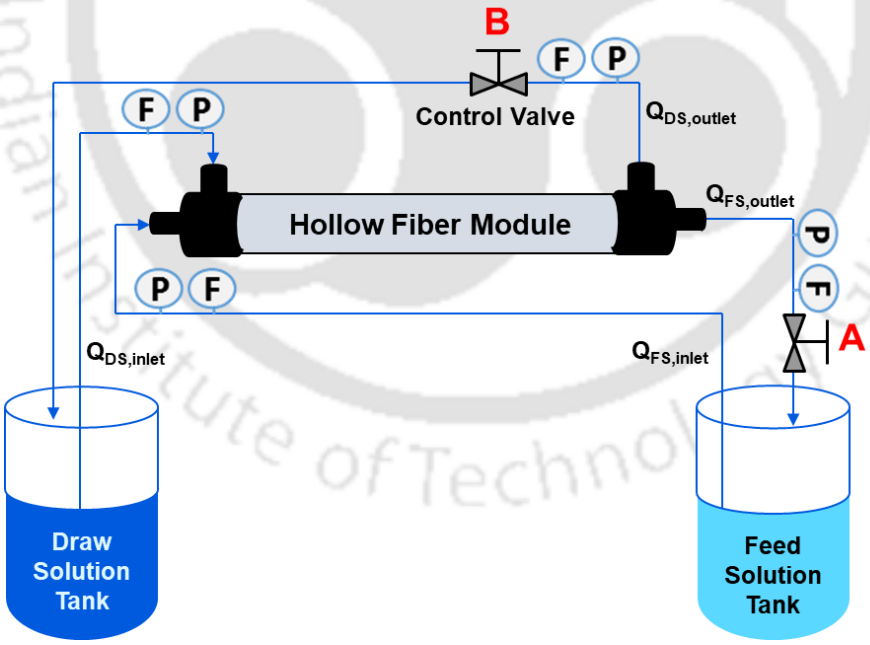

Figure 1-3. Schematic diagram for forward osmosis (FO), pressure-assisted osmosis (PAO), and pressure retarded osmosis (PRO) processes

1.2.2.2 Pressure Assisted Osmosis (PAO) Processes

In this process, the natural movement of water from the FS side to DS side will be assisted by applying external hydraulic pressure on the FS side. Since this process assists the natural water movement from the FS to the DS side, it is called pressure-assisted osmosis. In order to pressurize the FS side to the desired value, the control valve present on the FS outlet side will be slightly closed until the pressure in the FS stream reached the desired pressure value, as shown in Figure 1-3, i.e., A will be partially closed while B is fully opened.

1.2.2.3 Pressure Retarded Osmosis (PRO) Process

In the PRO process, the chemical potential is converted into hydraulic energy as water transport through the membrane from FS to the pressurized DS side. Unlike the FO process, a hydraulic pressure that is lower than the osmotic pressure difference between the FS and DS will be applied on the DS side (B will be partially closed while A is fully opened (Figure 1-3)). Since the hydraulic pressure "retards" the water permeation from FS into DS, this process is known as pressure retarded osmosis [15]. The hydraulic energy is then converted into electrical energy while passing part of the high-pressure draw solution through the turbine, as depicted in Figure 1-4 [16]. The remaining portion of the high-pressure draw solution is used in an energy recovery device called a pressure exchanger. The pressure exchanger transfers this high-pressure energy back to the incoming low-pressure draw solution. The availability of energy-efficient pressure exchangers is one of the main advantages for the PRO process to operate economically for power generation [15,17].

The maximum hydraulic pressure that can be applied for the PRO case will be dependent on the osmotic pressure difference between the DS and FS. It can be calculated using the water flow mathematical expression through the membrane.

$$J_W = A(\Delta\Pi - \Delta P) \quad (1.2)$$

where Jw is the water flux (m^3/m^2 s), and A is the water permeability coefficient of the membrane (m^3/m^2 s bar). ΔΠ and ΔP are the osmotic and hydraulic pressure (bar), respectively. The power generation from the PRO process sometimes quantifies using the power density (W), which is the power generated per unit membrane area (W/m^2). It can be mathematically expressed as

$$W = J_W \Delta P \quad (1.3)$$

$$W = J_W \Delta P = A(\Delta\Pi - \Delta P)\Delta P \quad (1.4)$$

Hence, to estimate the optimum hydraulic pressure that should be applied on the DS side, the power density should be maximized. Differentiating the power density with respect to ΔP and equating it to zero gives ΔP = ΔΠ/2. Therefore, the hydraulic pressure has to increase up to half of the osmotic difference between the DS and FS. Further increase in the external pressure leads to a reduction in power generation.

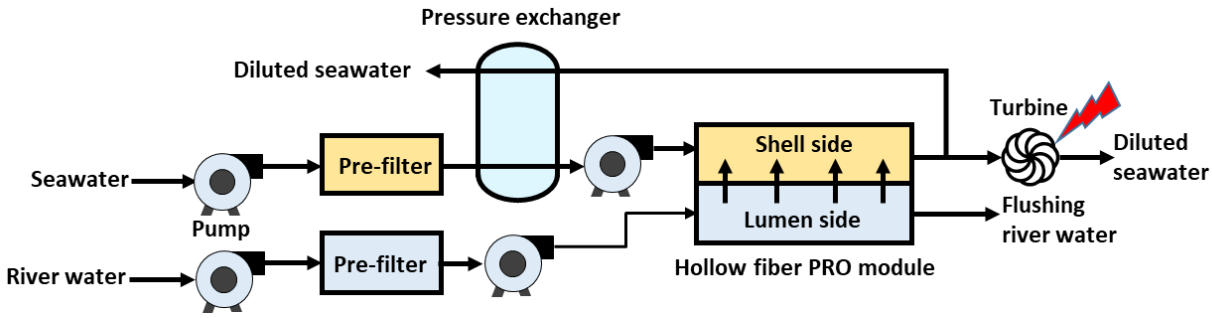

Figure 1-4. Power generation using PRO process

1.3 Background

The development of energy-efficient FO/PRO-based hybrid technology can enable the co-production of both clean energy and fresh water by using wastewater and renewable energy as a source. Such technology will minimize fresh water usage and the greenhouse effect [11]. Considering the recent innovations in membrane development activities, membrane technologies made of FO, PRO, reverse osmosis (RO), nanofiltration (NF), and membrane distillation (MD) are becoming exceptional and emerging technologies. They are proven to produce both clean water and energy while mixing saline water and freshwater/pre-treated wastewater through the PRO/FO process. The main advantages of FO over pressure-driven processes such as RO are that it has low membrane fouling tendency, high solute rejection, and operates at low hydraulic pressure [18]. The low fouling tendency requires minimum pre-treatment of feed solution (FS). Thus, a simple process like osmotic backwash (by interchanging the draw solution (DS) and FS side) or periodic chemical cleaning can be applied for the membrane regeneration [18]. In recent years, membrane fouling in the FO has been proven to be highly reversible [19,20] and can be quickly diminished by optimizing the FO operating conditions [21]. Moreover, the advantage of operating at low pressure significantly simplifies the design and selection of the equipment. The FO process also requires less pumping energy, mainly for solution circulation. However, in RO-FO combined process, a large amount of energy is consumed during the draw solution re-concentration process

[18]. Therefore, the FO recovery is constrained by DS concentration and its regeneration potential [6,22,23].

Considering the above-listed advantages, researchers have identified FO as a promising alternative technology to overcome technical bottlenecks of the RO process [24]. As a result of continuous research, FO has found different applications in pharmaceutical and liquid food processing [25,26], industrial and domestic wastewater treatment [9,27,28], seawater desalination and reclamation [9,28,29], osmotic membrane bioreactors [18], and water purification in emergency aid circumstances [30].

The design and optimization of the osmotically driven processes for the actual capacity plant require membrane transport parameters such as water permeability, solute permeability, and structural parameter. These parameters can be estimated by adopting appropriate experimental and theoretical techniques. Most studies reported that the solution concentration is assumed either the initial concentration or average of initial and final concentrations while estimating the membrane transport parameters using test cell experiments. Particularly in batch osmotic driven membrane process (FO/PRO), the solute concentration in DS and FS is expected to vary during the membrane characterization experiment [31]. The reasons might be due to

i) Water flux (J_W) from FS to DS that leads to dilution in DS and concentration in FS,
ii) Reverse solute flux (J_S) from DS to FS that leads to further dilution in DS and concentration in FS, and
iii) Water evaporation from DS and FS tank, if it is exposed to open environment.

The experimental data without incorporating the factors mentioned above might lead to errors in estimated membrane transport parameters. The error on the estimated membrane transport parameters might be reduced if the experimental data includes the water evaporation rate and the dynamic nature of the concentration while calculating the water and solute fluxes. Therefore, quantification of the error

in the estimated membrane transport parameter due to the above-mentioned experimental uncertainties is very much helpful while designing large-scale osmotic driven processes.

In the case of the high-capacity membrane module, the membrane can be characterized by using both continuous and batch experimental data. Both approaches have their own merits and demerits; for example, the continuous experiment requires continuous recycling of DS, and it is very expensive and challenging to maintain the DS and FS concentration at a fixed value due to reverse solution flux. But in the case of a batch experiment, DS recycle is not required, but this approach requires a dynamic data collection system and dynamic model of the batch process. In this work, the batch experimental approach is used to characterize the flat sheet test cell/hollow fiber FO/PRO module by using an appropriate dynamic modeling approach.

The HF mathematical model of ultra-filtration (UF)/RO has been studied thoroughly with experimental validation by many researchers [32–34]. However, in the case of the FO/PRO process, the HF module modeling is not exhaustively studied with experimental model validation [9]. Developing a mathematical model for the HF is crucial to evaluate the commercially available FO/PRO module performance. It also plays a vital role in getting an optimal result from the FO/PRO processes through simulation and optimization studies. Moreover, the PRO study is important to estimate the blue potential energy that can be generated by mixing river water into seawater. Producing energy from an environment-friendly process, such as the PRO process, is essential for increasing the amount of energy generated from renewable sources.

1.4 Motivation

1.4.1 Importance of Incorporating the Water Evaporation and Concentration Variation Effects During Membrane Characterization

Characterization of commercial FO membranes provides fundamental insights into the membrane structures and properties, which helps to predict the performance of membranes during operation [35]. For instance, the membrane from hydration technology innovations has been extensively characterized and evaluated for FO desalination processes [36]. Some of the essential desired characteristics of FO membranes are

i) Dense ultra-thin active layers with high water and low solute permeability, and
ii) Highly porous support layers with minimum thickness and high mechanical strength [7].

Phenomena, such as fouling, reverse solute flux, and concentration polarization (CP) are expected to reduce the water flux. However, they can be minimized with the help of optimally designed FO membranes and suitable operating conditions. The optimal system design and analysis using an accurate membrane transport parameter are fundamental in developing an appropriate FO membrane for a given industrial application [37].

One of the challenges in the FO experiment is to maintain constant solution concentration during the flux measurement. Though the solute concentration in DS and FS tank is expected to vary during the FO experiment [17,31,38–41], most studies assumed the solution concentration to be either the initial concentration or average of initial and final concentrations while estimating the membrane transport parameters. This assumption is expected to introduce errors in the estimated parameters. The errors are expected to be more when the membrane water flux is high.

In addition, if the solution tanks are kept open to the environment, water evaporation from the FS and DS tanks is expected to occur. This is expected to affect both J_W and J_S, and ultimately affect the estimated parameters. The water evaporation may be minimized when the FO membrane test cell is fabricated using a closed circulatory system. Such a system requires an expensive control system to measure J_W and J_S. The cost of a closed-circuit FO flux measurement system by Sterlitech Corporation is around $ 60,000. Even after using a closed circulatory system, the variation in FS and DS concentration is unavoidable. The cost of the open circulatory system used in this study is purchased ~ $ 5000. Therefore, studying the experimental uncertainties due to the water evaporation and concentration variation is very important while designing large-scale FO/PRO processes, as it will reduce the error in the estimated membrane transport parameters.

1.4.2 Importance of Developing a Mathematical Model for Axial Flow Hollow Fiber Forward Osmosis Module

FO membrane modules are available in plate-and-frame, spiral-wound, tubular, and hollow fiber designs like that of RO modules membrane [42–45]. Modules with high specific surface area and recoveries such as HF [46–49] and spiral wound [50,51] are well accepted in the desalination and water treatment sector. However, the HF module is superior for FO experimentation due to its high packing density, low pumping and manufacturing cost, appropriate flow pattern, high permeate flow rate, and limited floor space requirement compared to the other membrane modules [52,53]. An optimized FO module should have

i) Minimum pressure drop in FS and DS channel,
ii) High surface area per unit volume,
iii) High and stable water flux,
iv) Low reverse solute flux,
v) Low manufacturing cost, and
vi) Controllable flow hydraulics [54].

In order to exploit the FO technology to its full extent, a precise model describing all the phenomena occurring during the FO process is required. The developed model should be capable of integrating the membrane transport, concentration polarization (CP), and pressure drop throughout the module. Unlike HF RO mathematical model, which has been studied thoroughly with experimental validation, the HF FO module performance is not exhaustively studied with experimental model validation [9,17,40,55].

With the rapidly growing attention towards the FO process, it has become inevitable to look for optimal designs and operational conditions. The optimization of the HF FO system reported by D. Xiao et al., focuses on optimizing the permeate recovery and FO efficiency by manipulating the module characteristics and operating conditions [56]. However, the effect of permeate flow rate and module dimension on the module pressure drop is omitted, which contributes to the operational costs of the system. In most FO-RO design studies, the energy spent on pumping of DS and FS and regeneration of DS is the root cause of FO inefficiency [57,58]. From the commercial point of view, the pumping cost of the FO solution has to be kept minimum by simple modifications in the FO module design and operating ranges. These modifications decide the permeate flow rate in a module and, therefore, the number of modules to be employed for a given production rate. But generally, the recovery from the FO process is fixed during the economic feasibility analysis. The number of modules employed affects the initial investment and operation and maintenance costs [21,57]. Thus, it becomes necessary to optimize the design and operating conditions of FO modules to provide maximum permeate at a minimum cost of production.

1.4.3 Importance of Developing a Mathematical Model for Axial Flow Hollow Fiber Pressure Retarded Osmosis Module

The PRO process is well known for converting the chemical potential between seawater and freshwater into hydraulic energy that can be further used to produce electrical energy. The first commercial PRO pilot plant was built and operated in

2009 by Statkraft in collaboration with the Norwegian University of Science and Technology [59]. The Statkraft has successfully operated the pilot plant by demonstrating the feasibility of power generation using the PRO process. However, the Statkraft could not further push its effort on the commercialization of the PRO technology for power generation applications as it was not an energy-efficient technology. One of the drawbacks related to this technology was the unavailability of an energy-efficient PRO membrane. However, in the 2000s, the PRO was revived owing to fast improvement in the PRO membrane and the use of a pressure exchanger. Yip and Elimelech [60] predicted that 1370 TWh/year of power might be generated by mixing 10% of the global river water discharge using the PRO process.

Various PRO studies have been conducted at the lab scale targeting process development, system modeling, and performance assessment [61–66]. These experiments have been carried out using various module arrangements such as plate and frame [52], spiral wound [67,68], and hollow fiber (HF) [69]. Similar to that of the FO process, the HF module was found to be the better module configuration for the PRO application owing to its high packing density [53,67].

The integration of the PRO process with other water purification processes, such as membrane distillation (MD), improved the energy efficiency of the whole system [70,71]. In addition, when a PRO system is combined with a modern RO desalination plant, approximately 3.87 MJ/m^3 of energy can be potentially generated at DS = 70.13 kg/m^3 and FS = 0.58 kg/m^3 [60]. Considering the PRO pilot plant establishment and availability of commercial PRO membranes, in 2018, H.W. Chung et al., [72] analyzed a technology gap that has to be addressed to operate a standalone PRO system for energy generation. The study estimated a minimum power density of 56.4 W/m^2 for the economic viability of the PRO system. Such high-power density may be achieved by improving the membrane performance and implementing PRO system-level optimization for PRO plant construction. System-level optimization can be achieved by introducing additional degrees of freedom for optimization such as membrane module length, configuration (parallel and series), and operating conditions.

In another aspect, several researchers have used the Ergun and Hagen-Poiseuille equation to estimate the pressure drop in the shell and lumen side of the HF module, respectively. Still, these models might not be accurate

i) When the flow surfaces are semipermeable [73,74], and

ii) When the diameter and the cylindrical structure of the HF are affected due to the presence of high pressure in the DS side.

The pressure drop in the HF PRO module accounts for the energy consumed in the module. Therefore, while solving energy optimization for the PRO process, the actual benefit would be a proper estimation of the pressure drop using a model that can predict near to realistic scenarios.

The economic feasibility of the PRO plant was also evaluated using seawater as DS and river water as FS for Iran costal [75] and Red Sea–Dead Sea water [76]. The result proved that the PRO process could be used to produce net electricity. When we come to India, the combination of a long coastline (about 7500 km) and abundant river water (9.76 x 1011 m3/year) flowing into the seawater across the southern peninsula of the Indian sub-continent provides the best and suitable conditions for blue energy extraction. However, a similar feasibility report for Indian blue energy capacity is not yet reported in the literature (until June 2019). Therefore, the estimation of this blue energy potential is very important to increase the percentile share of renewable energy.

1.5 Objective and Research Scope of the Thesis

The main objectives of this Ph.D. thesis are

1. To analyze the effect of water evaporation and concentration variation during membrane characterization with respect to steady-state and unsteady-state FO test cell model using a batch mode test cell experimental data

    a) Develop an unsteady-state mathematical expression for the FO membrane in a test cell.

b) Develop a mathematical expression for water evaporation.

c) Analyze the error due to the presence/absence of water evaporation and concentration variation.

2. To develop a mathematical model for axial flow hollow fiber FO/PRO module

a) Develop a mathematical model for HF FO/PRO module by integrating HF FO module equations with tank model equations.

b) Characterize the HF FO/PRO membrane using the hybrid unsteady-state model equations.

3. To simulate and optimize the hollow fiber FO/PRO module with respect to

a) Module properties such as module length, and

b) Operating conditions such as flow rate and pressure of both FS and DS.

4. To estimate the potential of Indian major rivers blue energy capacity by using an optimized PRO process condition.

1.6 Organization of the Thesis

The Doctoral thesis is organized into six chapters. A brief summary of the chapters is presented as follows.

Chapter 1 starts with the general backgrounds of FO and PRO processes and then presents the research motivation for the entire works. This chapter will also present the objectives and scope of the thesis. Finally, the organization of the thesis will be highlighted.

Chapter 2 presents the literature review.

Chapter 3 presents the fundamental concepts behind all equations used in unsteady-state FO test cell models. In this chapter, the water evaporation rate will be experimentally investigated and incorporated into the main design equations. Then, the total mass balance equation for the FS and DS tank in the presence and absence of water evaporation terms will be elaborated. Finally, the errors in membrane transport parameters due to experimental uncertainties such as water evaporation,

variation in solution volume and concentration, for low and high flux FO membranes will be evaluated.

Chapter 4 presents the solution diffusion (SD) model along with all the assumptions made to develop the mass and momentum balance equation for the axial flow HF FO module. In this chapter, the applicability of the Ergun equation and Hagen-Poiseuille equation for estimating the pressure drop on the shell and lumen side, respectively, will be experimentally investigated. The performance of the HF FO membrane will be evaluated with respect to the net permeate flow rate, total power consumption, and specific energy consumption. Then, an optimization problem will be formulated to maximize the net permeate flow rate and minimize power consumption. Finally, a two-step procedure will be developed for identifying the optimal solution from a given pilot-scale experiment.

Chapter 5 presents a mathematical model for an axial flow HF PRO module, which is capable of calculating the net hydraulic power generation by the PRO process. This chapter also states all the assumptions made to develop the mass and momentum balance equation for the axial flow HF PRO module. The applicability of the Ergun equation and Hagen-Poiseuille equation to estimate the pressure drop on the shell and lumen side, respectively, will be experimentally investigated for the PRO conditions. Then, the PRO model will be simulated to study the sensitivity of the PRO process operating condition and module length by calculating the net hydraulic power generation from the PRO process. Finally, the optimized PRO process will be used to estimate the Indian blue energy potential by mixing the Indian river and seawater before discharging into the sea.

Chapter 6 presents the main conclusions that can be drawn from the research work covered in this thesis. Also, it provides some suggestions towards the scope for future research.

Chapter 2 Review of Literature

Review of literature

This chapter presents the possible literature gaps on (i) Uncertainties in reported FO/PRO membrane characterization methods, (ii) Modeling and design optimization of the FO/PRO process by using lab-scale experimental data. Based on the identified literature gap, the detailed scope of this thesis is presented.

2.1 Membrane Characterization

Membrane characteristic parameters such as the membrane thickness, pore size, pore size distribution, pure water permeability, solute permeability, solute resistivity, mass transfer coefficient, etc. are either measured by using appropriate characterization equipment or estimated indirectly by performing osmotic experiments. These parameters are vital to the design and operation of the osmotic-driven membrane process with respect to the following aspects.

i) Selection of suitable membrane with respect to pore size and its distribution for a given separation process.

ii) During membrane process design, the membrane surface for a given design capacity can be calculated using pure water permeability, solute permeability, solute resistivity, and mass transfer coefficient.

iii) Modeling and simulation of the membrane separation process require the membrane transport parameters.

iv) The fouling intensity of the membrane process can be calculated by estimating pure water permeability in real-time using pressure and flow data, such that the membrane process can be monitored in real-time [9,39].

The optimal system design and analysis using an accurate membrane transport parameter are one of the fundamental aspects in developing an appropriate FO membrane for a given industrial application [40,73]. The membrane characterization technique can be divided based on its approaches, such as (i) destructive and non-destructive, (ii) invasive and non-invasive, (iii) static and dynamic, and (iv) online and offline.

The destructive technique helps to investigate the chemical and physical properties of the membrane by placing them in an appropriate measuring instrument, whereas the non-destructive technique helps to investigate the membrane performance without damaging the membrane [77]. In the case of a non-destructive technique, the characterized membrane can be used for further analysis without any damage to the membrane. But in the case of destructive technique, the membrane cannot be reused for further operation/analysis. For example, pore size analysis by Mercury porosimetry will be damaging the membrane surface, and it is called a destructive technique. Surface porosity analysis by Atomic force microscopy will not damage the membrane surface and is called a non-destructive technique.

Similarly, the technique that requires intervention, such as the dismantling of the membrane module and introduction of external components/chemicals through the membrane, is called as invasive techniques such as porometry. The technique that does not require the dismantling of the membrane module and introduction of external component/chemical through the membrane is called non-invasive techniques such as flux, retention measurements, and membrane fouling layer thickness measurement using ultrasonic sensor.

The membrane characterization performed by using dynamic data generated during the membrane performance analysis is known as a dynamic method. The method that uses static data is called a static technique. For example, membrane surface analysis by Scanning Electron Microscopy (SEM), Transmission Electron Microscopy (TEM) uses static data and, therefore, called as a static technique. Flux and retention measurements use both static and dynamic data due to membrane fouling; therefore, this technique is called as dynamic.

The techniques that can be applied in real-time while the membrane system is in operation is known as an online method. The method that requires stopping the regular membrane operation is known as the offline technique. For example, flux, retention, fouling layer thickness measurement by using a flow meter, pressure gauge, and ultrasonic sensor can be done in real-time without any intervention to

regular operation. In another aspect, an autopsy of the membrane system requires part of the membrane system to take them to offline mode to perform offline analysis.

Both online and offline techniques are widely used in the membrane industry for membrane system design and fouling monitoring applications [78–80]. Both methods are expected to provide flux pressure and solute retention data to calculate water permeability coefficient (A), solute permeability coefficient (B), structural parameter (S), and mass transfer coefficient correlation. Also, all other techniques, for example, SEM, porometer, tensiometers, etc., are not viable to use during online membrane system operation [49]. The membrane transport parameter such as A, B, and S should be estimated by conducting osmotic experiments in the laboratory. While estimating these parameters, errors in the estimated parameters might arise due to the influence of the experimental uncertainty, such as variation in solution concentration and water evaporation. Thus, to minimize the errors in the estimated parameters, researchers have proposed different techniques. Some of them are discussed below.

2.1.1 Effect of Concentration Variation on Membrane Characterization

One of the challenges in the FO membrane characterization experiment is the accommodation of variation in a draw and feed solution concentration while estimating the membrane transport parameter using a batch FO experimental data [17,31,38–41]. One of the approaches reported in the literature is that the solution concentration is assumed to be either equal to the initial concentration or average of initial and final concentrations while estimating the membrane transport parameters. This assumption is expected to introduce errors in the estimated parameters. The errors in the estimated parameters are also expected to be more when the water flux is high. Thus, to minimize the concentration variation during the FO experiment, various researchers have proposed different approaches. Some of them are listed below:

Cath et al., [3] have proposed three different approaches while measuring the water flux and solute flux. In the first approach, a control system was recommended to

maintain the concentration of both DS and FS by adding concentrated salt solution in the DS tank and pure water in the FS tank. In the second approach, a large DS volume and a control FS volume were recommended. However, in both approaches, minor variations in FS and DS concentration were observed due to a solute loss in the DS tank and accumulation in the FS tank. In the last approach, solute mass balance for FS and overall mass balance for DS tanks were recommended to calculate J_S and J_W, respectively.

In another study, A. Tiraferri et al. [31] have used large volumes of DS and FS tanks to maintain nearly equal osmotic pressure during the entire period of the experiment. This approach helped them to precisely monitor both the concentration and volume of DS and FS tanks. As a result, they were able to obtain less than 0.5 % DS concentration variation between the start and end of the experiment.

Further, to accommodate the concentration variations in the FS and DS tanks with respect to time, Ruprakobkit et al., 2016 [81] have proposed an unsteady state model-based FO membrane characterization technique. They have developed the unsteady-state model to concentrate carboxylic acid using plate and frame configuration. The developed model was able to calculate the DS and FS concentration of the FO system at any given simulating time. The developed model was also capable of suggesting the optimal initial DS concentration conditions for the best FO performance. Hence, a similar unsteady-state model is required for FO membrane characterization using membrane test cell.

2.1.2 Effect of Water Evaporation on Membrane Characterization

Water evaporation is a phenomenon that occurs above the DS and FS solution surface due to the humidification of air above the solution surface, such as liquid food concentration and desalination [82]. There are a lot of factors that can affect the water evaporation from saline water. The main factors could be seawater salinity, humidity, air velocity, evaporation surface area, solution, and surrounding temperature. The water evaporation rate can be measured with various methods, such as a change in weight or level of the water tank, change in humidity of the air

stream, and change in moisture in moisture adsorbent materials [82]. The weight-based measurement is found to be more accurate. However, till date, there is a limitation in having a good water evaporation predictive model, which might include all the possible factors. In this section, some of the literature which focuses on the water evaporation predictive model from saline water will be reviewed.

In 2002, Al-Shammiri, [82] had reviewed the previously used instruments, methods, and experimental conditions and came up with a new predictive model for water evaporation from the saline solution. The new predictive model was formulated by considering the effect of salinity on the water evaporation rate, which was not covered by any other researcher before. Upon comparing the newly developed predictive model with the previous method, the comparison result revealed that there was a reduction in the water evaporation rate when the salinity of the water is increased. This was due to the vapor pressure reduction at the water surface when the water salinity is increased. In another aspect, the water evaporation from a saline water body is less than that of a freshwater body due to lower saturation vapor pressure present in the saline water body [83]. The average accuracy of the newly developed method for predicting water evaporation was $R^2 = 0.91$.

Again in 2007, Salman and Al-Shammiri [84] have developed an improved water evaporation predictive model using computational intelligence. The method was based on three experimental methods and various air velocities, brine concentrations, and air and water temperatures. As this approach used various sets of experimental data under different conditions, the average accuracy of this model increased to $R^2 = 0.975$.

Even though there are plenty of literature and models regarding the water evaporation rate from saline water, however, there is no a single literature that incorporates the water evaporation effect in the osmotically driven processes. All the available literature in the FO and PRO processes have not included the effect of water evaporation. The reason for this could be either (i) due to the assumption that the water evaporation rate is negligible, or (ii) they might not notice the effect of water evaporation at all. However, if the solution tanks of both FS and DS are kept open to

the environment, water evaporation from the FS and DS tanks is expected to occur, and this might increase the error during the parameter estimation. The water evaporation may be minimized when the FO membrane test cell is fabricated using a closed circulatory system. Such a system requires an expensive control system to measure J_W and J_S. The cost of a closed-circuit FO flux measurement system by Sterlitech Corporation is around $ 60,000. Therefore, the effect of both concentration variation and water evaporation on the estimation of FO membrane parameters in an open circulatory system needs to be addressed.

Possible Scope for Further Research

The FO membrane characterization literature is limited with respect to incorporating the water evaporation effect during a batch FO experiment. Hence, this study proposes a method that aims at including the water evaporation rate while calculating the solvent and solute fluxes, which will ultimately reduce the error in the estimated membrane transport parameters. Unsteady-state FS and DS tank model, which incorporates both the concentration variation and water evaporation effect, will be introduced for estimating the membrane transport parameters more accurately and by using a low-cost FO test experimental setup. In addition, the errors between the estimated membrane transport parameters of unsteady and steady-state models will be analyzed with respect to membrane flux, solution concentration, solution volume, and presence and absence of water evaporation model. Finally, the optimum experimental condition for achieving minimum error in the estimation of the model parameter will be proposed.

Table 2-1. Literature summary on FO membrane characterization

Author	Year	Summary	Literature Gap
M. Al-Shammiri et al. [82]	2002	Studied water evaporation rate as a function of water salinity	Not studied with respect to PRO/FO application
A. Salman, M. Al-Shammiri [84]	2007	Developed a new computational intelligence model for predicting evaporation rates for saline water	Not studied with respect to PRO/FO application
R. Wang et al. [49]	2010	Characterized novel hollow fiber forward osmosis membranes	Required expensive equipment and not applicable for unsteady-state approach
T. Ruprakobkit et al. [81]	2016	Developed a dynamic simulation model for concentrating carboxylic acid using the FO process	Not included the water evaporation loss

2.2 Experimentation, Modeling, and Optimization Studies on Axial Flow Hollow Fiber Forward Osmosis Module

2.2.1 FO Membrane Module Configuration

One of the most important factors which affect the performance of the FO process is the selection of an appropriate FO module. Hence, one has to choose the module type as per the requirement of the selected application, such as operating pressure, fouling intensity of the feed and draw solution, and economics of the overall process. The FO membrane modules are available in plate-and-frame, spiral-wound, tubular, and hollow fiber designs like that of RO membrane modules, as depicted in Figure

2-1 [42–45]. However, modules with high specific surface area and recoveries such as HF [46–49] and spiral wound [50,51] are well accepted for the FO process. In this study, the HF module is chosen for FO experimentation due to its high packing density, low pumping and manufacturing cost, appropriate flow pattern, high permeate flow, and limited floor space compared to the other membrane modules, as shown in Table 2-2 [52,53].

Table 2-2. Membrane module comparison

Module	Plate and frame	Tubular	Hollow fiber	Spiral wound	Reference
Packing Density (m^2/m^3)	100	500	1600	600	[85]
Energy cost (pumping)	Moderate	High	Low	Low	[86]
Ease of cleaning	Good	Excellent	Fair	Moderate	
Manufacturing cost ($/m^2)	50-200	50-200	5-20	5-100	[87]
Suitable for high-pressure operation	Yes	Marginal	Yes	Yes	

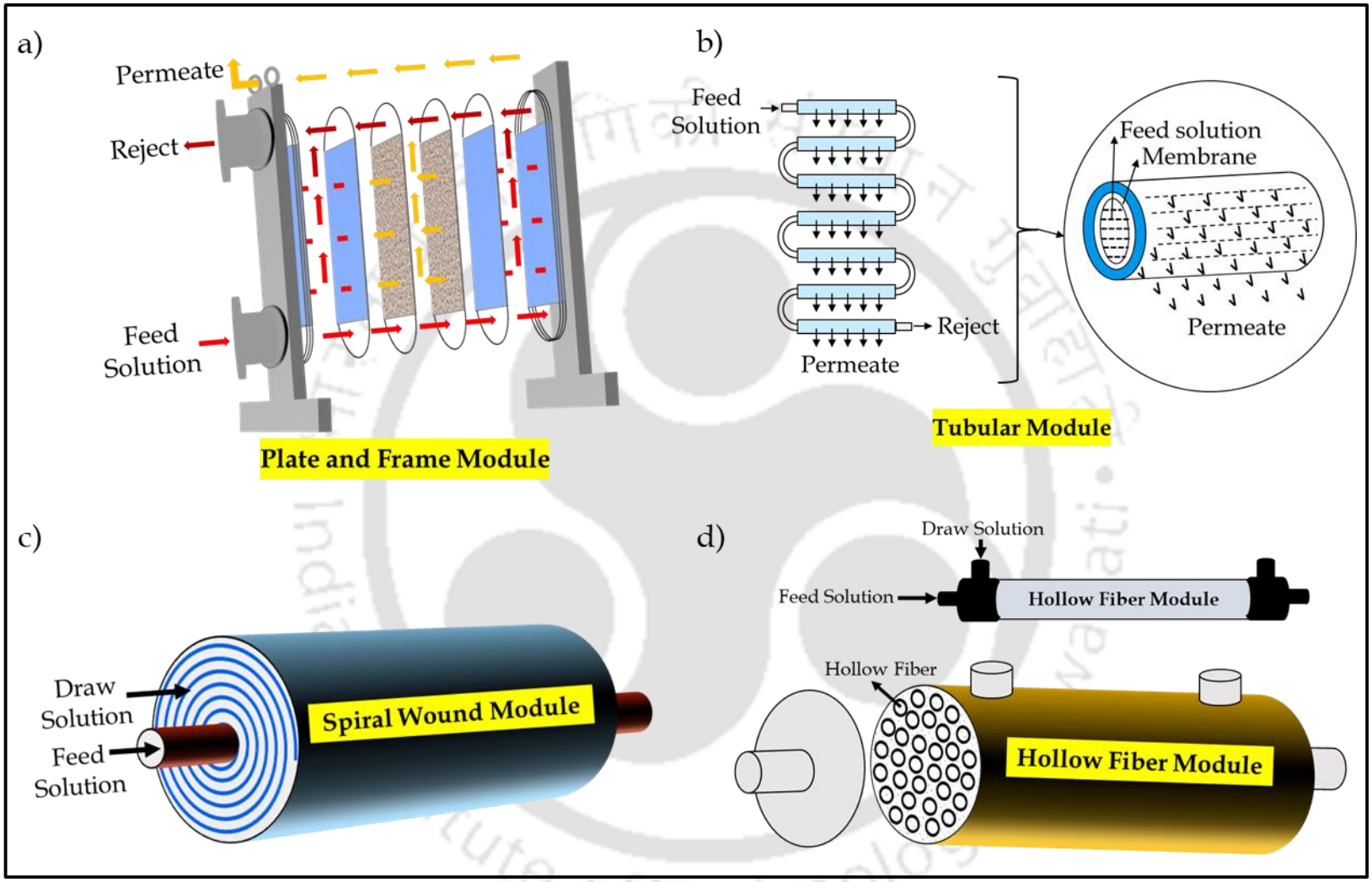

Figure 2-1. Types of FO membrane modules

2.2.2 Mathematical Models for HF FO Module

Developing a precise mathematical model is not only a base for predicting the performance of the FO process but also helps to optimize the overall FO process. Hence, to exploit the FO process to its full extent, it is crucial to develop a precise model that is capable of describing all the phenomena that occur during the FO process. With this regard, various researchers [32–34,88] have tried to develop HF RO mathematical model, which is capable of integrating the membrane transport, concentration polarization (CP), and pressure drop throughout the module. Unlike the HF RO mathematical model, which has been studied thoroughly with experimental validation, the HF FO module performance is not exhaustively studied with experimental model validation. In this section, we will try to review literature that focuses on the HF FO mathematical model development and then find the literature gaps.

In 2015, Shibuya et al., [89] had experimentally investigated the effect of operating conditions such as DS concentration, FS and DS flow rates, operating temperature, and membrane orientation on the performance of the HF FO process using a small-scale module. The small-scale HF FO module had the following specification: 700 HF with an outer diameter of less than 200 µm, module length of 0.3 m, and an effective membrane area of 0.12 m^2. They have analyzed the experimental data by using theoretical calculations and obtained satisfactory results.

Again in 2016, Shibuya et al., [53] had experimentally and theoretically investigated the effect of operating conditions on the performance of the HF FO process using a large-scale module with a cross-wound configuration. The large-scale HF FO module had the following specification: 220,000 HF, outer diameter of 175 µm, inner diameter of 75 µm, module length of 0.682 m, packing density of 54.2 %, and a cross-wound configuration. A friction-concentration polarization (FCP) model, which incorporates both the pressure drop and external concentration polarization (ECP) were used for the simulation study.

However, the model proposed by Shibuya et al., was based on the radial flow HF FO module. Hence, it cannot be used for the simulation of the axial flow HF FO module. Also, their studies did not include the parameter estimation from the FO experiments. Moreover, both studies excluded the effect of ECP on the FS side for the active layer facing DS (ALDS) orientation. The ECP on the FS side was neglected in most studies due to low recovery from the process. But, the high recovery in the FO process might lead to high concentration polarization on the FS side, and in this thesis, one of the objectives is to operate the FO process at high recovery. Hence, it is important to incorporate the ECP effect on the FS side of the HF module. Neglecting the ECP effect on the FS side might lead to errors in the solute permeability and mass transfer coefficient estimation. Integrating both ECPs in the membrane transport model equations provides better accuracy in the estimated parameters.

2.2.3 Optimization of HF FO Process

With the rapidly growing attention towards the FO process, it has become inevitable to look for optimal designs and operational conditions. The optimization of the HF FO system reported by D. Xiao et al., [56] focuses on optimizing the permeate recovery and FO efficiency by manipulating the module characteristics and operating conditions. However, the effect of permeate flow rate and module dimension on the module pressure-drop is omitted, which contributes to the operational costs of the system.

In most FO-RO design studies, the energy spent on pumping of DS and FS and regeneration of DS is the root cause of FO inefficiency [57,58]. From the commercial point of view, the pumping cost of the FO solution has to be kept minimum by manipulating the FO module design and operating ranges. These modifications decide the permeate flow rate in a module and, thus, the number of modules to be employed for a given production rate. But generally, the recovery from the FO process is fixed during the economic feasibility analysis. The number of modules employed affects the initial investment and operation and maintenance costs [21,57]. Thus, it becomes necessary to optimize the design and operating conditions of FO modules in order to provide maximum permeate at a minimum operating cost.

However, in most HF FO studies, the optimization of the FO process is missing. For example, Shibuya et al., [53] have only investigated the effect of operating function on the HF FO performance. Their study was limited to the impact of module length on the HF FO performance, and optimization studies are missing.

Possible Scope for Further Research

To the best of our knowledge, no study has been carried out using a mathematical model of axial flow HF module along with a tank model equation to estimate the performance of the batch mode FO processes. Hence, in this thesis, the axial flow HF FO modeling, simulation, and optimization are thoroughly covered. A Toyobo HF membrane module with an axial flow arrangement will be used for conducting the FO experiments. In this thesis, the model parameter estimation procedure is designed by using dynamic FO process data and unsteady state FO process. Since this approach gives the advantage of using experimental results at various inlet conditions due to the continuous concentration of FS and dilution of DS, the accuracy of the parameters is expected to be superior. In line with this, an optimization problem will be set up to find the optimum length of the module, flow rate, and pressure of DS and FS for maximizing the net permeate flow per unit energy input for a given membrane area.

2.3 Experimentation, Modeling, and Optimization Studies on Axial Flow Hollow Fiber Pressure Retarded Osmosis Module

2.3.1 Selection of PRO Module

Various PRO studies have been conducted at the lab scale targeting process development, system modeling, simulation, and performance assessment [61–66]. These experiments have been carried out using various module arrangements such as plate and frame [52], spiral wound [67,68], and hollow fiber (HF) [69]. However, the HF module was found to be the better module configuration owing to its high packing density [53,67]. In this study, we have used the HF FO module for analyzing the performance of the PRO process.

2.3.2 Techno-economic Analysis for Hybrid and Stand-alone PRO Process

As recommended by the Statkraft [59], many researchers have studied the techno-economic analysis of the hybrid seawater reverse osmosis (SWRO) + PRO process through a simulation study [72,90,91]. Senthil and Senthilmurugan [90] have proposed six different hybrid SWRO + PRO configurations that can produce both energy and water together by mixing SWRO brine and wastewater. The pros and cons of all the six configurations were analyzed by simulating the corresponding flowsheet configurations. The SWRO + PRO configuration with a straight mixing of diluted PRO DS outlet and pre-treated seawater of SWRO brought down the energy consumption to 49% in contrast with the standard SWRO desalination system. Later, Wan and Chung [92] studied the techno-economic assessment of several hybrid RO - PRO and RO - FO combined processes for water and energy nexus applications. They concluded that the SWRO + PRO unit with direct mixing of draw and seawater offers more significant advantages than SWRO + PRO configuration without mixing draw and seawater to SWRO feed and FO + SWRO configuration. Recently in 2018, Park et al., [91] have proven the economic viability of the SWRO + PRO plant by construction and operation of 240 m^3/d PRO treatment capacity. Similarly, many authors [92–95] have reported the feasibility of combining PRO with SWRO with improved PRO membranes.

Considering the PRO pilot plant establishment and availability of commercial PRO membranes, in 2018, Chung et al., [72] analyzed a technology gap that has to be addressed to operate a standalone PRO system for energy generation. The study estimated a minimum power density of 56.4 W/m^2 for the economic viability of the PRO system. Such high-power density may be achieved by improving the membrane performance and implementing PRO system-level optimization for PRO plant construction. System-level optimization can be achieved by introducing additional degrees of freedom for optimization such as membrane module length, configuration (parallel and series), and operating conditions.

The economic feasibility study based on a simplified model of PRO plant for Iran costal [75] and Red Sea – Dead Seawater [76] concludes that the PRO process can be

used to produce net electricity by mixing river and seawater. The reduction in the pre-treated water cost and integration of SWRO brine may lead to a better return on investment. A similar feasibility report for Indian blue energy capacity is not yet reported in the literature (until June 2019).

2.3.3 Modeling and Optimization of HF PRO Process

Model development, simulation, and optimization studies are crucial for improving the performance of both lab and pilot-scale PRO processes [61–66]. In 2017, Higa et al., [69] had evaluated the steady-state HF PRO performance and investigated the effect of operating conditions using a pilot-scale module. However, their model was not applicable to the unsteady state system, and the optimization studies were missing.

Recently Y. Tanaka et al., [52] had proposed a mathematical model for the HF PRO module, which includes parameter estimation from experimental water flux data. Also, they have experimentally and theoretically analyzed the performance of two pilot-scale HF FO modules with the cross-wound configuration for the PRO process and investigated the effect of operating conditions. However, the developed model was not applicable for no wound configuration. In addition, the effect of ECP was not included on the FS side of the membrane. Further, the solute flux prediction of the model with respect to the experimental results and the optimization studies with respect to the operating condition was missing in their study.

Further, Kishimoto et al., [96] had investigated the optimization of the HF PRO process using a numerical simulation. They have maximized the power generation by optimizing the operating condition using river water as FS and seawater as DS. However, in their study, they have not included the effect of module length and the ECP effect on the FS side. As their model was developed for radial flow HF with cross-wound configuration, it is not applicable for axial flow HF without cross-wound configuration. Also, they have not considered the inefficiency of the pumps, turbines, and pressure exchangers, which hugely affect the overall power generation. Further, they have considered the Ergun equation and Hagen-Poiseuille equation for

estimating pressure drop in the shell and lumen side, respectively. These models may not be accurate when the flow surfaces are semipermeable and when the diameter and the cylindrical structure of the HF are affected due to the presence of high pressure in the DS (shell) side [73,74].

As the range of power density reported for commercial HF modules at seawater concentration was 0.57-1.77 W/m^2 [65], R. Long et al., established a multi-objective optimization strategy to maximize both energy efficiency and power density together [97]. They validated the PRO model using the PRO test cell. The main difference between the test cell and commercial module experimental data is that there is a high-pressure drop in the commercial module in comparison to the test cell. The studies on HF PRO modeling consider the Ergun equation and Hagen-Poiseuille equation for estimating pressure drop in the shell and lumen side, respectively. However, these models may not be accurate when the flow surfaces are semipermeable [73,74]. The pressure drop in the HF PRO module accounts for the energy consumed in the module.

The reported literature in the area of PRO optimization was focused on formulating the following objectives to improve PRO process performance (i) maximization of power density [96,98], (ii) maximization of net specific energy generation [99–102], (iii) overall profit of the PRO process [93], (iv) maximization of both power density and PRO efficiency [97]. But, in the process of energy extraction from the PRO process, the availability of river water is one of the critical parameters, and therefore, the maximization of net power generation by PRO process per unit river water supply may provide the maximum benefit. Also, while solving energy optimization for the PRO process, the actual benefit can be estimated by using a model that can predict near to realistic scenarios.

Possible Scope for Further Research

Considering the above literature gap, in this work, the optimization strategy is proposed for the PRO plant to maximize the energy production for a given flow capacity of river water by manipulating both operating conditions and PRO plant configuration. The mathematical model presented in this study integrates both the

mass and momentum balance equations along with the membrane transport equation. The membrane transport equation is coupled with both internal and external concentration polarization (ICP and ECP) equations to incorporate the impact of both flow hydrodynamics and module recovery. The developed model will be validated by using experimental data generated from the commercial hollow fiber PRO membrane module. Finally, the blue energy potential for Indian major rivers will be calculated by using optimized PRO plant operating conditions established in this work.

2.4 Summary of Literature on Modeling, Simulation, and Optimization Studies of FO and PRO Processes

Several studies are available regarding FO/PRO membrane module modeling, simulation, and optimization. The most relevant literature, which mainly focuses on modeling, simulation, and optimization of FO/PRO are reviewed and summarized based on the type of module used, parameters consider, type of membrane transport used, membrane orientation, concentration polarization, optimized parameter, etc. as shown in Table 2-3.

Table 2-3. Summary of literature for Modeling, Simulation and Optimization of PRO

Ref.	Type of Module	Initial condition (kg/m^3)	Parameter Considered	Lumped/ Distributed	Membrane Transport Model	Membrane orientation	Concentration Polarization	Optimized parameter	Model Validation	Solution Density	Process
Holt et al., (2012) [103]	HF	C_{DS} = 32 C_F = 0	Concentration	Lumped	SD	ALDS	CICP	A, B, S	Yes	Constant	PRO
He et al., (2014) [104]	Test cell	C_{DS} = 35 C_{FS} = 0.1	Concentration	Lumped	SD	ALFS	DICP, CECP	A, B, S	Yes	Depend on conc.	PRO
Attarde et al., (2015) [5]	Spiral	C_{DS} = 4-60 C_{FS} = 0-1	Concentration velocity pressure	Distributed	SD	ALDS	CICP, DECP	A, B, K, ka, kb	Yes	Constant	PRO/FO
Attarde et al., (2016) [24]	Spiral	C_{DS} = 10-60 C_{FS} = 0.5	Concentration velocity pressure	Distributed	SK	ALDS	CICP, DECP	Lp, B, σ, K, k_a, k_b	Yes	Constant	PRO/FO
Pardeshi et al., (2016) [105]	Test cell	C_{DS} = 116 C_{FS} = 0	Temperature Velocity	Distributed	ANN	Both	Not considered	u_{FS}, u_{DS}, T_{FS}, T_{DS}	Yes	constant	FO
Ruprakobkit et al., (2016) [81]	Plate and frame	C_{DS} = 53.5 C_{FS} = 0.6	Concentration	Lumped	SD	ALFS	DICP, CECP	A, B, S, B_a	Yes	Constant	FO
S.S.S.S (2016) [90]	Spiral	C_{DS} = 32 C_{FS} = 0.1-10	Concentration velocity pressure	Lumped	SK	ALDS	CICP, DECP	A, B, σ, x, y, D_f	Yes	Constant	RO–PRO
Wang et al., (2016) [106]	Test cell	C_{DS} = 60 C_{FS} = 0.1	Concentration velocity pressure	Distributed	SD	ALDS	CICP, DECP, RSD	A, B, K	Yes	Depend on conc.	PRO
Sagiv et al., (2017) [107]	Test cell	C_{DS}= 35-339 C_{FS}= 0.58-58	Concentration velocity pressure	Distributed	SD	ALFS	Not Considered	A, B, $V_{F,in}$, V_d, L, H	Yes	Constant	PRO

2.5 Literature Closure

In summary, the main features of the literature can be summarized as follows:

- FO membrane characterization that includes the effect of water evaporation and concentration variation is not yet addressed.
- A mathematical model for the axial HF FO module that incorporates the dynamic variation of FS and DS during lab-scale experiments is not yet studied.
- An optimization problem is not yet set up for the axial flow HF FO process to find out the optimum
    - ❖ Module length,
    - ❖ DS and FS flow rate, and
    - ❖ DS and FS pressure.
- Experimentation, simulation, and optimization study on the axial flow HF PRO module with respect to module properties and operating conditions is not also addressed.
- Even though the combination of a long coastline and abundant river water flowing into the seawater across the southern peninsula of the Indian sub-continent provides the best and suitable conditions for blue energy extraction, however, this huge energy potential is not yet estimated.

Chapter 3 Uncertainty Analysis in Forward Osmosis Membrane Characterization Using Test Cell

Parts of this Chapter is revision-submitted for publication as research articles:

- **H. T. Aseffa** and S. Subbiah, Error analysis during forward osmosis membrane characterization in open recirculatory system

Uncertainty Analysis in Forward Osmosis Membrane Characterization Using Test Cell

The work presented in this chapter is focused on the development of an unsteady-state FO model that incorporates the water evaporation rates from the surface of both FS and DS tanks. The aim is to evaluate the errors in membrane characterization experiments due to the experimental uncertainties such as water evaporation, variation in solution volume and concentration, for low and high flux FO membranes. For the low flux FO membrane, various experiments are performed in this work, and for the high flux FO membrane, the experimental data are simulated using the parameters adopted from Zhang et al. The water evaporation from the solution tank is experimentally investigated and incorporated into the FS and DS tank mass balance equations. The errors in the membrane transport parameters due to the experimental uncertainties in the presence and absence of water evaporation term are compared. In addition, the error on the estimated parameters due to FS and DS concentration variation during the FO test cell batch experiment is presented. Finally, based on the experimental investigation and simulation analysis, a model that leads to a minimal error in the estimated parameters is proposed.

3.1 Theory

3.1.1 Modeling of FO Membrane Test Cell Setup

The unsteady-state model for FO membrane test cell is developed by integrating systems of model equations, namely (i) the macroscopic unsteady state water and solute balance equations for FS and DS tanks, (ii) Spiegler–Kedem (SK) model for membrane active layer transport, and (iii) film theory model for mass transport in ICP and ECP layers. More details about the SK and CP model equations are provided by Attarde et al.[5,24]. For this study, the FO analysis and equation derivations are based on ALDS orientation.

3.1.1.1 Membrane Transport Models

The transport of solvent and solute through membranes is most widely expressed by using either the solution-diffusion (SD) or SK models. The SD model assumes that both solvent and solute are adsorbed on the membrane surface and then diffuse from high to low chemical potential side through the dense membrane. Finally, the diffused solvent and solute will be desorbed on the low concentration side. The adsorption and diffusion capacities of the solvent and solute through the membrane are defined in terms of solvent permeability (A) and solute permeability (B).

The SK model is derived based on the irreversible thermodynamic principle. Here, both J_W and J_S will be calculated by mapping fluxes with their corresponding forces such as pressure, osmotic pressure difference, and the interaction effect between them. The final flux equations of the SK model consist of a reflection coefficient in addition to the other two parameters of the SD model. The flux equations of the SK model are expressed as follows [5,24],

$$J_W = L_p\left[\frac{vRT}{M_W}\sigma\left(C_{DS,m} - C_{FS,m}\right) - \left(P_{DS} - P_{FS}\right)\right] \tag{3.1}$$

$$J_S = -\frac{J_W\left(1-\sigma\right)\left[C_{DS,m} - C_{FS,m}\exp\left(\frac{J_W(1-\sigma)}{B}\right)\right]}{\exp\left(\frac{J_W(1-\sigma)}{B}\right) - 1} \tag{3.2}$$

where J_W, J_S, Lp, B, and σ are water flux in [$m^3/(m^2\ s)$], solute flux in [$kg/(m^2\ s)$], water permeability in [$m^3/(m^2\ s\ Pa)$], solute permeability in [m/s] and reflection coefficient in [-], respectively. $C_{FS,m}$ and $C_{DS,m}$ are the FS and DS concentrations at the active layer of membrane surface in [kg/m^3], respectively, P_{FS} and P_{DS} are applied hydraulic pressures of FS and DS in [Pa], respectively. v, M_w, T, and R are the Van't Hoff factor in [-], molecular weight in [kg/kmol], the temperature of the solution in [K], and the universal gas constant in [Pa $m^3/(mol\ K)$], respectively.

3.1.1.2 Concentration Polarization (CP) Model

CP is one of the performance-limiting factors in the FO process [17,40,55,108]. CP is developed owing to the accumulation or dilution of solute near the membrane surface. It cannot be eliminated, but it can be minimized [49]. As shown in Figure 3-1, two types of CP are observed: (i) ICP/ECP, and (ii) dilute/concentrated CP. ICP quantifies the CP in the membrane support layer and ECP quantifies the CP near to the membrane surface [55,109]. The influence of ECP on the water flux can be minimized by proper controlling of the hydrodynamic conditions at the membrane surface. As shown in Figure 3-1, the dilute CP occurs in the DS side, and the concentrated CP occurs in the FS side of the membrane when the membrane active layer is in contact with DS. The concentration of DS at the membrane surface ($C_{DS,m}$) is lower than that of the bulk ($C_{DS,b}$) due to J_W from FS to DS. Therefore, the effective osmotic pressure will be low in the presence of a highly dilute CP.

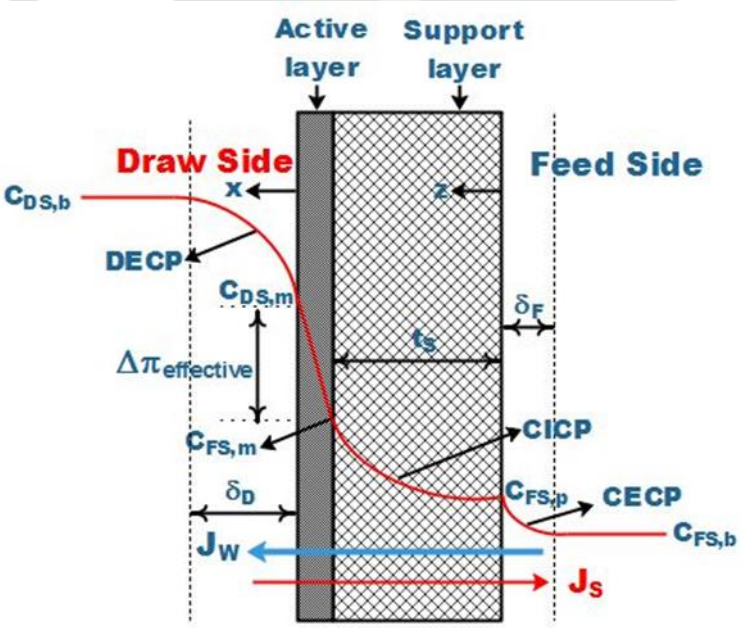

Figure 3-1. Illustration of concentration profile across the asymmetric FO membrane for ALDS orientation

The dilutive external concentration polarization (DECP) model equation is defined according to the film theory, i.e., solute balance across a boundary layer near the membrane active layer includes diffusive and convective components [62]:

$$J_S = D_s \frac{dC(x)}{dx} - J_W C(x) \tag{3.3}$$

As Eq. 3.2 equals Eq. 3.3 for steady state case, the integration of the resulting equation across the following ECP boundary layer

C(x) = $C_{DS,m}$ at x = 0,

C(x) = $C_{DS,b}$ at x = δ, yields

$$C_{DS,m} = C_{DS,b} \exp\left(\frac{-J_W}{k_{DS}}\right) + \frac{(1-\sigma)\left[C_{DS,m} - C_{FS,m}\exp(\frac{J_W(1-\sigma)}{B})\right]}{\exp(\frac{J_W(1-\sigma)}{B})}\left[\exp\left(-\frac{J_W}{k_{DS}}\right)-1\right] \tag{3.4}$$

where k_{DS} is the mass transfer coefficient on the DS side.

In the literature [5,17,24,55,62], the FS is assumed to be very diluted; thus, the support layer is expected to have zero salt rejection. Therefore, the effect of concentrative external concentration polarization (CECP) is always neglected. However, recent FO applications use pre-treated domestic wastewater as FS. Therefore, the CECP model equation (Eq. 3.5) and included in this study:

$$C_{FS,p} = C_{FS,b} \exp\left(\frac{J_W}{k_{FS}}\right) + \frac{(1-\sigma)\left[C_{DS,m} - C_{FS,m}\exp(\frac{J_W(1-\sigma)}{B})\right]}{\exp(\frac{J_W(1-\sigma)}{B})}\left[\exp\left(\frac{J_W}{k_{FS}}\right)-1\right] \tag{3.5}$$

Where $C_{FS,p}$ and $C_{FS,b}$ are the concentration of FS at the surface of the porous support and feed bulk phase, and k_{FS} is the mass transfer coefficient in the FS side.

The following relation may be obtained for the concentrative internal concentration polarization (CICP) in the support layer by integrating the SK and CP models [24].

$$\frac{C_{FS,m}}{C_{DS,m}} = \frac{\left[1-\exp\left(\frac{J_W(1-\sigma)}{B}\right)\right]\exp(J_W K)\frac{C_{FS,p}}{C_{DS,m}} + (1-\sigma)\left[1-\exp(J_W K)\right]}{\left[1-\exp\left(\frac{J_W(1-\sigma)}{B}\right)\right] + (1-\sigma)\exp\left(\frac{J_W(1-\sigma)}{B}\right)\left[1-\exp(J_W K)\right]} \tag{3.6}$$

The solute resistivity (K) is defined as the ratio of the structural parameter (S) and the diffusion coefficient (D_S) of the solute at the support layer. S is also called boundary layer thickness.

$$K = \frac{S}{D_{diff}} = \frac{t_S \tau}{\varepsilon D_{diff}} \tag{3.7}$$

Where, K, S, D_{diff}, t_S, τ, and ε are the solute resistivity in [s/m], structural parameter [m], diffusion coefficient of the solute at porous support layer in [m^2/s], thickness in [m], tortuosity in [-] and porosity in [-] of the support layer respectively.

Further, the following correlations can be used for estimating the FO test cell mass transfer coefficient under laminar flow conditions [110].

$$Sh = a\,\mathrm{Re}^{k_b}\,Sc^{1/3} \tag{3.8}$$

Where,

$$\mathrm{Re} = \frac{\rho u d_h}{\mu} \tag{3.9}$$

$$Sc = \frac{\mu}{\rho D_{diff}} \tag{3.10}$$

$$k = \frac{D_{diff} Sh}{d_h} \tag{3.11}$$

Where ρ, u, d_h, μ, and D_{diff} are density, velocity, hydraulic diameter, viscosity, and diffusion coefficient, respectively. The parameter a and k_b has to be estimated using experimental data.

The hydraulic diameter might be estimated using Eq. 3.12 for spacer occupied channel [111]

$$d_h = \frac{4(\text{volume of flow channel})}{\text{wetted surface}} \tag{3.12}$$

The mass transfer coefficient can also be expressed as a power function of FS/DS velocity after simplifying Eq. 3.8, [33,112]:

$$k = k_a u^{k_b} \tag{3.13}$$

where k_a, and k_b are mass transfer coefficient correlation constants [$k_a = a\left(\frac{\rho h_d}{\mu}\right)^{k_b} (Sc)^{1/3}$ and $k_b = 0.5$].

3.1.1.3 Unsteady State Solute and Solvent Balance for Solution Tank in the Presence and Absence of Water Evaporation

As shown in Figure 3-2, the mass and concentration of FS and DS variation during the FO experiment, with and without water evaporation, can be addressed using the following equations:

The DS and FS tank total mass balance equations in the absence of water evaporation are given by:

$$\frac{dM_{DS}}{dt} = J_W A_M \rho_w - J_S A_M \tag{3.14}$$

$$\frac{dM_{FS}}{dt} = -J_W A_M \rho_w + J_S A_M \tag{3.15}$$

The DS and FS tank total mass balance equations in the presence of water evaporation are given by:

$$\frac{dM_{DS}}{dt} = J_W A_M \rho_w - J_S A_M - E_{DS} A_{DS-Air} \tag{3.16}$$

$$\frac{dM_{FS}}{dt} = -J_W A_M \rho_W + J_S A_M - E_{FS} A_{FS-Air} \tag{3.17}$$

The solute mass balances in the DS and FS tank are given by:

$$\frac{dC_{DS}V_{DS}}{dt} = -J_S A_M \tag{3.18}$$

$$\frac{dC_{FS}V_{FS}}{dt} = J_S A_M \tag{3.19}$$

The DS and FS tank volumes and densities are given by:

$$V_{DS} = \frac{M_{DS}}{\rho_{DS}} \tag{3.20}$$

$$V_{FS} = \frac{M_{FS}}{\rho_{FS}} \tag{3.21}$$

$$\rho_{DS} = \rho_W + C_{DS} \tag{3.22}$$

$$\rho_{FS} = \rho_W + C_{FS} \tag{3.23}$$

where V_{DS}, V_{FS}, M_{DS}, M_{FS}, C_{DS}, C_{FS}, ρ_{DS} , and ρ_{FS} are respectively the volumes in [m^3], masses in [kg], concentrations in [kg/m^3], and densities of DS and FS in [kg/m^3]; ρ_W is the density of water in [kg/m^3], A_M is the membrane surface area in [m^2], E_{DS} and E_{FS} are the water evaporation rates from the DS and FS tanks respectively in [$kg/(m^2\ s)$], $A_{FS\text{-}Air}$ and $A_{DS\text{-}Air}$ are the surface area of FS and DS which is in contact with the Air respectively in [m^2], respectively.

In this study, E_{FS} and E_{DS} are calculated using Eq. 3.24 and 3.25, which were experimentally measured for FS and DS:

$$E_{FS} = \frac{1.97}{1.2x10^6 A_{FS-Air}} \tag{3.24}$$

$$E_{DS} = \frac{1.5233 - 9x10^{-3} C_{DS}}{1.2x10^6 A_{DS-Air}} \tag{3.25}$$

3.1.2 Methods for Membrane Parameter Estimation

In the present work, the Dymola software® is used to solve the model equations and estimate the membrane transport parameters using an error minimization technique. The model parameters were estimated by minimizing the error between the model output and experimental measurements. For the unsteady state model case, the parameter estimation was performed by solving Eqs. (3.1–3.7) and (3.14–3.25) along with the objective function given below:

$$\min \sum_{t=0} \left[\begin{array}{l} \left| M_{DS,\exp}(t) - M_{DS,\mathrm{mod}}(t) \right| + \left| M_{FS,\exp}(t) - M_{FS,\mathrm{mod}}(t) \right| \\ + \left| C_{DS,\exp}(t) - C_{DS,\mathrm{mod}}(t) \right| + \left| C_{FS,\exp}(t) - C_{FS,\mathrm{mod}}(t) \right| \end{array} \right] \tag{3.26}$$

Subjected to

$$10^{-14} < L_p < 10^{-11} \qquad 0.1 < \sigma < 0.99 \qquad 10^{-6} < k_{DS} < 10^{-2}$$
$$10^{-8} < B < 10^{-6} \qquad 10^{4} < K < 10^{6} \qquad 10^{-6} < k_{FS} < 10^{-2}$$

Where t, Abs, M, and C are the sampling time in [s], absolute value, mass at time t in [kg], and concentration at time t in [kg/m^3], respectively. Subscripts exp and mod refer to the experimentally measured and calculated values from the model equation.

The absolute error minimization is chosen over the least square method because the sum of squared errors gives bigger weight to large errors and lesser weight to small errors. Thus, the least square method is preferred when the range of the output is large. However, absolute difference assigns equal weight to the spread of data. Hence, for our case, since the range is small, we have used absolute error.

For the steady-state parameter estimation, the objective function (Eq. 3.27) is formulated, and model J_W and J_S are found by solving Eqs. (3.1–3.7).

$$\min \sum \left[\left| J_{W,\exp} - J_{W,\mathrm{mod}} \right| + \left| J_{S,\exp} - J_{S,\mathrm{mod}} \right| \right] \tag{3.27}$$

The steady-state J_W and J_S experimental values are calculated by using the following equations:

$$J_{W,\exp} = \frac{V_{DS,Final} - V_{DS,Initial}}{A_M t_{Tot}} = \frac{V_{FS,Initial} - V_{FS,Final}}{A_M t_{Tot}} \tag{3.28}$$

$$J_{S,\exp} = \frac{V_{DS,Initial} C_{DS,Initial} - V_{DS,Final} C_{DS,Final}}{A_M t_{Tot}} = \frac{V_{FS,Final} C_{FS,Final} - V_{FS,mitial} C_{FS,Initial}}{A_M t_{Tot}} \tag{3.29}$$

where A_M and t_{Tot} are the membrane area and duration of the experiment, respectively. Subscripts Final and Initial denote the end and start of the experiment, respectively. The J_W and J_S can be calculated based on either the FS or DS tank

measurements. However, the corresponding J_W and J_S will be different as their respective water evaporation is different.

3.2 Materials and Methods

3.2.1 Experimental Setup for FO Process in Membrane Test Cell

The schematic diagram of the FO experimental setup is shown in Figure 3-2. The membrane test cell with a channel length (L) = 7.25 cm, width (W) = 3.62 cm, DS channel thickness = 0.15 cm, and FS channel thickness = 0.25 cm was purchased from Davey P.L.C., India. A flat sheet thin-film composite membrane with an effective area of 26.244 cm^2 (XLE flat sheet, DOW, USA) was used in conducting all the FO experiments (see Figure A. 1 in the appendix section). A net-type spacer with dimensions L = 7.25 cm and W = 3.62 cm has been inserted in both sides of the membrane to enable proper solution mixing at the membrane surface. The FS and DS were co-currently recirculated using a floating submersible centrifugal pump (Model VND-380-SP1, Lunar Motors, India), and the solution flow rates were independently controlled using a control valve. The solution flow rate was measured using a Micro-Flo flow meter (Model FTB300 Series, Omega Ltd., USA). Both FS and DS were maintained at 31 ± 0.5 °C using a circulating water bath (Model WB 2000V, ANM Industries, India). Two weighing balances (Model SF-400, Virgo, China) were used to measure the masses of solution tanks. The solute concentration was measured using a conductivity meter (Model CON 700, Eutech Instruments, Singapore), and sodium chloride was purchased from Merck Life Science Pvt. Ltd., India. The active membrane area is calculated using the ImageJ (version imageJ2) software, as shown in Figure A. 1 (refer to Appendix). The accuracy of the measuring devices used in this study is reported in Table A. 1 (refer to Appendix).

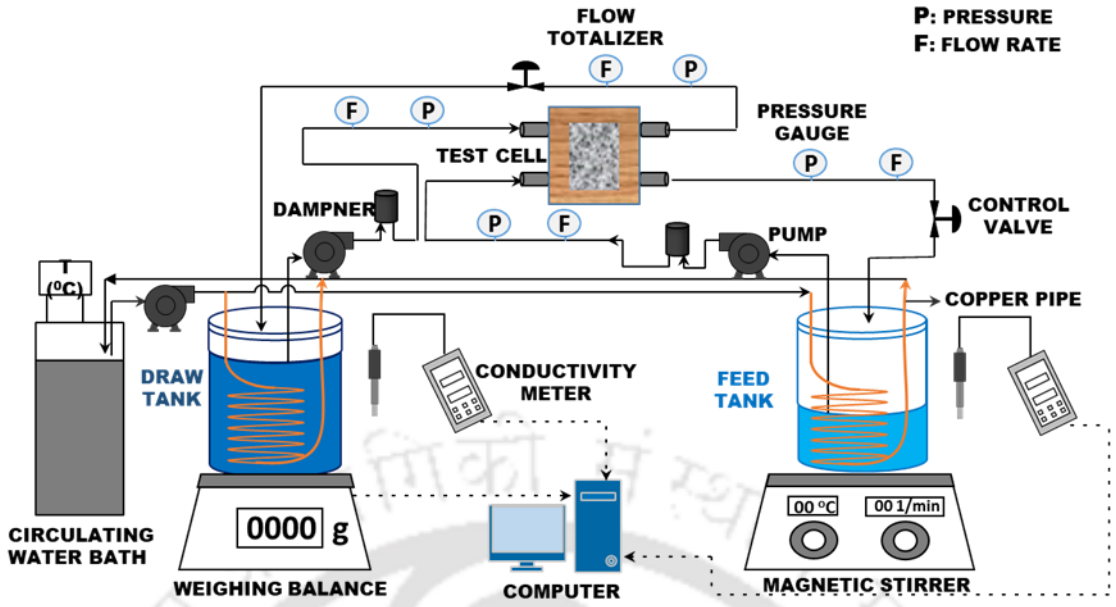

Figure 3-2. Schematic diagram for experimental set up of FO process using test cell

3.2.2 Experimental Methods

The aim of the experiment is to evaluate the errors in membrane transport parameters due to experimental uncertainties such as evaporation loss, variation in solution volume and concentration, for low and high flux FO membranes. For the low flux FO membrane, various experiments are performed in this work, and for the high flux FO membrane, the experimental data are simulated using the parameters adopted from Zhang et al. [113].

For the low water flux membrane, the experiments were run on a bench-scale laboratory system as shown in Figure 3-2. The FS and DS tanks were in open circulating mode. Before conducting the actual FO mode experiment, the membrane was stabilized in RO mode using DI water at 345 kPa for 3 hours. After stabilization, the FO mode experiments were carried out by varying the FS flow rate (Q_{FS}), DS flow rate (Q_{DS}), and DS concentration (C_{DS}). The duration for a single experiment was 10 hours (due to low solvent flux). The changes in mass and concentration of FS and DS were recorded at 20 min intervals. The FO experiments were designed and performed for single C_{FS} (0.05 kg/m^3), different C_{DS} (30, 40, 50 and 100 kg/m^3), Q_{FS} (189.7, 97, and 41.2 L/h), and Q_{DS} (171.6, 91, and 38.8 L/h). All experiments were

carried out at atmospheric pressure and control temperature environment (T_{FS} = T_{DS} = 31.5 °C, and environment temperature ≈ 25 °C and pH ≈ 7). The water and salt flux measurements were repeated three times by using three new membrane pieces made from a single bigger membrane sheet to avoid uncertainties due to the membrane manufacturing process. The experimental flux measurement reported in this work is calculated by taking the average of three experiments with a minimum standard deviation.

3.3 Results and Discussion

3.3.1 Effect of Water Evaporation on the FO Process

Considering the uncertainties in the experimental measurements due to sensors and surrounding environmental conditions, an accurate estimation of water evaporation during the FO experiment is essential. As mentioned in the introduction part, the error due to water evaporation loss has a significant effect on the solvent and solute flux measurements. This effect can be minimized by incorporating the water evaporation loss in the model equations. The water evaporation rates in the open circulatory FO test cell system were experimentally measured for 0.050 kg/m^3 of FS, and 30, 40, and 50 kg/m^3 of DS. The average measured water evaporation rates are reported in Table 3-1. The experiments were performed by circulating the FS and DS through the FO test cell at 31.5 °C. The mass variation of the solution was then recorded every 20 min intervals for 5 hours. All the water evaporation rate measurements were done before conducting the regular FO experiments.

In our investigation, both the Raoult's and modified Raoult's law were not able to predict the evaporation loss as described below. Therefore, the empirical model equations (Eq. 3.24 and Eq. 3.25) were established using experimental data presented in Table 3-1. These empirical equations were used in the mathematical model of the FO process to represent the water evaporation rate from FS and DS tank. The comparison between the experimental results with both the Raoult's law (Case 1) and modified Raoult's law (Case 2) are given below.

Table 3-1. Water evaporation rate with respect to NaCl concentration

Solution	Concentration (kg/m^3)	Water evaporation rate (g/20 min)
FS	0.05	1.97
DS	30	1.25
DS	40	1.17
DS	50	1.07

Note: Q_{FS} = 189.7 L/h, Q_{DS} = 171.6 L/h, $M_{FS,in}$ = 1 kg and $M_{DS,in}$ = 1 kg , T_{DS} = T_{FS} = 31.5 °C and A_M = 2.624x10^{-3} m^2, $T_{surrounding}$ ≈ 25 °C and Humidity = 65 %, Tank surface area available for water evaporation (A) = 13.27 × 10^{-3} m^2.

Case 1: Raoult's law applicability

According to the Raoults' law, the vapour pressure is directly proportional to the mole fraction of the solvent. Thus, when the solute (NaCl) concentration increases, the solvent mole fraction decreases, and this, in turn, reduces the water evaporation, as reported in Table 3-1.

According to the Raoults' law, the vapour pressure is directly proportional to the mole fraction of the solvent.

$$P_w = P_{solvent}\left(1 - x_{solute}\right) \tag{3.30}$$

$$x_{solute} = \frac{n_{solute}}{n_{solvent} + n_{solute}} \tag{3.31}$$

If we consider the feed solution (C_{FS} = 0.05 g/L), its mole fraction roughly will be

$$x_{solute} = \frac{0.05/58.44}{999.95/18 + 0.05/58.44} = 1.54x10^{-5}$$

Since the mole fraction of the solute is too small (dilution solution), the vapour pressure of the mixture can be assumed to be similar to that of the solvent.

Furthermore, the experimentally measured water evaporation rate was validated against the empirical correlation proposed by Rowher [114].

$$J = (125 + 75.5v)(P_w - P_a) \quad (3.32)$$

where J is the water evaporation rate in [g/(m²·h)], v is the air velocity in [m/s], P_w is the vapour pressure at the water surface in [kPa] (which is assumed to follow the Raoult's law), and P_a is the partial pressure of the water vapour in the ambient air in [kPa]. Note that this equation is valid for air velocity range from 0 – 0.67 m/s.

The water evaporation rate was calculated using experimental data such as tank surface area (A) = 13.27 × 10^{-3} m², water vapour pressure at 31.5 °C (P_w) = 4.62 kPa, and partial pressure of water at 25 °C (P_a) = 2.103 kPa. The partial pressure of water was also calculated using humidity data:

$$\%\,\text{humidity} = \frac{P_a(P - P_s)}{P_s(P - P_a)} x100 \quad (3.33)$$

where % humidity = 65, ambient pressure (P) = 101.325 kPa, and saturation pressure at 25 °C (P_s) = 3.2 kPa. Thus, the estimated water evaporation from the FS tank is $\frac{20}{60}(JA)$ = 1.95 g per 20 min, which is close to the experimentally measured water evaporation rate in this study, i.e., 1.97 g per 20 min.

Case 2: Modified Raoult's law applicability

For high salt concentrations, the Raoult's law is modified as

$$P_w = \left(\frac{\gamma}{\varphi}\right) P_{solvent}(1 - x_{solute}) \quad (3.34)$$

where γ and ϕ are the activity and fugacity coefficients, respectively.

If the draw concentrations (say C_{DS} = 30 g/L) is considered, the corresponding activity coefficient would be 0.66 (M. Rad et al., 2012 [115]). Also, if the ambient air is considered as an ideal gas (ϕ = 1), the vapour pressure of the mixture will be 3.02 kPa. Thus, for a given tank surface area of 13.27 × 10^{-3} m² and an experimental duration of 20 min, the corresponding water evaporation will be 0.709 g. However, this result underestimates the experimental result (i.e., 1.25 g).

From both cases, we can conclude that

- For dilution solutions such as feed solution, the Raoult's law can be applicable. However, in our work, the Raoult's law along with the empirical correlation proposed by Rowher was used to validate the experimental FS side evaporation rate.
- For concentrated solutions such as draw solution, the solution can be treated as a non-ideal solution. However, the applicability of modified Raoult's law underestimates the experimental results.

3.3.2 Membrane Parameters Estimation

The objective functions (Eq. 3.26 and Eq. 3.27) were minimized using the Dymola design calibration function, which uses a successive quadratic programming technique for error minimization. The bounds for the model parameters estimation were:

$$10^{-14} < L_p < 10^{-11} \qquad 0.1 < \sigma < 0.99 \qquad 10^{-6} < k_{DS} < 10^{-2}$$
$$10^{-8} < B < 10^{-6} \qquad 10^{4} < K < 10^{6} \qquad 10^{-6} < k_{FS} < 10^{-2}$$

The water permeability coefficient (L_p) of the membrane was estimated to be 0.0842 × 10^{-12} $m^3/(m^2\ s\ Pa)$ using the unsteady state FO mode data. For cross-checking this result, the L_p was also estimated in RO mode. To estimate the L_p in the RO mode, distilled water was pressurized through a preconditioned membrane at different pressures. The permeate flux was then recorded with respect to the applied hydraulic pressure. The slope for the plot between the hydraulic pressure (in the x-axis) and the water flux (in the y-axis) gives the L_p. As shown in Figure A. 2 (refer to appendix), the L_p in RO mode was estimated to be 0.082 × 10^{-12} $m^3/(m^2\ s\ Pa)$. This value was close to the water permeability estimated using the unsteady state FO mode data.

The deviations in the estimated parameters between the steady and unsteady state model approaches were analyzed further with respect to the experimental uncertainties in subsequent sections.

3.3.2.1 Case 1: Unsteady State Model Prediction

The unsteady state FO membrane model predictions incorporating the presence of water evaporation term in the main design equations are shown in Figure 3-3, Figure 3-4, and Figure 3-5. From the experimental observation, the FS tank mass decreased at a higher rate than usual, and the DS tank mass decreased instead of increasing. Both unusual phenomena were due to the dominance of the water evaporation over the FO water flux. For low flux FO membrane experiments, C_{FS} has varied up to 114 % (from 0.05 to 0.107 kg/m^3 in 10 hours) and C_{DS} up to 3 %. The DS concentration presented in Figure 3-5 (a) looks flat due to a slight change in DS concentration and wider range used for Y-axis. To see the changes in the DS concentration, one can refer to Figure 3-3 (a), Figure 3-4 (a), and Figure 3-6 (a).

The proposed model equations in this study were able to predict the mass and concentration variations of solutions in the tank with maximum relative errors of 3.7 and 5.7 %, respectively. The variation in both C_{FS} and C_{DS} is expected to be more for the high flux FO membrane.

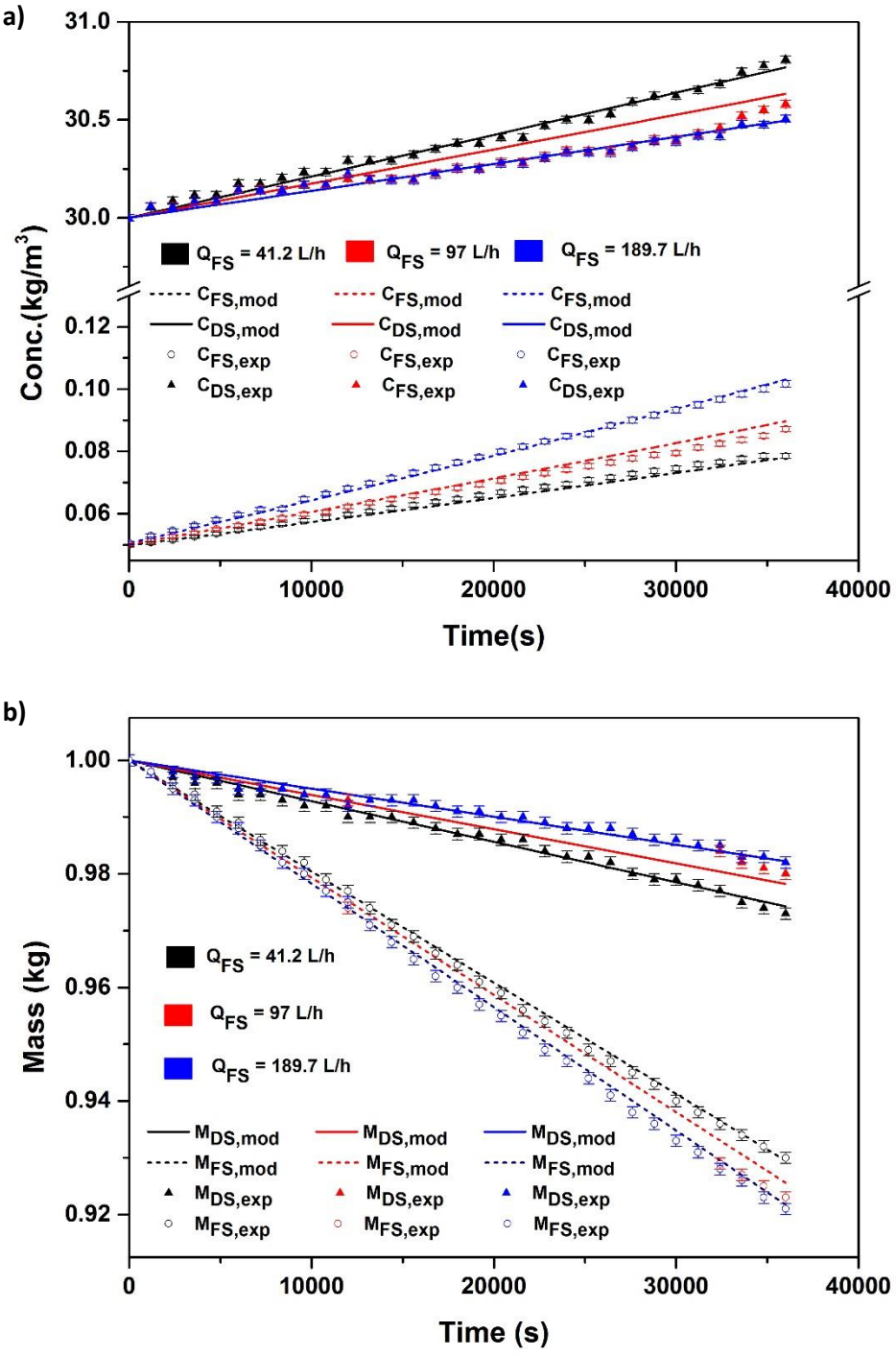

Figure 3-3. Unsteady state model prediction with respect to Q_{FS}. [Note: Q_{DS} = 171.6 L/h, $C_{FS,in}$ = 0.05 kg/m^3, $C_{DS,in}$ = 30 kg/m^3, and $M_{FS,in}$ = $M_{DS,in}$ = 1 kg]

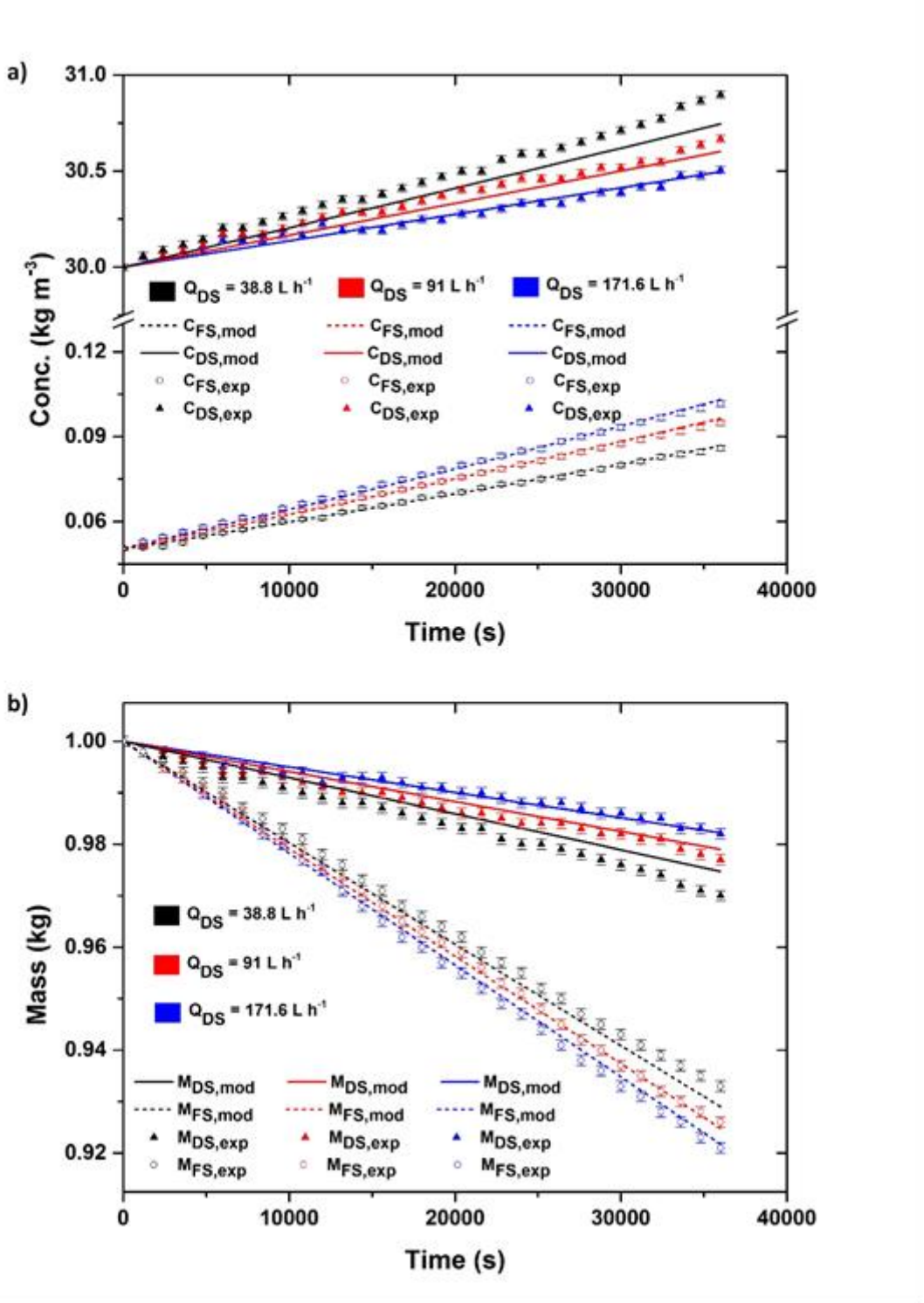

Figure 3-4. Unsteady state model prediction with respect to Q_{DS}. [Note: Q_{FS} = 189.7 L/h, $C_{FS,in}$ = 0.05 kg/m^3, $C_{DS,in}$ = 30 kg/m^3, and $M_{FS,in} = M_{DS,in}$ = 1 kg]

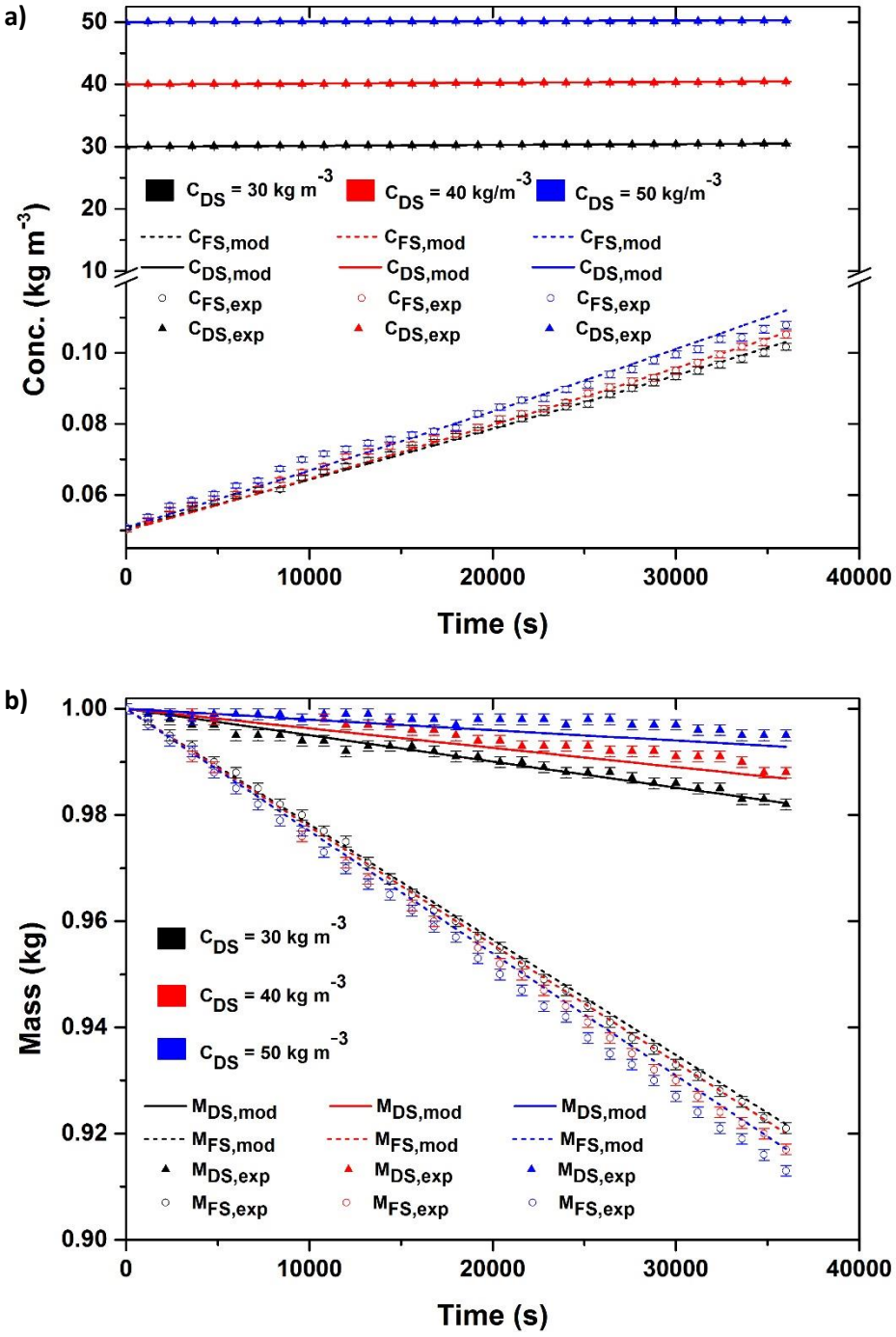

Figure 3-5. Unsteady state model prediction with respect to C_{DS}. [Note: Q_{FS} =189.7 L/h and Q_{DS} =171.6 L/h; $C_{FS,in}$ = 0.050 kg/m^3; $C_{DS,in}$ = 30, 40 and 50 kg/m^3; $M_{FS,in}$ = $M_{DS,in}$ = 1 kg]

3.3.2.2 Case 2: Steady-State Model Prediction

The steady-state model predictions in the presence and absence of water evaporation terms are presented in Table 3-2. The J_W and J_S were calculated using average solution volume and concentration, respectively, for various Q_{FS} and Q_{DS}. In the absence of water evaporation term in the design equations, the maximum error in J_W was found to be 744 % (refer to Table 3-2). The deviations between the model parameters of steady and unsteady state cases are listed in Table 3-3 and Table 3-4.

The steady-state based J_W and J_S were found to have maximum deviations of 390.5 and 6.9 %, respectively, in comparison to the unsteady state-based model in the presence of water evaporation. The deviations are mainly due to the water evaporation and solution concentration variation. Therefore, such errors in the solvent and solute permeability may result in erroneous plant design. For instance, the designed production rate could not be achieved when higher permeability values are used.

Table 3-2. Experimental versus model comparison for solvent and solute fluxes using the steady-state model

C_{FS} (kg/m³)	C_{DS} (kg/m³)	Q_{FS} (L/h)	Q_{DS} (L/h)	$J_{W\,exp}$ Case 1 x 10^7 (m³/(m² s))	$J_{S\,exp}$ Case 1 x 10^7 (kg/(m² s))	$J_{W\,mod}$ Case 1 x 10^7 (m³/(m² s))	$J_{S\,mod}$ Case 1 x 10^7 (kg/(m² s))	Error in J_W (%)	Error in J_S (%)	$J_{W\,exp}$ Case 2 x 10^7 (m³/(m² s))	Error in J_W^* (%)
0.064	30	189.7	171.6	2.11	4.56	2.05	4.73	2.84	3.73	8.36	296
0.064	30	97.0	171.6	1.89	3.21	1.64	3.49	13.23	8.72	8.15	331
0.064	30	41.2	171.6	1.15	2.45	1.22	2.40	6.09	2.04	7.41	544
0.064	30	189.7	91.0	1.58	3.95	1.72	4.13	8.86	4.56	7.83	396
0.064	30	189.7	38.8	0.84	3.16	1.19	3.22	41.67	1.90	7.09	744
0.064	40	189.7	171.6	2.53	4.91	2.23	5.02	11.86	2.24	8.78	247
0.064	50	189.7	171.6	2.95	5.03	2.53	5.50	14.24	9.34	9.21	212

Note: Case 1: presence of water evaporation: $\text{Error in } J_W(\%) = 100\left|\frac{J_{W,\text{exp},Case1} - J_{W,\text{mod},Case1}}{J_{W,\text{exp},Case1}}\right|$ $\text{Error in } J_S(\%) = 100\left|\frac{J_{S,\text{exp},Case1} - J_{S,\text{mod},Case1}}{J_{S,\text{exp},Case1}}\right|$

Case 2: absence of water evaporation: $\text{Error in } J_W^*(\%) = 100\left|\frac{J_{W,\text{exp,Case 2}} - J_{W,\text{exp,Case1}}}{J_{W,\text{exp,Case1}}}\right|$

Table 3-3. Steady and unsteady state parameter estimation with respect to FS and DS flow rate for low water flux FO membrane

	Maximum flow of both solution (L/h) Q_{FS} = 189.7 and Q_{DS} = 171.6			Feed Flow Rate Change (L/h) Q_{FS} = 97 and Q_{DS} = 171.6			Q_{FS} = 41.2 and Q_{DS} = 171.6			Draw Flow Rate Change (L/h) Q_{FS} = 189.7 and Q_{DS} = 91			Q_{FS} = 189.7 and Q_{DS} = 38.8		
Membrane parameters	Case I	Case II	Error (%)	Case I	Case II	Error (%)	Case I	Case II	Error (%)	Case I	Case II	Error (%)	Case I	Case II	Error (%)
$Lpx10^{12}$ ($m^3/(m^2\ s\ Pa)$)	0.084	0.412	390.5	0.084	0.412	390.5	0.084	0.412	390.5	0.084	0.412	390.5	0.084	0.412	390.5
$Bx10^7$ ($m^3/(m^2\ s)$)	0.204	0.190	-6.9	0.204	0.190	-6.9	0.204	0.190	-6.9	0.204	0.190	-6.9	0.204	0.190	-6.9
σ (-)	0.954	0.999	4.7	0.954	0.999	4.7	0.954	0.999	4.7	0.954	0.999	4.7	0.954	0.999	4.7
$Kx10^{-5}$ (s/m)	4.385	3.461	-21.1	4.385	3.461	-21.1	4.385	3.461	-21.1	4.385	3.461	-21.1	4.385	3.461	-21.1
k_{DS} x 10^5 (m/s)	1.235	1.235	0.0	1.235	1.235	0.0	1.235	1.235	0.0	0.905	0.905	0.0	0.595	0.595	0.0
k_{FS} x 10^5 (m/s)	1.298	1.298	0.0	0.933	0.933	0.0	0.613	0.613	0.0	1.298	1.298	0.0	1.298	1.298	0.0

Case 1: estimated using the unsteady-state model (Eqs. (3.1–3.7) and (3.14–3.27))

Case 2: estimated using the steady-state model (Eqs. (3.1–3.7) and (3.14–3.15))

Note: $C_{FS,in}$ = 0.050 kg/m^3, $C_{DS,in}$ = 30 kg/m^3, $M_{FS,in}$ = $M_{DS,in}$ = 1 kg, T_{DS} = T_{FS} = 31.5 °C and A_M = 2.624 $x10^{-3}$ m^2

Table 3-4. Steady and unsteady state parameter estimation with respect to DS concentration for low flux FO membrane

Membrane parameters	Concentration								
	30 kg/m^3			40 kg/m^3			50 kg/m^3		
	Case 1	Case 2	Error (%)	Case 1	Case 2	Error (%)	Case 1	Case2	Error (%)
Lp x 10^{12} (m^3/(m^2 s Pa))	0.084	0.412	390.5	0.084	0.412	390.5	0.084	0.412	390.5
B x10^7 (m^3/(m^2 s))	0.204	0.190	-6.9	0.204	0.190	-6.9	0.204	0.190	-6.9
σ	0.954	0.999	4.7	0.954	0.999	4.7	0.954	0.999	4.7
K x 10^{-5} (s/m)	4.385	3.461	-21.1	4.385	3.461	-21.1	4.385	3.461	-21.1
k_{DS} x 10^5 (m/s)	1.235	1.235	0.0	1.338	1.341	0.2	1.368	1.386	1.3
k_{FS} x 10^5 (m/s)	1.298	1.298	0.0	1.298	1.298	0.0	1.298	1.298	0.0

Case 1: estimated using the unsteady-state model (Eqs. (3.1–3.7) and (3.14–3.27))

Case 2: estimated using the steady-state model (Eqs. (3.1–3.7) and (3.14–3.15))

Note: Q_{FS} =189.7 L/h and Q_{DS} =171.6 L/h, $C_{FS,in}$ = 0.05 kg/m^3, $M_{FS,in}$ = $M_{DS,in}$ = 1 kg, T_{DS} = T_{FS} = 31.5 °C and A_M = 2.624 x10^{-3} m^2

$$\text{Error}(\%) = 100\left(\frac{\text{Case 2} - \text{Case 1}}{\text{Case 1}}\right)$$

3.3.3 Error Analysis with respect to Low Flux FO Membrane

3.3.3.1 Effect of FS and DS Flow Rates on Mass Transfer Coefficient (k_{FS} and k_{DS}) and Solute and Solvent Fluxes

To study the effect of Q_{FS} and Q_{DS} on k_{FS}, k_{DS}, J_W, and J_S, the FO experimental results were analyzed at various Q_{FS} = 187.9, 97, 42.2 and Q_{DS} =171.6, 91, 38.8 L/h. When Q_{FS} was increased from 41.2 L/h to 97, and then to 189.7 L/h, the k_{FS} has increased as described in model Eq. 3.13. The improvement in the k_{FS} was owing to $\exp\left(J_W/k_{FS}\right)\approx 1$, i.e., the bulk FS concentration ($C_{FS,b}$) is nearly equal to the membrane surface concentration ($C_{FS,m}$). This phenomenon improves the effective solute concentration difference ($C_{DS,m} - C_{FS,m}$), which in turn improves the J_W and J_S, according to Eq. 3.1 and Eq. 3.2 as presented in Table 3-5 (a). Generally, when the solution flow rate increases, there will be more turbulence near the membrane surface, which decreases the solute accumulation on the membrane surface. Thus, the migration of more solute from the DS into the FS side increases and results in the increment of concentration at the FS side.

Similarly, when Q_{DS} was increased from 38.8 to 91 and then to 171.6 L/h, both the k_{DS} (Table 3-3) and the J_W (Table 3-5 (b)) has increased owing to the same reason mentioned above. However, the effect of Q_{DS} on J_W and J_S was higher than that of Q_{FS} as shown in Table 3-5 (a) and (b). For instance, changing Q_{DS} from 171.6 to 38.8 L/h resulted in 15.19 and 30.59 % reduction in J_W and J_S, respectively, whereas changing Q_{FS} from 189.7 to 41.2 L/h resulted in 11.39 and 46.30 % reduction in J_W and J_S, respectively. Thus, optimization of the operating conditions such as Q_{FS} and Q_{DS} is very important to improve the performance of FO processes.

Table 3-5 (a). Effect of FS flow rate on solvent and solute fluxes

FS Flow Rate	Mass change in FS tank per hour	Mass change in DS tank per hour	Avg. Water flux (Eq. 3.28)	Concentration change in FS tank per hour	Concentration change in DS tank per hour	Avg. Reverse Solute Flux (Eq. 3.29)
Q_{FS} (L/h)	ΔM_{FS} (g/h)	ΔM_{DS} (g/h)	$J_W \times 10^7$ ($m^3/m^2.s$)	ΔC_{FS} (mg/L)	ΔC_{DS} (mg/L)	$J_S \times 10^7$ ($Kg/m^2.s$)
189.7	1.99	1.95	8.3598	5.110	50.604	4.5572
97.0	1.79	1.75	8.1481	3.951	58.134	3.2048
41.2	1.09	1.05	7.4074	2.816	80.871	2.4469

Note: Q_{DS} = 171.6 L/h,.$C_{FS,in}$ = 0.050 kg/m^3, $C_{DS,in}$ = 30 kg/m^3, $M_{FS,in}$ = $M_{DS,in}$ = 1 kg, T_{DS} = T_{FS} = 31.5 °C and A_M = 2.624x10^{-3} m^2

Table 3-5 (b). Effect of DS flow rate on solvent and reverse solute fluxes

DS Flow Rate	Mass change in FS tank per hour	Mass change in DS tank per hour	Avg. Water flux (Eq. 3.28)	Concentration change in FS in tank per hour	Concentration change in DS tank per hour	Avg. Reverse Solute Flux (Eq. 3.29)
Q_{DS} (L/h)	ΔM_{FS} (g/h)	ΔM_{DS} (g/h)	$J_W \times 10^7$ ($m^3/m^2.s$)	ΔC_{FS} (mg/L)	ΔC_{DS} (mg/L)	$J_S \times 10^7$ ($Kg/m^2.s$)
171.6	1.99	1.95	8.360	5.110	50.604	4.557
91.0	1.49	1.45	7.831	4.430	66.808	3.945
38.8	0.79	0.75	7.090	3.565	89.702	3.163

Note: Q_{FS} = 189.7 L/h,.$C_{FS,in}$ = 0.050 kg/m^3, $C_{DS,in}$ = 30 kg/m^3, $M_{FS,in}$ = $M_{DS,in}$ = 1 kg, T_{DS} = T_{FS} = 31.5 °C and A_M = 2.624x10^{-3} m^2

The model parameters were estimated using an experimental data set of Q_{FS} = 189.7 and Q_{DS} = 171.6 L/h. The estimated parameters were validated using an experimental data set of Q_{FS} = 97, 42.2 and Q_{DS} = 91, 38.8 L/h as shown in Table 3-5. The effect of Q_{FS} and Q_{DS} on the k_{FS} and k_{DS} were also validated with the mass transfer coefficients obtained from correlation (Eq. 3.13) as reported in Table 3-6 [116]. The maximum relative error between the correlation and model output was found to be 7.63 % for λ = 0.00891 and k_b = 0.541. The sensitivity of the estimated parameters was studied by interchanging the data set used for parameter estimation and validation. The sensitivity results concluded that parameters were not varying with respect to the data sets.

Table 3-6. Mass transfer coefficient comparison between correlation and model results

Flow rate (L/h)	Estimated mass transfer coefficient from experimental data k_{exp} x 10^5 (m/s)	Predicted mass transfer coefficient using Eq. 3.13 k_{model} x 10^5 (m/s)	Relative Error (%)
171.6	1.235	1.329	7.63
91	0.905	0.943	4.23
38.8	0.595	0.595	0.00
189.7	1.295	1.295	0.00
97	0.933	0.901	3.42
41.2	0.613	0.567	7.47

Note: Estimated λ = 0.00891 and k_b = 0.541

3.3.3.2 Effect of Draw Concentration on Membrane Parameters (B, k_{DS} and k_{FS})

To study the effect of solution concentration in the membrane transport parameters such as B, k_{FS}, and k_{DS}, experiments were performed for C_{DS} = 30, 40, and 50 kg/m^3 at Q_{FS} = 189.7 L/h and Q_{DS} = 171.6 L/h. The experimental data set of C_{DS} = 30 kg/m^3 was used for parameter estimation and the experimental data set of C_{DS} = 40 and 50

kg/m^3 were used for validation. With increasing C_{DS}, the k_{DS} and B are expected to vary. Therefore, both parameters were tuned during the parameter estimation. The corresponding results are presented in Table 3-4. As indicated in the table, when C_{DS} was increased, the k_{DS} has increased for both unsteady and steady-state cases. The slight improvement in k_{DS} was due to $C_{DS,m} \approx C_{DS,b}$. However, the solute permeability was found to be the same.

3.3.3.3 Simulation of Membrane Test Cell in the Presence of Water Evaporation

To study the effect of water evaporation on M_{FS}, M_{DS}, C_{FS}, and C_{DS}, the unsteady state model of FO membrane test cell was simulated in the presence and absence of water evaporation term for the condition $C_{FS,in}$ = 0.05 kg/m^3, $C_{DS,in}$ = 50 kg/m^3, Q_{FS} = 189.7 L/h, and Q_{DS} = 171.6 L/h. Unlike the experimental results, the simulation results for the M_{DS} and M_{FS} were increasing and decreasing, respectively, and vice versa for both C_{DS} and C_{FS}, as shown in Figure 3-6. These contradicting phenomena led to a large error in the estimated parameters. Thus, the use of the unsteady state model and the inclusion of the water evaporation model were essential to minimize the error in the estimated membrane transport parameters.

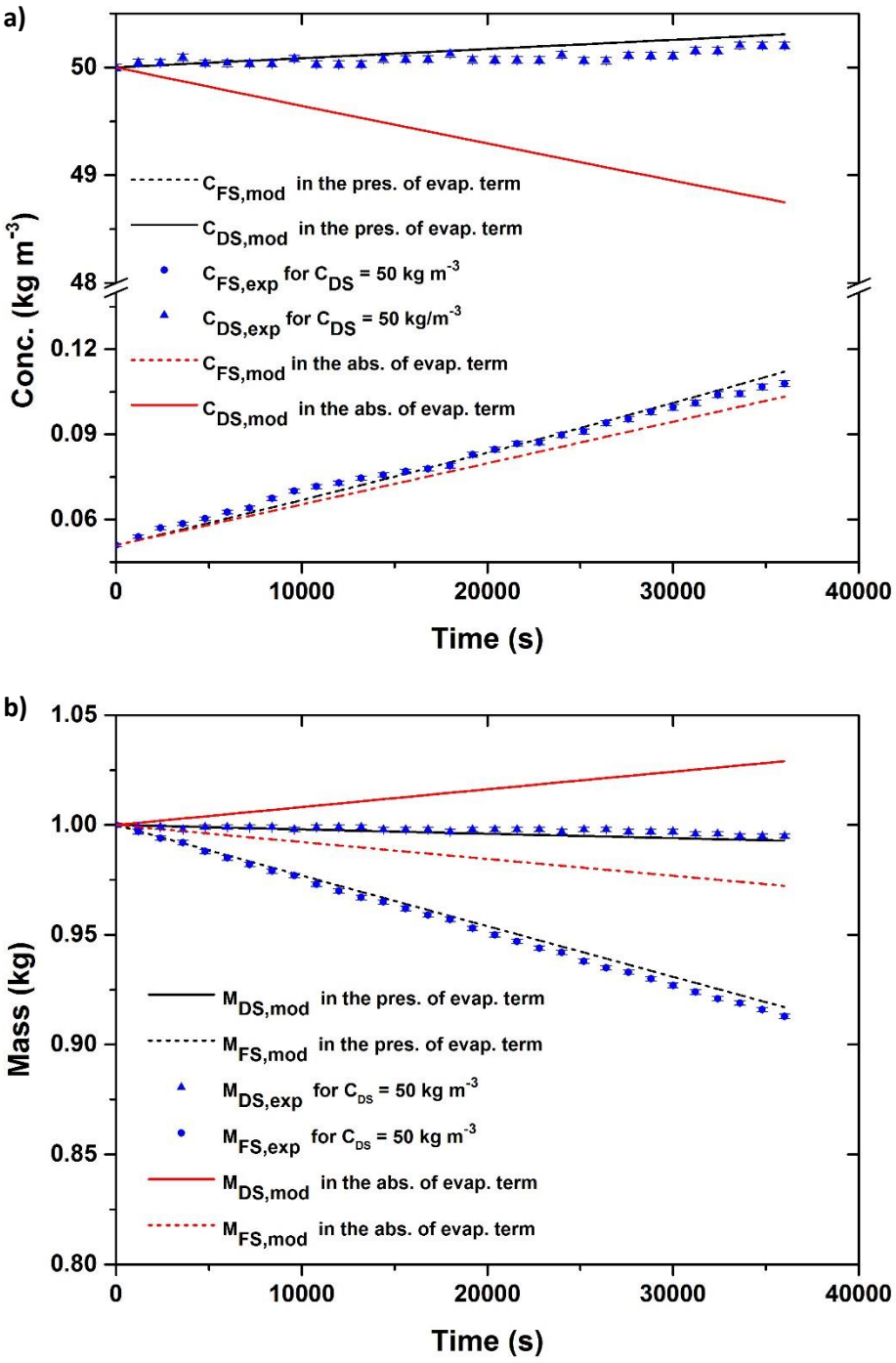

Figure 3-6. Experimental and model comparison in solution (a) concentration and (b) mass for both FS and DS in the presence and absence of evaporation loss at Q_{FS} = 189.7 L/h and Q_{DS} = 171.6 L/h. Note: $C_{FS,in}$ = 0.050 kg/m^3, $C_{DS,in}$ = 50 kg/m^3, $M_{FS,in}$ = 1 kg, and $M_{DS,in}$ = 1 kg [pres. = presence, abs = absence and evap. = evaporation].

3.3.4 Error Analysis in the Presence/Absence of Water Evaporation with Respect to High Water Flux FO Membrane

The FO experimental duration is short for the high-water flux case, and this reduces the corresponding water evaporation time. Hence, the error on the membrane parameter estimation in the presence and absence of water evaporation term are expected to decrease for high water flux FO membrane. For the FO experiment with a shorter duration, the use of a significant amount of DS volume improves the water flux measurement accuracy. In another aspect, a combination of high flux and low DS volume can lead to a significant variation in the DS concentration, and this phenomenon will add more experimental errors in flux measurement. A specific combination of solution volume and concentration is expected to minimize the error in flux measurement. Therefore, for a given FO membrane and DS concentration, the use of optimal tank volume is critical to achieving minimal errors in the experimental flux measurement. In this section, the effect of FS and DS tank volumes on the high flux FO membrane is analyzed in detail.

The mass and concentration profiles for both FS and DS tanks were simulated using high flux FO membrane parameters given in Zhang et al. [113] (refer to Table 3-7). The parameters, k_{FS} and k_{DS}, are taken from the current experimental study as given in Table 3-4. Apart from the parameters given by Zhang et al., the following experimental conditions were also used: Q_{FS} = 189.7 L/h and Q_{DS} = 171.6 L/h; tank volume = 1, 2, 5, and 10 L; C_{DS} = 1.5 and 2 M, and C_{FS} = deionized water.

The estimated membrane parameters with respect to tank volumes in the presence and absence of water evaporation terms are summarised in Table 3-7 (a) and (b). Here, the estimated parameters were deviating from the actual parameters. The deviations might be observed due to the volume and concentration variation during the FO simulations. According to the FO test cell experimental procedure, the effect of both uncertainties cannot be ignored during the FO experiments. The estimated errors in the model parameter, such as L_p in the absence and presence of water evaporation terms, were observed to be 26.8 and 0.92 %, respectively, for 1 L solution

volume. Moreover, for the DS-based measurement, the error in the L_p was reduced from 19.27 to 16.28 % when the tank volume increased from 1 L to 10 L.

Furthermore, as indicated in Table 3-7 (a), DS-based J_W and J_S measurements provided less error in the model parameters compared to the FS-based measurements. For example, while increasing the tank volume from 1 L to 10 L, the estimated error in the L_p varied from 19.27 to 16.28 % for DS-based measurements and from 26.8 to 24.1 % for FS-based measurements. The above-reported error value is mainly due to the water evaporation rate difference between FS and DS. However, the proposed model in this work includes both the water evaporation term and concentration variation in the model equation. Therefore, the errors in model parameters (L_p and B) are reduced to 1.02 and 1.45 %, respectively.

Table 3-7 (a). Tank volume effect on membrane parameters in the absence of water evaporation term

Parameter	Reference parameter [113]	DS Based Measurement				Error (%)				FS Based Measurement				Error (%)			
		1 L	2 L	5 L	10 L	1 L	2 L	5 L	10 L	1 L	2 L	5 L	10 L	1 L	2 L	5 L	10 L
$L_p x10^{12}$ ($m^3/(m^2\ s\ Pa)$)	4.36	3.52	3.55	3.57	3.65	19.27	18.58	18.12	16.28	5.53	5.45	5.43	5.41	26.8	25.0	24.5	24.1
B $x10^7$ ($m^3/(m^2\ s)$)	0.88	0.68	0.70	0.71	0.73	22.73	20.46	19.32	17.05	1.06	1.04	1.04	1.03	20.5	18.2	17.9	17.0
σ (-)	0.99	0.99	0.99	0.99	0.99	0	0	0	0	0.99	0.99	0.99	0.99	0	0	0	0
K $x10^{-5}$ (s/m)	1.23	1.12	1.13	1.14	1.17	8.94	8.13	7.32	4.88	0.99	0.99	1.01	1.02	19.5	19.5	17.9	17.1

Table 3-7 (b). Tank volume effect on membrane parameters in the presence of water evaporation term

Parameter	Reference parameter [113]	DS/FS Based Measurement				Error (%)			
		1 L	2 L	5 L	10 L	1 L	2 L	5 L	10 L
$L_p x10^{12}$ ($m^3/(m^2\ s\ Pa)$)	4.36	4.32	4.33	4.33	4.36	0.92	0.69	0.69	0
B $x10^7$ ($m^3/(m^2\ s)$)	0.88	0.87	0.87	0.87	0.88	1.14	1.14	1.14	0
σ (-)	0.99	0.98	0.98	0.98	0.99	1.01	1.01	1.01	0
K $x10^{-5}$ (s/m)	1.23	1.22	1.22	1.22	1.22	0.81	0.81	0.84	0.84

Note: FS/DS based measurement means when we use FS/DS data for calculating J_W and J_S

C_{DS} = 1.5 M and 2.0 M, $C_{FS,in}$ = DI water, Q_{FS} = 189.7 L/h, Q_{DS} = 171.6 L/h, $T_{DS} = T_{FS}$ = 23.0 °C and A_M = 2.624 $x10^{-3}$ m^2

$$\text{Error}\,(\%) = 100\left|\frac{\text{Parameter}_{\text{at given solution volume}} - \text{Parameter}_{\text{Initial}}}{\text{Parameter}_{\text{Initial}}}\right|$$

3.4 Summary

In this chapter, the FO mathematical model was developed for a membrane test cell by combining the model equations such as membrane transport, concentration polarization, and unsteady state tank mass balance. The water evaporation loss from the solution tank was experimentally investigated and incorporated in the unsteady-state tank mass balance equations. Then, the mass and concentration variations in FS and DS tanks were used to estimate the FO membrane transport parameters and mass transfer coefficients. The errors in membrane transport parameters due to experimental uncertainties such as water evaporation, variation in solution volume and concentration, for low and high flux FO membranes were evaluated and compared. Based on the experimental and simulation analysis, the incorporation of the water evaporation rate model and the dynamic nature of DS and FS properties in the FO model equations could reduce the overall error in the estimated membrane transport parameters. The proposed model equations in this study were able to predict the mass and concentration variations of solutions in the tank with maximum relative errors of 0.37 and 5.69 %, respectively.

Chapter 4 Experimentation, Modeling and Optimization Studies on Axial Flow Hollow Fiber Forward Osmosis Module

Parts of this Chapter is published as research articles:

- **H. Teklu**, D. K. Gautam, and S. Subbiah, Axial flow hollow fiber forward osmosis module analysis for optimum design and operating conditions in desalination applications, Chem. Eng. Sci., vol. 216, p. 115494, 2020

Experimentation, Modeling and Optimization Studies on Axial Flow Hollow Fiber Forward Osmosis Module

This chapter presents the mathematical model for the axial flow hollow fiber FO membrane module. The solution diffusion (SD) model is integrated with ICP and ECP equations on both sides of the membrane. Then, it states all the assumptions made to develop the mass and momentum balance equation for the axial flow HF FO module. In this chapter, the applicability of the Ergun equation and Hagen-Poiseuille equations for estimating the pressure drop across the shell and lumen side have been experimentally investigated, respectively. Also, a simple tank model has been developed to study the batch FO process. In addition, the performance of the HF FO membrane has been evaluated with respect to net permeate flow rate, total power consumption, and specific energy consumption. Further, a multi-objective optimization (MOO) problem is formulated owing to the conflicting nature of maximizing the net permeate flow rate and minimizing the power consumption. Finally, a two-step procedure is developed for identifying the optimal solution from a given pilot-scale experiment.

4.1 Theory

4.1.1 Overview of Axial flow Hollow Fiber FO Module

In this work, the axial flow Toyobo HF FO module is used for batch FO experimental studies. The flow configuration of the HF FO module is shown in Figure 4-1. The DS and FS are passing through the shell and tube sides of the Toyobo HF module, respectively. As a result of continuous DS dilution and FS concentration, a non-uniform osmotic driving force is present along the length of the module. However, unlike the radial flow HF FO mathematical model, which has been studied thoroughly with experimental validation, the axial flow HF FO module performance is not exhaustively studied with experimental model validation. Hence, developing a precise mathematical model for the axial flow HF FO model is very important to predict and optimize the performance of the axial flow HF FO process.

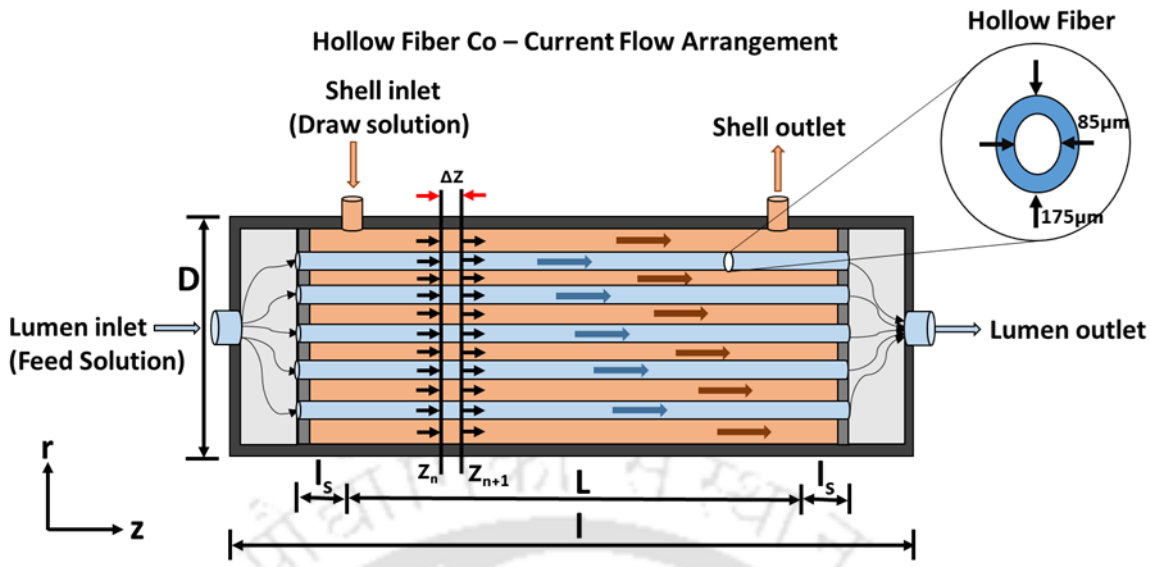

Figure 4-1. Hollow fiber forward osmosis module in co-current flow configuration

4.1.1.1 The Objective of the Axial flow Hollow Fiber FO Model

The mathematical model proposed in this work is intended to be used for the validation of FO experimental results in the first phase. Then, the validated model will be used for the optimization of the HF FO module design and operating condition. The following important phenomena that take place during the experimental study have to be included in the model equations.

(i) The FO process parameter such as flow, pressure and solute concentration is expected to vary along the HF FO module length. Hence, the model should be able to calculate such a variation.

(ii) The internal and external concentration polarization phenomena across the membrane layer have a significant effect on the FO membrane performance. Thus, these effects should be incorporated using an appropriate concentration polarization model.

(iii) The FO experiments are performed in batch mode. Therefore, the integrated HF FO, feed and draw solution tank model should be capable of calculating the dynamic variation of mass and concentration of draw and feed solution in respective tanks.

4.1.1.2 Modeling of HF FO Batch Process

The mathematical model of an axial flow HF FO module used in this thesis is expected to calculate the net permeate flow rate for a given operating condition such as inlet flow rate, concentration, and pressure of the FS and DS, and model parameters such as the FO membrane properties, module dimensions and coefficients of empirical correlation. The steady-state model of the HF FO module is developed by integrating mass and momentum balance equations across fiber lumen and shell side with appropriate boundary conditions derived from the solute and solvent flux equation for dense layer and concentration polarization equation for both the support layer and membrane surface.

The batch mode FO experimental data is used for both experimentation and validation of the FO mathematical model developed in this study. The FO mathematical model combines both the unsteady state tank model and the steady-state HF FO module model. The tanks (refer to Figure 4-3), which act as continuous sources and sinks to the HF FO module, are formulated as an unsteady state model owing to the continuous change in the tank solution concentration and volume.

The concentration and flow rate of FS and DS are expected to vary across the module length, and by assuming uniform fiber distribution across the radial position, the variation in the radial direction is assumed to be negligible. Also, the residence time of FS (0.094 s) and DS (0.42 s) in the HF module is lower than the FS and DS tank resistance, i.e., the response of the HF FO module is observed to be faster than both FS (223 s) and DS (163 s) tank at the standard operating condition. Therefore, 1-dimensional (ID) unsteady state FO model equation is solved and validated using batch experimental data generated in this work along with the tank model. The validated model is used to improve the FO module performance by maximizing the net permeate flow rate and minimizing the power consumption while manipulating the operational condition (pressure and flow rate) and design variable (module length).

4.1.1.3 Assumptions Taken While Developing the 1D HF FO Model

The following assumptions are made to develop the 1D HF FO model by solving the mass and momentum balance equations along with the axial direction local membrane transport equation.

(i) Hollow fibers are uniformly distributed along the radial direction.

(ii) No-slip boundary condition is applicable for membrane surface.

(iii) The HF FO module is packed uniformly across the radial direction such that mass and momentum variation in the radial direction is negligible.

(iv) The forward flux of the feed component to the draw side is negligible, and the same is confirmed through experimental results.

(v) The solution diffusion model is used for describing solvent and solute flux across the dense layer because the reflection coefficient of Toyobo's FO membrane is considered as one.

(vi) Concentration polarization exists inside the support layer and both FS and DS side membrane surface.

(vii) Flow across the HF bundle is assumed as equivalent to flow across the structured packed bed, such that the modified Ergun equation is used to calculate pressure drop across the module shell side.

(viii) Flow inside the lumen side is laminar such that the Hagen-Poiseuille is used for lumen side pressure drop calculation and experimentally verified that within the operating range of the HF FO module (i.e., Feed flow rate 9 – 120 LPH). The Hagen-Poiseuille equation is applicable for laminar flow conditions, Re < 2100.

4.1.2 Flux Equations for FO Membrane

The solution diffusion (SD) model is a two-parameter model which is used to describe the transport phenomena of solvent and solute through a homogeneous dense membrane [11,35–38]. In the SD model, the solvent and solute flux through the membrane is defined by two parameters: water permeability coefficient (A) and

solute permeability coefficient (B). The estimation of both parameters using the experimental method is essential to characterize the membrane performance.

The SD governing equations, which are used to describe water and solute fluxes in the FO process, are

$$J_W = A\left[\frac{iRT}{M_W}\left(C_{DS,m} - C_{FS,m}\right) - \left(P_{DS} - P_{FS}\right)\right] \quad (4.1)$$

$$-J_S = B\left[C_{DS,m} - C_{FS,m}\right] \quad (4.2)$$

Where, J_W, J_S, A, B, $C_{DS,m}$, $C_{FS,m}$, i, R, T and M_W are water flux in [$m^3/(m^2\ s)$], solute flux in [$kg/(m^2\ s)$], water permeability coefficient [$m^3/(m^2\ s\ Pa)$], solute permeability coefficient in [$m^3/(m^2\ s)$], concentration of DS at membrane surface in [kg/m^3], concentration of FS at membrane surface in [kg/m^3], ionization number of the solution, universal gas constant in [$(m^3\ Pa)/(mol\ K)$], temperature of solution in [°K] and molecular weight of DS in [g/mol], respectively. P_{DS} and P_{FS} are the hydraulic pressure in [Pa] for DS and FS sides, respectively. Here, the water flux is expressed in terms of concentration based on Van't Hoff's theory.

In FO, the concentration gradient that exists across the membrane is responsible for solute penetration through it. Since the concentration of the DS side is more than the FS side, the flow direction of solute flux is opposite to that of water flux, as expressed in Eq. 4.2.

4.1.3 Concentration Polarization Models with Solution Diffusion Model

Concentration polarization (CP), is the gathering of more solute (in the case of concentrative) or watering of solute (in the case of dilutive) on the membrane surface in comparison to the bulk solution. This concentration disparity between the membrane surface and bulk solution diminishes the available osmotic pressure across the dense part of the membrane and limits the performance of the FO process [17,40,55,108]. Net permeate from the FO membrane depends heavily on the osmotic difference of concentrated DS and a diluted FS. Like RO membranes, FO membranes

consist of a thin dense salt rejecting layer facing one side and a thick porous support layer facing the other side.

As depicted in Figure 3-1, when the separation layer is facing the DS, there will be DECP on the DS side, CICP in the support layer, and CECP on the FS side. Water permeates from FS to DS and dilutes the DS concentration on the DS side, as shown in Figure 3-1. The solute in FS will accumulate both on the FS side and within the porous support layer. In the meantime, solutes diffuse from the bulk DS side through the active and porous support layer to the bulk FS side owing to the concentration gradient from the DS side. These water and reverse solute fluxes, including corresponding CP, are described by convection-diffusion equation [117] as

$$J_S = D\frac{dC(x)}{dx} - J_W C(x) \tag{4.3}$$

At steady state, the solute fluxes within the active and support layer are equal. Thus,

$$J_S = B\left(C_{DS,m} - C_{FS,m}\right) = D\frac{dC(x)}{dx} - J_W C(x) \tag{4.4}$$

with boundary conditions

$x = 0$, $C(x) = C_{DS,m}$

$x = \delta_D$, $C(x) = C_{DS,b}$, $D = D_D$

Solving Eq. 4.4 with the above boundary conditions gives the DS concentration at the active layer as

$$C_{DS,m} = C_{DS,b}\exp\left(\frac{-J_W}{k_{DS}}\right) + \frac{J_S}{J_W}\left(\exp\left(\frac{-J_W}{k_{DS}}\right) - 1\right) \tag{4.5}$$

Where $k_{DS} = \delta_{DS}/D_{DS}$, and k_{DS}, δ_{DS}, and D_{DS} are the mass transfer coefficient in [m/s], the thickness of the boundary layer in [m] and the solute diffusion coefficient at DS side in [m^2/s]. $C_{DS,b}$ is DS concentration at the bulk phase.

Similarly, the FS concentration at the active layer, $C_{FS,m}$ is derived from

$$J_S = B\left(C_{DS,m} - C_{FS,m}\right) = D\frac{dC(z)}{dz} - J_W C(z) \tag{4.6}$$

with boundary conditions

z = 0, C(z) = $C_{FS,p}$

z = ts, C(z) = $C_{FS,m}$, D = D_{diff}

z = -δ_F, C(z) = $C_{FS,b}$, D = D_F

Solving Eq. 4.6 with these boundary conditions gives the FS concentration at the active layer as

$$C_{FS,m} = C_{FS,b}\exp\left(J_W\left(\frac{S}{D_{diff}} + \frac{1}{k_{FS}}\right)\right) + \frac{J_S}{J_W}\left(\exp\left(J_W\left(\frac{S}{D_{diff}} + \frac{1}{k_{FS}}\right)\right) - 1\right) \tag{4.7}$$

Subtracting Eq. 4.7 from Eq. 4.5 and rearranging yields

$$C_{DS,m} - C_{FS,m} = \frac{C_{DS,b}\exp\left(\frac{-J_W}{k_{DS}}\right) - C_{FS,b}\exp\left[J_W\left(\frac{S}{D_{diff}} + \frac{1}{k_{FS}}\right)\right]}{1 + \frac{B}{J_W}\left\{\exp\left[J_W\left(\frac{S}{D_{diff}} + \frac{1}{k_{FS}}\right)\right] - \exp\left(\frac{-J_W}{k_{DS}}\right)\right\}} \tag{4.8}$$

Applying the Van't Hoff theory, i.e., the linear relationship between concentration and osmotic pressure, to Eq. 4.8 and substituting it into Eq. 4.1 yield

$$J_W = A\left\{\frac{\pi_{DS,b}\exp\left(\frac{-J_W}{k_D}\right) - \pi_{FS,b}\exp\left[J_W\left(\frac{S}{D_{diff}} + \frac{1}{k_F}\right)\right]}{1 + \frac{B}{J_W}\left\{\exp\left[J_W\left(\frac{S}{D_{diff}} + \frac{1}{k_F}\right)\right] - \exp\left(\frac{-J_W}{k_D}\right)\right\}} - \left(P_{DS} - P_{FS}\right)\right\} \tag{4.9}$$

Similarly, the solute transport can be expressed as

$$J_S = \frac{J_W + A\Delta P_{DS-FS}}{\frac{A}{B}\nu RT} \tag{4.10}$$

Where k_{FS} = δ_{FS}/D_{FS}, and k_{FS}, $\delta_{FS,}$ and D_{FS} are the mass transfer coefficient, the thickness of the boundary layer and solute diffusion coefficient at FS side,

respectively. D_{diff} is the solute diffusion coefficient at the porous support layer in [m^2/s], and t_s is the thickness of the support layer [m]. $C_{FS,p}$ and $C_{FS,b}$ are the feed concentration at the surface of the porous support layer and bulk phase, respectively.

The water and solute fluxes are often expressed in terms of intrinsic membrane properties like the structural parameter (S), solute permeability coefficient (B), and water permeability coefficient (A), as presented in Eq. 4.9 and Eq. 4.10.

The mass transfer coefficient (k) can be empirically expressed in terms of a dimensionless number called Sherwood number, (Sh). Sherwood number is a function of two other dimensionless number, Reynolds number (Re) and Schmidt (Sc) number. The detailed relation between mass transfer coefficient (k) and dimensionless number (Sh, Re, and Sc) is given as:

$$k_{DS} = \frac{D_{DS} Sh_{DS}}{d_o} \quad and \quad k_{FS} = \frac{D_{FS} Sh_{FS}}{d_i} \tag{4.11}$$

$$Sh_{DS} = \alpha_{DS} \mathrm{Re}_{DS}^{\ \beta} Sc_{DS}^{\ \gamma} \quad \text{and} \quad Sh_{FS} = \alpha_{FS} \mathrm{Re}_{FS}^{\ \beta} Sc_{FS}^{\ \gamma} \tag{4.12}$$

$$\mathrm{Re}_{DS} = \frac{d_{o\,fiber} u_{shell} \rho_{shell}}{\mu_{shell}} \text{ and } \mathrm{Re}_{FS} = \frac{d_{i\,fiber} u_{lumen} \rho_{lumen}}{\mu_{lumen}} \tag{4.13}$$

$$Sc_{DS} = \frac{\mu_{shell}}{\rho_{shell} D_{DS}} \text{ and } Sc_{FS} = \frac{\mu_{lumen}}{\rho_{lumen} D_{FS}} \tag{4.14}$$

$$\rho_{shell} = 994.7 + 0.76 C_{DS} \text{ and } \rho_{lumen} = 994.7 + 0.76 C_{FS} \tag{4.15}$$

Where d_o and d_i are the outer and inside diameter of the fiber in [m], α_{DS}, α_{FS}, β, and γ are constants in [-], μ_{shell} and μ_{lumen} are shell and tube side viscosity in [Pa.s], u_{shell} and u_{lumen} are shell and tube side velocity in [m/s], ρ_{shell} and ρ_{lumen} are shell and tube side density in [kg/m^3], respectively. The subscript DS and FS represent the draw and feed solution side. In this paper, β = 0.7845 and γ = 0.33 were taken from M. Shibuya et al. (2016) [53].

As reported in the literature [31,62,63,117–119], the solute permeability coefficient (B) was found to be constant above 35 kg/m^3 salt concentration. However, in this

work, B is observed to be a function of salt concentration at low salt concentration [32] and constant at higher salt concentration. The model equation of B as a function of salt concentration is given as

$$B = \begin{cases} mC_{DS,inlet} + b_0 & if\ C_{DS,inlet} < C^* \\ mC^* + b_0 & if\ C_{DS,inlet} \geq C^* \\ 0 & if\ C_{DS,inlet} = 0 \end{cases} \quad (4.16)$$

Where C* is the critical solution concentration (kg/m^3) whereby the linear relation of the solute permeability with respect to concentration changes to constant, m and b_0 are the slope in (m^6/(m^2 s kg)) and y-intercept in (m^3/(m^2 s)) of solute permeability coefficient (B), respectively.

Similarly, L. Xia et al. reported the structural parameter as a function of salt concentration [120]. To accommodate such variation in this work, the solute diffusivity at DS, FS, and porous support layer side of the membrane is expressed as a function of concentration [121]

$$D_{DS} \,/\, D_{FS} \,/\, D_{diff} = -462.93\left(\sqrt{C}\right)^3 + 973.7\left(\sqrt{C}\right)^2 - 641.13\left(\sqrt{C}\right) + 1604 \quad (4.17)$$

Where C is the average concentration in mol/L.

The concentration of FS in the porous support layer increases due to the rejection by the active layer of the membrane. The solute accumulation near the separation layer leads to CICP. This effect is quantified by solute resistivity, K as given in Eq. 3.7 [55,109].

Since the solute size is smaller than the support pore size and high turbulence near the support layer, the ECP in the flat sheet membrane's porous support layer was assumed to be negligible in most of the literature [5,17,24,55,62]. However, in the HF module case, the membrane is asymmetric and without a support layer. Therefore, the effect of ECP near the porous support layer at low fluid velocity conditions may not be negligible. It can be included as shown in appendix Eq. 4.7.

The effects of ECP and ICP on the net driving force is governed by membrane orientation, namely active layer facing DS (ALDS) or active layer facing FS (ALFS). In this chapter, ALDS orientation is used, as shown in Figure 3-1.

The SD model incorporating both ECP and ICP is shown in Eq. 4.9. As per the above discussion, the DECP will affect the osmotic pressure of DS by a factor $exp(-J_W/k_{DS})$, the CECP will affect the osmotic pressure of FS by a factor $exp(J_W/k_{FS})$, and the CICP will affect the osmotic pressure of FS by a factor $exp(J_W S/D_{diff})$ for ALDS orientation. The positive exponent on the FS side signifies the concentrative effect of ECP and ICP $(C_{FS,m} > C_{FS,b})$, and the negative exponent on the DS side signifies the dilutive effect of ECP $(C_{DS,m} < C_{DS,b})$ at the membrane surface [53].

4.1.4 Mass Balance for HF FO Module

In this work, the following equations were used to develop the mathematical model for the HF FO module. The solvent and solute balance for both the shell side (DS) and lumen side (FS) along the HF FO module is given by:

DS water balance $$\frac{dQ_{DS}}{dz} = n\pi d_i J_W \quad (4.18)$$

FS water balance $$\frac{dQ_{FS}}{dz} = -n\pi d_i J_W \quad (4.19)$$

DS solute balance $$\frac{dQ_{DS}C_{DS}}{dz} = -n\pi d_i J_S \quad (4.20)$$

FS solute balance $$\frac{dQ_{FS}C_{FS}}{dz} = n\pi d_i J_S \quad (4.21)$$

Boundary condition are: $$at\ z=0 \begin{cases} Q_{DS} = Q_{DS,inlet} \\ Q_{FS} = Q_{FS,inlet} \\ C_{DS} = C_{DS,inlet} \\ C_{FS} = C_{FS,inlet} \end{cases} and\ at\ z = L \begin{cases} Q_{DS} = Q_{DS,outlet} \\ Q_{FS} = Q_{FS,outlet} \\ C_{DS} = C_{DS,outlet} \\ C_{FS} = C_{FS,outlet} \end{cases}$$

where J_W and J_S are calculated from the above flux equations, i.e., Eq. 4.9 and Eq. 4.10, respectively. $C_{DS,outlet}$, $C_{DS,inlet}$, $C_{FS,outlet}$ and $C_{FS,inlet}$ are concentrations at outflow and inflow of DS and FS in [kg/m^3], respectively.

4.1.5 Momentum Balance Equation for HF FO Module

The Ergun equation is used to describe the pressure drop in a packed bed as a function of the viscous and kinetic terms. This equation is mainly used when the kinetic term has a significant effect on pressure loss [122]. In the HF FO module, since the fibers are expected to act as a packed bed with respect to the shell side, the shell side pressure drop was estimated using the Ergun equation [34,88,122] as follows.

$$\frac{dP_{shell}}{dz} = \frac{150\left(1-\varepsilon\right)^2 \mu_{shell} u_{shell}}{\varepsilon^3 \left(1.5 d_o\right)^2} + \frac{1.75\left(1-\varepsilon\right) \rho_{shell} u_{shell}^{\ 2}}{\varepsilon^3 \left(1.5 d_o\right)} \tag{4.22}$$

where P, z, and ε are pressure in [bar], axial direction coordinates in [m], and the porosity of the HF module in [-], respectively.

The applicability of the Ergun equation for pressure drop in the current module was verified by supplying distilled water on the shell side while closing the inlet and outlet of the lumen side. Based on these experimental results (refer to Table B. 2 and Figure B. 3 in the appendix), the Ergun equation was found to underestimate the pressure drop in the module. Thus, the constants 150 and 1.75 in viscous and kinetic terms of the Ergun equation were re-estimated from the FO experimental results.

The pressure drop in the HF lumen side is expressed by the Hagen-Poiseuille equation [34,53,88]

$$\frac{dP_{lumen}}{dz} = \frac{32 \mu_{lumen} u_{lumen}}{d_i^{\ 2}} \tag{4.23}$$

4.1.6 Tank Mass Balance Equations

A simple tank model is applied to replicate the continuous recirculation system. The flow out from the tank is connected to the inlet of the module, and the outlet from the module is recirculated back as inflow to the tank.

The mass and solute balances for DS and FS tanks are expressed by,

$$\frac{d\left(\rho_{DS,outlet}V_{DS}\right)}{dt} = \rho_{DS,outlet}Q_{DS,outlet} - \rho_{DS,inlet}Q_{DS,inlet} \quad (4.24)$$

$$\frac{d\left(\rho_{FS,outlet}V_{FS}\right)}{dt} = \rho_{FS,outlet}Q_{FS,outlet} - \rho_{FS,inlet}Q_{FS,inlet} \quad (4.25)$$

$$\frac{d(V_{DS}C_{DS})}{dt} = Q_{DS,outlet}C_{DS,outlet} - Q_{DS,inlet}C_{DS,inlet} \quad (4.26)$$

$$\frac{d(V_{FS}C_{FS})}{dt} = Q_{FS,outlet}C_{FS,outlet} - Q_{FS,inlet}C_{FS,inlet} \quad (4.27)$$

$$\rho_{DS} = 994.7 + 0.76C_{DS} \quad and \quad \rho_{FS} = 994.7 + 0.76C_{FS} \quad (4.28)$$

with initial conditions, at t = 0, $V_{DS} = V_{DS,initial}$ and $V_{FS} = V_{FS,initial}$

boundary condition: at z = 0, $Q_{DS} = Q_{DS,inlet}$, $Q_{FS} = Q_{FS,inlet}$, $C_{DS} = C_{DS,inlet}$ and $C_{FS} = C_{FS,inlet}$ and at z = L, $Q_{DS} = Q_{DS,outlet}$, $Q_{FS} = Q_{FS,outlet}$, $C_{DS} = C_{DS,outlet}$ and $C_{FS} = C_{FS,outlet}$

4.1.7 Method for Solving the Model Equations

The HF FO model was solved in MATLAB 2017b academic version (Mathworks, Natick, MA, USA) platform. The DS weight change and concentration of DS and FS tank data were used to estimate the membrane parameters. The flow chart for solving the HF FO model is shown in Figure 4-2. The calculations were initiated by entering initial conditions (e.g., initial DS and FS volume and concentration), fixed variables (e.g., membrane area, module and fiber size, and gas constant, etc.), and physical properties of the solution (e.g., diffusion coefficient, viscosity, density).

Membrane parameters estimated based on the $C_{DS,inlet}$ = 45 kg/m^3 are used to simulate and validate the $C_{DS,inlet}$ = 30 kg/m^3 experimental results.

4.1.8 Method for Membrane Parameter Estimation

The error function (Eq. 4.29), which is the error between experimental results and model outputs, was derived to estimate the membrane parameters. The parameters were found by minimizing the deviation between the experimental results and simulated values. In this chapter, the Genetic Algorithm (GA) optimization technique was used to minimize the deviation and evaluate the membrane transport parameters (A, B (C*, m, b_0) and S), mass transfer coefficient parameters (α_{DS}, and α_{FS}) and pressure drop equation coefficients (e_1 and e_2). The objective function, i.e., the error function, is shown below,

$$Error = \sum \left[\left| \frac{C_{DS,\exp} - C_{DS,\mathrm{mod}}}{C_{DS,\exp}} \right| + \left| \frac{C_{FS,\exp} - C_{FS,\mathrm{mod}}}{C_{FS,\exp}} \right| + \left| \frac{\Delta V_{\exp} - \Delta V_{\mathrm{mod}}}{\Delta V_{\exp}} \right| + \left| \frac{\Delta P_{\mathrm{D},\exp} - \Delta P_{\mathrm{Dout,mod}}}{\Delta P_{\mathrm{D},\exp}} \right| \right] \quad (4.29)$$

where C, V, and P denote concentration, volume, and pressure, and subscript exp and mod represent experimental result and model outputs, respectively. The relative absolute error is implemented to avoid the dominance of one error over the other one (for example, C_{DS} over C_{FS}). The lower and upper bound for the estimated membrane parameters were

$$1 \le C^* \le 75 \qquad 10^{-11} \le b_0 \le 10^{-6} \qquad 0.01 \le \alpha_{FS} \le 0.99$$
$$10^{-14} \le m \le 10^{-8} \qquad 4x10^{-5} \le S \le 2x10^{-3} \qquad 0.01 \le \alpha_{DS} \le 0.99$$

While solving the model equations in MATLAB, zero velocity in the FS was observed along the path of FS for some operating conditions. The possibility of getting zero velocity in the FS might be because of lower Q_{FS} or higher Q_{DS}. Thus, to avoid such a bottleneck during the GA optimization process, a penalty function was included, which set the error to a very high value whenever Q_{FS} reached zero anywhere along the length of the module. The method for estimating the model parameters is shown in Figure 4-2.

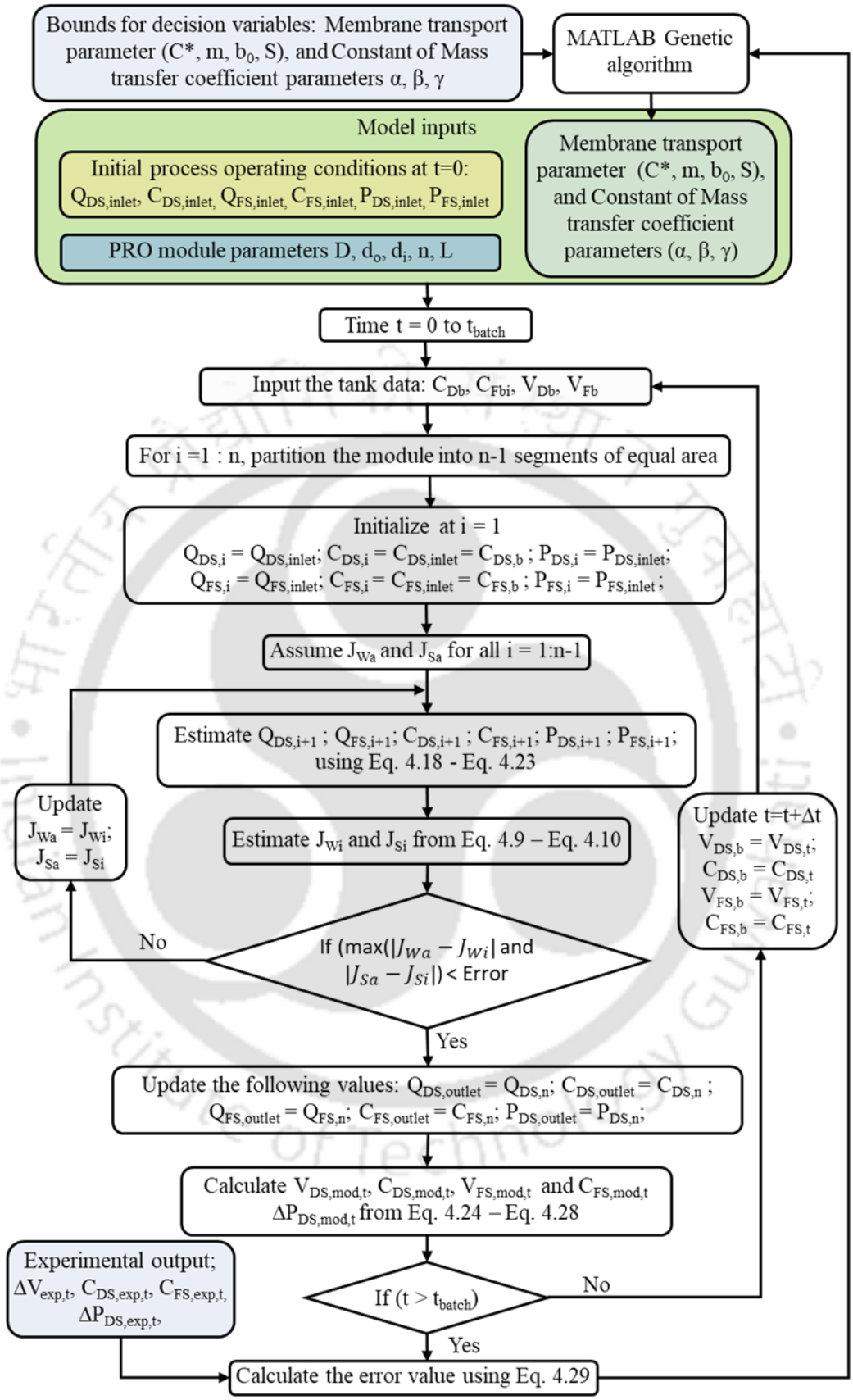

Figure 4-2. Flow chart for solving the batch HF FO process model equations and estimating the unknown parameters of the HF FO module

4.1.9 Formulation of an Optimization Problem for HF FO Module Configuration

The performance of any HF FO membrane for a given membrane area is a function of module dimensions and operating conditions such as flow rates and pressure drop on the DS and FS side. In this section, the effects of these parameters on the FO performance, net permeate flow, and power consumption will be investigated. The overall objective is to minimize the net power required by the FO process and maximize the FO flux. However, due to the pressure drop in the module, the net power required for the FO process will be increasing with an increase in the FO flux. Under these circumstances, the following objective function can be formulated,

1. Minimization of net power supplied to the FO process subject to the following constraint
   FO Module flux ≥ Target Flux
2. Minimization of net power consumption per unit FO water flux subject to the following constraint
   FO Module flux ≥ Target Flux

In this thesis, the second objective function was chosen for further study since the minimum global power consumed by FO can be calculated as

$$\min f = \frac{Pw_{inp}}{Q_P} \tag{4.30}$$

Where Q_P and Pw_{inp} are permeate flow rate (L/min) and input power consumed (watt), respectively, given by

$$Pw_{inp} = P_{DS,inlet}Q_{DS,inlet} + P_{FS,inlet}Q_{FS,inlet} \tag{4.31}$$

$$Q_P = Q_{DS,outlet} - Q_{DS,inlet} \tag{4.32}$$

The dimensions of the membrane were calculated based on the net membrane area, ID and OD of fiber, and porosity of the module. The net membrane surface area is given by,

$$A_M = n\pi d_i L \tag{4.33}$$

Where A_M, n, and L are membrane surface area, number of fiber, and length of the fiber, respectively. The porosity of the module is fixed to a constant value for any size of the module, given by the equation

$$\varepsilon = \frac{\text{Volume of module} - \text{Volume of hollow fibers}}{\text{Volume of module}} = \frac{D^2 - nd_o^2}{D^2} = \text{constant} \tag{4.34}$$

From the above equations, it is evident that only the length of the module has to be varied to fix the diameter of the module.

While solving the optimization problem, the optimizer is expected to give a different combination of module length, inlet flow rate, and pressure to the model. The combination of low flow rate and low pressure with larger module length may result in negative velocity and pressure along the module length, which might crash the model. Therefore, to avoid such scenarios during optimization, the following constraints are included in the optimization problem.

$$Q_{FS,outlet} > 0.5 \qquad P_{FS,outlet} > 0 \qquad P_{DS,outlet} > 0$$

The simulation results indicated that the objective function was always converging at the lowest power consumption value. However, the water flux was converging at the lower bound of the constraint. To avoid such a scenario, the objective function (Eq. 4.30) can be reformulated as follows:

$$\max f = \text{Cost}_P Q_P - \text{Cost}_{energy} Pw_{inp} \tag{4.35}$$

where Cost_p is the cost of permeate per unit volume of permeate ($/L) and Cost_{energy} is the cost of energy per kWh ($/kWh).

The costs of the input power and revenue from the FO process are required in Eq. 4.35. These depend on factors like region, market demand, etc. Removing these location-based cost factors in the objective function is a very important aspect to provide a globally optimal solution. Therefore, a multi-objective optimization problem is formulated as shown below:

$$\min f(1) = Pw_{inp} \tag{4.36}$$

$$\max f(2) = Q_p \tag{4.37}$$

The decision variables were the active module length in [m], DS and FS pressure in [bar], and DS and FS flow rate in [L/min]. The corresponding lower and upper bounds were

$$0.1 \le L \le 0.8 \qquad 0.1 \le P_{DS,inlet} \le 16 \qquad 0.5 \le Q_{DS,inlet} \le 10$$
$$0.1 \le P_{FS,inlet} \le 16 \qquad 0.5 \le Q_{FS,inlet} \le 10$$

4.2 Materials and Methods

The bench-scale FO experiments were conducted using the Toyobo HF FO module. The FO membrane, supplied by Toyobo Co. Ltd., Japan, is made of cellulose triacetate. The specification of this module is given in Table 4-1. The FS and DS were recirculated using a 300 GPD heavy-duty booster pump (supplied by the Hi-Tech company, India). These pumps were individually controlled using a pump speed controller. The solutions flow rates were measured by PP helical flow meter (supplied by ASMA industrial corporation, India). The flow rate, pressure, temperature, and total volume passed through the flow meter were displayed and recorded by using a digital flow indicator cum totalizer (supplied by ASMA industrial corporation, India). The inlet and outlet pressure of the module is measured by ASCORP digital pressure gauge (supplied by ASMA industrial corporation, India). The temperature of both solutions was kept at 25 ± 0.5 °C using a circulating water bath (ANM Industries, India). The permeate volume, which is equivalent to DS weight change, was measured by the data logging weighing system (Weighing solutions and instrumentation, India). The real-time FS and DS concentrations were measured by two Hanna conductivities meters (HI5321 Research grade EC/TDS/resistivity/salinity professional benchtop meter, HANNA Instruments, USA). The FS is continuously mixed using a magnetic stirrer (Tarsons 1515 watts Ceramic Spinot Digital Magnetic Stirrer Hot Plate, 6090). The DS weighing change and the conductivities of both FS and DS were recorded in the

personal computer. RO water with a conductivity of less than 25 µS/cm was used to prepare FS and DS. The experiments were conducted using 10 L of FS and 4 L of 45 and 30 kg/m^3 NaCl as DS.

4.2.1 Toyobo HF FO Module Specifications

The bench-scale FO experiments were conducted using the Toyobo HF FO module. The FO membrane, supplied by Toyobo Co. Ltd., Japan, is made of cellulose triacetate. The specification of this module is given in Table 4-1.

Table 4-1. Toyobo HF module specification

Parameter	Symbol	Unit	Value
Model		-	HPC3205
Membrane area	A_M	m^2	30.5
Material of vessel	PVC	-	Poly Vinyl Chloride
Module type	HF	-	Hollow fiber
Module diameter	D	m	7.57 x 10^{-2}
Module length	l	m	0.74
Module active length	L	m	0.63
Number of hollow fiber	n	-	99 x 10^3
Fiber outer diameter	d_0	m	175 x 10^{-6}
Fiber inside diameter	d_i	m	85 x 10^{-6}
Wound		-	Not wounded
Membrane material		-	Cellulose triacetate
Shell side operating pressure	P_{DS}	Pa	< 4.9 x 10^5
Tube side operating pressure	P_{FS}	Pa	< 2.0 x 10^5
Temperature	T	°C	5 - 40
pH			3 - 8
Residual Chlorine		mg/L	≤ 1

4.2.2 Experimental Setup

The schematic diagram of the experimental set-up is shown in Figure 4-3. The HF FO experimental setup consists of the following subcomponents: (i) HF FO membranes module (supplied by Toyobo Co. Ltd, Japan), (ii) solution tanks (supplied by Zenith India), and (iii) 300 GPD heavy-duty booster pump (supplied by the Hi-Tech company, India). For experimental data collection, the following instruments are installed: (i) four number of data acquisition system (supplied by ASMA industrial corporation, India) to display and record flow rate, pressure, temperature, and total volume of the DS and FS inlet and outlet, (ii) weighing balance with data logging feature (supplied by Weighing solutions and instrumentation, India) to measure change in DS and FS weight every sec, (iii) ASCORP digital pressure gauge (supplied by ASMA industrial corporation, India) to measure the inlet and outlet hydraulic pressure of the module, and (iv) Hanna conductivities meters (HI5321 Research grade EC/TDS/resistivity/salinity professional benchtop meter, HANNA Instruments, USA) to measure the conductivity of the DS and FS solution. The flow meter and pressure gauges were positioned on both sides of the module to measure the inlet and outlet flow rates and hydraulic pressures, as shown in Figure 4-3.

The temperature of both solutions was kept at 25 ± 0.5 °C using a circulating water bath (ANM Industries, India). The DS weight change was measured by the data logging weighing system (Weighing solutions and instrumentation, India). The real-time FS and DS concentrations were measured by Hanna conductivities meters (HI5321 Research grade EC/TDS/ resistivity/salinity professional benchtop meter, HANNA Instruments, USA). The FS was continuously mixed using a magnetic stirrer (Tarsons 1515 watts Ceramic Spinot Digital Magnetic Stirrer Hot Plate, 6090). The DS weighing change and the conductivities of both FS and DS were recorded in the personal computer. RO water was used to prepare both FS and DS. The FO experiments were conducted using 10 L of FS at $C_{FS,inlet}$ = 0.34 kg/m^3, and 4 L of DS at $C_{DS,inlet}$ = 45 kg/m^3 for experimentation and $C_{DS,inlet}$ = 30 kg/m^3 for validation. The FS and DS were passed through the lumens and shell side of the HF module,

respectively. The accuracy of the measuring apparatus is reported in Table B. 1 (refer to appendix).

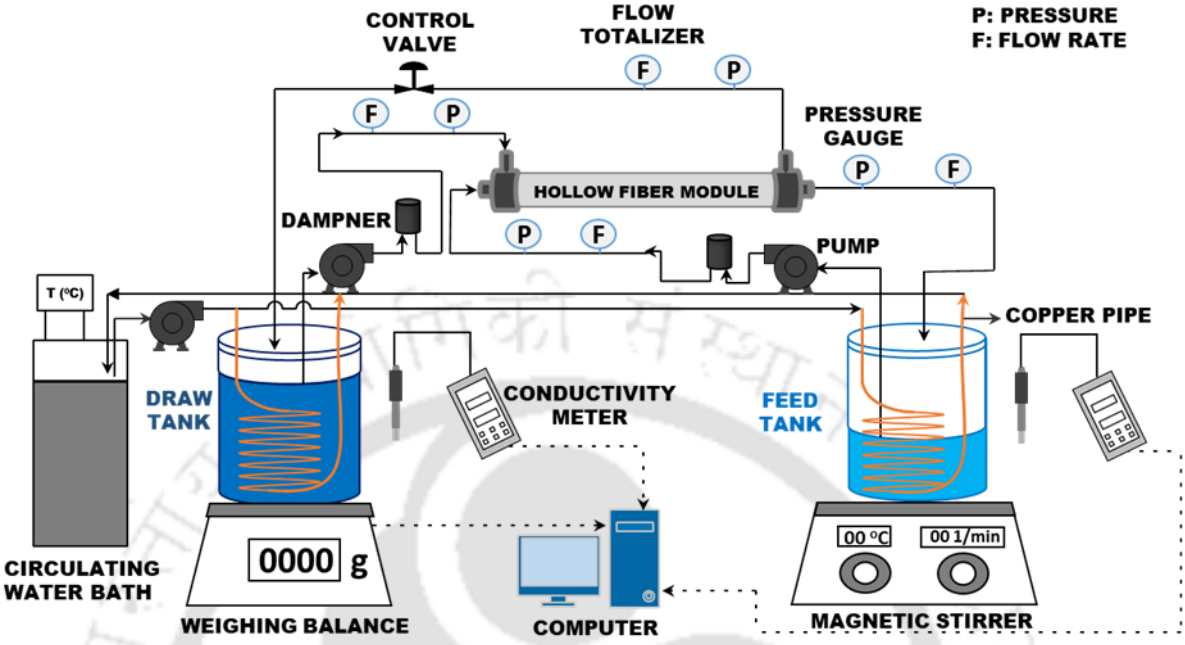

Figure 4-3. The experimental setup for forward osmosis process

For redundancy, the weight and concentration changes in both tanks are also recorded in the data acquisition system. Since the high accuracy of the dynamic experimental measurements is essential for analyzing the batch HF FO experimental results, the measuring devices used in this experimental setup are accurate enough to capture all the measurements within ± 1%. In this study, all the FO experiments are performed in co-current mode by circulating both DS and FS in the same direction through the axial flow HF FO module.

4.2.3 Design of Experiment

Before each experiment, deionized water was flushed through the shell, lumens, and dampeners along with FS and DS lines. The solute transfer from DS to FS and solvent from FS to DS resulted in a dynamic change of weight and concentration in the tanks. This dynamic change was recorded every 5 seconds until the end of the experiment. The conductivity of FS and DS and the weight of DS were recorded on the computer. The recorded conductivity data was converted to concentration using the

conductivity-concentration calibration graph. Further, the inlet and outlet flow rate, pressure, total volume passed, and the temperature of the solution was recorded by the flow totalizer. Dampeners were placed after the pumps to reduce the fluctuation in flow rate and pressure. The outlet streams of the HF module were connected back to their respective FS and DS tanks. Moreover, for proper FS mixing, a magnetic stirrer has been used only on the FS side, as shown in Figure 4-3, since the DS is occupied by weighing balance and due to the reasonable mixing of DS tank as a result of the higher DS flow rate from the module. All the experimental results reported are the average of three experimental data.

4.3 Results and Discussion

4.3.1 Characterization of the HF FO Module

The experimental conditions for conducting the actual FO experiment are shown in Table 4-2. The recirculation mode of the FO experiment was carried out at multiple combinations of DS-FS inlet concentrations. As depicted in Figure 4-4, the total number of experimental values to be fitted at a time were three, namely, net volume change, C_{DS}, and C_{FS}. Since this approach gives the advantage of using experimental results at multiple data points, the accuracy of the parameters is expected to be superior. The model parameters were predicted by minimizing the error between the experimental results and model outputs at a DS concentration of 45 kg/m^3. Then, the estimated parameters were validated at a DS concentration of 30 kg/m^{3,} as shown in Figure 4-4 (c). The lower and upper bound for the estimated membrane parameters were

$$1 \le C^* \le 75 \qquad 10^{-11} \le b_0 \le 10^{-6} \qquad 0.01 \le \alpha_{FS} \le 0.99$$
$$10^{-14} \le m \le 10^{-8} \qquad 4x10^{-5} \le S \le 2x10^{-3} \qquad 0.01 \le \alpha_{DS} \le 0.99$$

Before estimating these parameters, the water permeability value (A) and the Ergun equation constants (e_1 and e_2) were set as the experimental results obtained by passing distilled water, as explained below.

Table 4-2. The experimental condition for HF membrane in FO mode

	units	Shell side	Tube side
Solution type	-	Draw solution	Feed solution
Volume of solution	L	4.2	10
Concentration	kg/m^3	45 and 30	< 0.025
Flow rate	L/min	1.7	2.7
Pressure	bar	1.3	1.2
Temperature of solution	°C	25	25

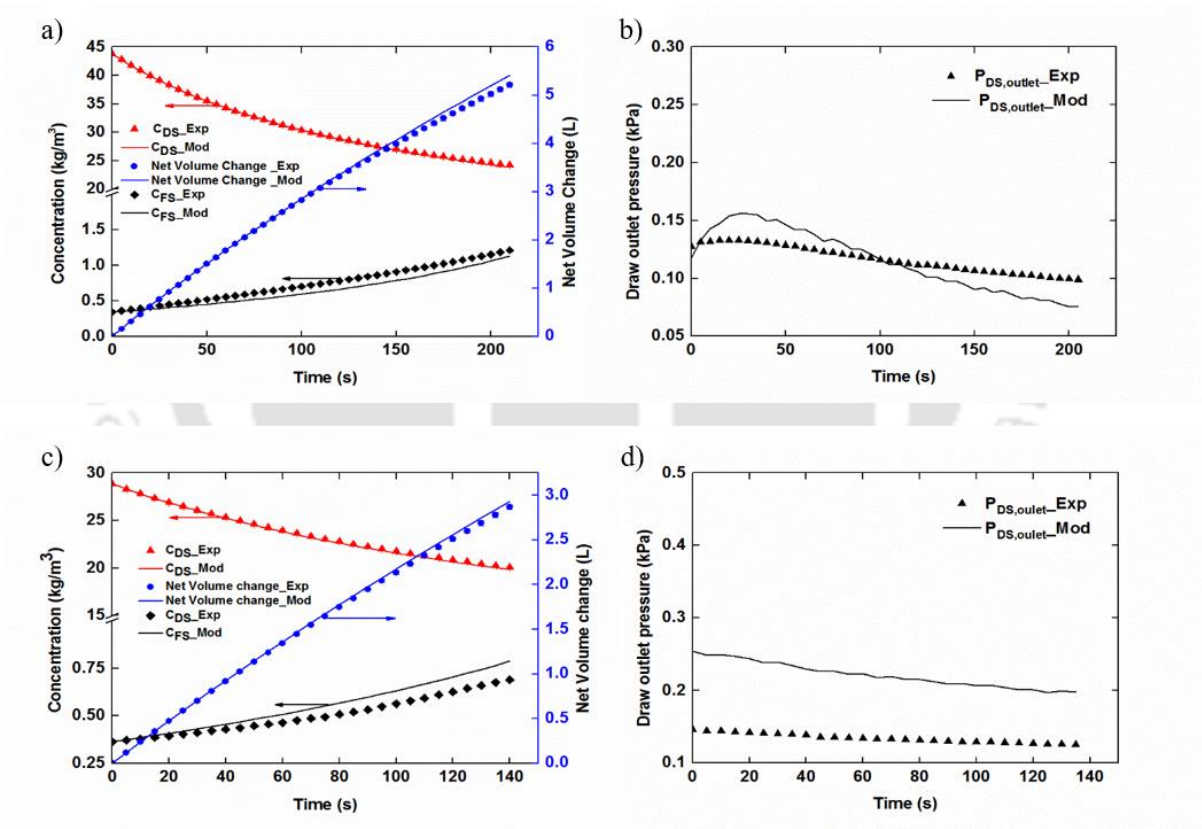

Figure 4-4. The experimental performance of Toyobo HF FO module for NaCl – water system and model prediction: (a) and (c) C_{DS}, C_{FS} and net volume change comparison for ($C_{DS,inlet}$ = 45 kg/m^3, $C_{FS,inlet}$ = 0.34 kg/m^3), and ($C_{DS,inlet}$ = 30 kg/m^3, $C_{FS,inlet}$ = 0.34 kg/m^3), respectively. (b) and (d) Draw outlet pressure comparison for ($C_{DS,inlet}$ = 45 kg/m^3, $C_{FS,inlet}$ = 0.34 kg/m^3), and ($C_{DS,inlet}$ = 30 kg/m^3, $C_{FS,inlet}$ = 0.34 kg/m^3) Note: $V_{DS,inlet}$ = 4.2 L, $V_{FS,inlet}$ = 10 L and T = 25 ± 0.5 °C.

The estimation of water permeability was performed by passing distilled water through the pre-conditioned HF membrane at different pressures (10, 15, 20, 25, and 30 Psi). The corresponding permeate flux was calculated based on the permeated volume collected. Unlike the flat sheet membrane, which uses RO mode for estimation of water permeability, here RO model was used. The axial flow RO model was built based on A. Chatterjee et al. [33]. The RO model takes care of the pressure variation along the HF module length. To estimate the water permeability, the model uses error minimization between the RO model output and experimental results. The comparison between the RO model and the experimental result is shown in Figure B. 1 (refer to appendix). The water permeability was estimated to be 1.1081 × 10^{-12} $m^3/(m^2\ s\ Pa)$.

Similarly, the estimated Ergun equation constants values are also comparable with the one obtained in the modified Ergun equations. The constants 150 and 1.75 in viscous and kinetic term of the Ergun equation were re-estimated for the HF module using the following equation,

$$\frac{dP_{shell}}{dz} = \frac{e_1\left(1-\varepsilon\right)^2 \mu_{shell} u_{shell}}{\varepsilon^3 \left(1.5 d_o\right)^2} + \frac{e_2\left(1-\varepsilon\right) \rho_{shell} u_{shell}^{\ 2}}{\varepsilon^3 \left(1.5 d_o\right)} \tag{4.38}$$

where e_1 and e_2 are the re-estimated constants for the viscous and kinetic terms of the modified Ergun equation.

Distilled water from a tank was supplied to the shell side, and the outlet flow was recirculated back to the tank. The lumen side inlet and outlet flow rate were closed for the entire run of the experiment. The distilled water tank was kept on a weighing balance. The steady-state of the process was confirmed by zero change in the weighing balance. The inlet and outlet pressure at different flow rates were measured once a steady-state condition was achieved. The Ergun constants were determined by minimizing Eq. 4.39

$$Error = \left|\Delta P_{Exp} - \Delta P_{Modified\ Ergun\ Eq.}\right| \tag{4.39}$$

The viscous and kinetic term constants were found to be 200.8 and 279.1, respectively (refer to Table B. 2 and Figure B. 3 in the appendix).

After minimizing the error function (Eq. 4.29) using the genetic algorithm, the estimated parameters were found to be C* = 20.33 kg/m^3, m = 3.172 x 10^{-11} m^4/(s kg), b_0 = 0.837 x 10^{-8} m^3/(m^2 s), S = 498.2 µm, α_{DS} = 0.173, and α_{FS} = 0.13. The solute permeability coefficient was found to be directly proportional to $C_{DS,inlet}$ till some concentration and found to be constant afterward as given in Eq. 4.16 and shown in Figure B. 2 (refer appendix) [32].

Moreover, the estimated intrinsic membrane parameters of this study were compared with the other Toyobo HF module as shown in Table 4-3. The membrane transport parameters (A, B, and S) estimated by Shibuya et al., 2016 were based on both RO and FO experimental data using the HF FO mini-module containing 720 fibers. In their approach, the effects of pressure drop, DS dilution, and FS concentration were overlooked. However, these effects cannot be neglected for a larger hollow fiber module with significant pressure drop and high-water flux. Later Tanaka et al., 2018 developed a model incorporating mass and momentum balance along the model length. However, Tanaka et al., have taken the values of A, B, and S (for module 1 shown in Table 4-3) from Shibuya et al., and estimated the other parameter using the FO experimental data.

Nevertheless, in this work, unlike Shibuya et al., 2016, the effects of pressure drop, DS dilution, and FS concentration were incorporated into the model. Besides, the HF FO module experimental data was used to estimate all the membrane transport parameters. The pure water permeability (A) was estimated using RO pure water permeability experimental data and the remaining membrane transport parameters (B and S) and coefficient of mass transfer correlation (α_{FS}, α_{DS}) were estimated using FO experiments.

Table 4-3. Comparison of the literature reported intrinsic membrane parameter of Toyobo HF

Literature	Water permeability coefficient, AA x 10^{12} $m^3/(m^2\ s\ Pa)$	Solute permeability coefficient, B x 10^9 $m^3/(m^2\ s)$ (Refer Figure B. 2)	Structural parameter, S µm
This study	1.108	9.01 for $C_{DS,inlet} \geq 20.33$ kg/m^3 $3.172x10^{-11}$ x $C_{DS,inlet}$ + $0.837x10^{-8}$ for $C_{DS,inlet} < 20.33$ kg/m^3	498
[53]	0.75	9.72	1024
Tanaka et al., with module 1 [52]	0.75	9.72	1024
Tanaka et al., with module 2 [52]	1.67	20	912

Note: Module 1 and 2 differ one another in their technical specification

Furthermore, the previous studies mentioned above ignored the effect of ECP on the FS side. In doing so, the effect of ECP was reflected in the parameter expressing the ICP, i.e., 'S'. However, in this study, the effect of ECP and ICP are separated and expressed with the respective parameters ('S' and mass transfer coefficient). This segregation of ECP from ICP might result in a lower S value.

The quantified errors between the model outputs and experimental results for the net volume change, $C_{DS,}$ and C_{FS} in both parameter estimation and validation are shown in Table 4-4. The C_{FS} deviation could be due to the instrumental error at a very small concentration measurement. In addition, the outlet DS pressure from the experiment was compared with the corresponding model output, as shown in Figure 4-4 (b) and (d). In these figures, as the experimental duration increases, there is a

slight drop in draw outlet pressure in both experiments (0.29 bar for C_{DS} = 45 kg/m^3 and 0.21 bar for C_{DS} = 30 kg/m^3). However, in the model calibration case (C_{DS} = 45 kg/m^3), the model was able to predict the draw outlet pressure within ± 0.5 bar, whereas, in the model validation case (C_{DS} = 30 kg/m^3), it was always over-predicted with a maximum deviation of 1 bar. The error observed in the draw outlet pressure might be the limitation of the model developed in this study. Further, as it can be observed in Figure 4-4, the experimental duration was short due to the large HF FO module size and less DS and FS volume. Thus, to avoid experimental error related to measurements and short run time, all the experimental results reported in this study were taken as the average of three experimental data.

Table 4-4. The average error in C_{FS}, C_{DS}, and net volume change between model output and experimental results for $C_{DS,inlet}$ 45 and 30 kg/m^3

$C_{DS,inlet}$	Error in (%)		
(kg/m^3)	C_{FS}	C_{DS}	Net Volume Change
45	11.58	0.37	2.04
30	9.16	0.65	1.36

Note:

$$\text{Error in } C_{FS}(\%) = \frac{100}{n}\sum_{i=1}^{n}\left|\left(\frac{C_{FS,\text{exp}} - C_{FS,\text{mod}}}{C_{FS,\text{exp}}}\right)_i\right|$$

$$C_{DS}(\%) = \frac{100}{n}\sum_{i=1}^{n}\left|\left(\frac{C_{DS,\text{exp}} - C_{DS,\text{mod}}}{C_{DS,\text{exp}}}\right)_i\right|$$

$$\text{Net volume change }(\%) = \frac{100}{n}\sum_{i=1}^{n}\left|\left(\frac{\text{Net volume change}_{\text{exp}} - \text{Net volume change}_{\text{mod}}}{\text{Net volume change}_{\text{exp}}}\right)_i\right|$$

4.3.2 Simulation Studies on the HF FO Module

The model simulation studies are the preliminary step required to formulate an

optimization problem. The FO simulation studies were performed by (i) fixing Q_{FS} while varying design parameter (module length) and operating parameters (Q_{DS}, $P_{DS,}$ and P_{FS}), and (ii) fixing the design parameter while varying the operating parameters (Q_{DS}, Q_{FS}, $P_{DS,}$ and P_{FS}). The membrane area and porosity of the HF module were kept constant during these simulations, and the corresponding changes were made on the number of fibers and shell diameter. The performance of the HF FO module could be assessed by calculating the key parameters such as the net permeate produced by the module, the net power consumed by FS and DS pumps, and the energy consumed by the pumps per unit permeate volume produced by the module, also referred as specific energy consumption (SEC).

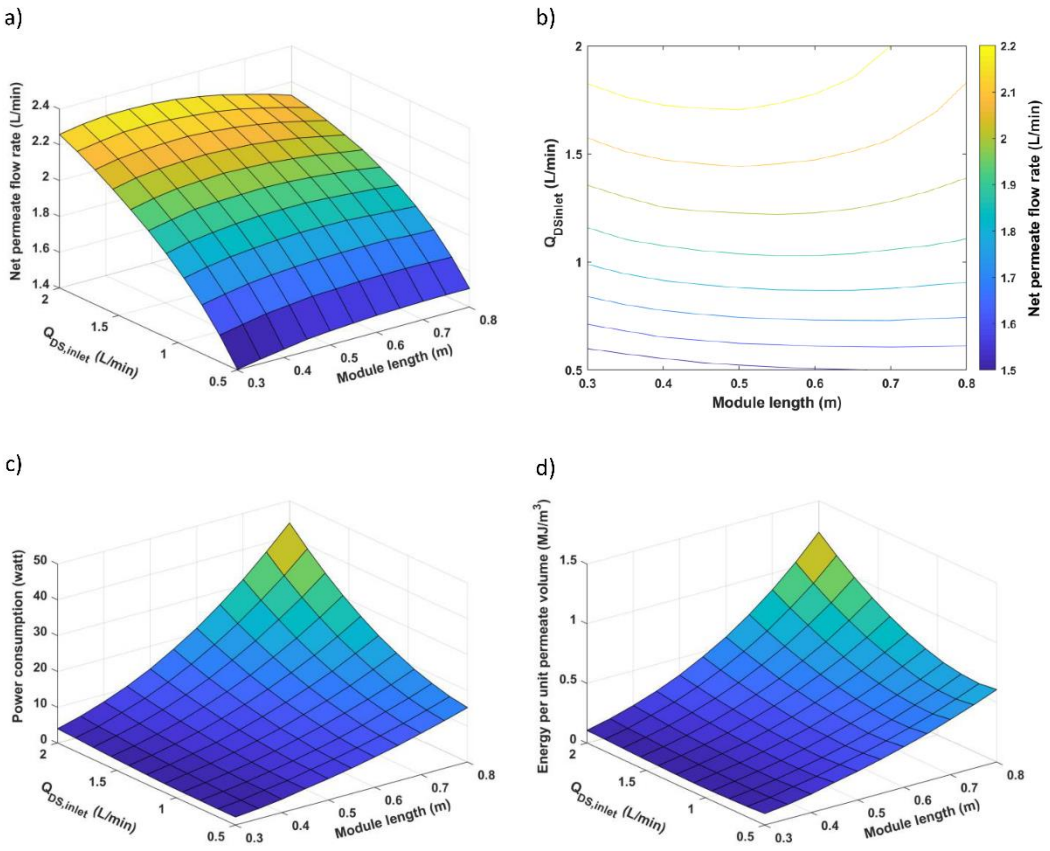

Figure 4-5. Simulation of the HF FO module performance in terms of net permeate flow rate (a and b (Contour plot)), power consumption (c) and energy per unit permeate volume (d) with respect to $Q_{DS,inlet}$ and module length. Note: $C_{DS,inlet}$ = 45 kg/m^3, $C_{FS,inlet}$ = 0.34 kg/m^3 and $V_{DS,inlet}$ = 4.2 L, $V_{FS,inlet}$ = 10 L and T = 25 ± 0.5 °C

The simulation results for the key parameters with respect to $Q_{DS,\ inlet}$ and module length are shown in Figure 4-5 (a), (c) and (d). These simulations were performed by varying the $Q_{DS,inlet}$ (from 0.5 to 2 L/min, typical operating condition as per the Toyobo manual) and module length (from 0.3 to 0.8 m, to provide sufficient length and be close to the actual length, respectively) along with $C_{DS,inlet}$ = 50 kg/m^3, $C_{FS,inlet}$ = 0.01 kg/m^3.

To maintain a sufficient FS flow rate inside the lumen, $Q_{FS,inlet}$ was kept at 3 L/min. Moreover, since the FO process operates at zero back pressure in the shell and lumen side, the inlet pressures, $P_{DS,\ inlet}$, and $P_{FS,\ inlet}$ were estimated based on the Ergun and Hagen-Poiseulle equation. Each run at different inlet conditions was made to converge at the minimum $P_{DS,inlet}$ and $P_{FS,inlet}$.

The net permeate flow rate for various module lengths and $Q_{DS,inlet}$ with the corresponding contour plot is shown in Figure 4-5 (a) and (b). It was observed that the net permeate flow rate was increasing with the increase in the $Q_{DS,inlet}$. This is an expected trend for any given FO module with a fixed length, where the increase in the $Q_{DS,inlet}$ reduces the ECP effect. As the $Q_{DS,inlet}$ increased further, the permeate flow rate reached a maximum value and then decreased with an increase in module length. The decrease in permeate flow rate was due to the high DS inlet pressure requirement. For example, at higher $Q_{DS,\ inlet}$ (>1.5 L/min) and longer module length (> 0.7 m), the estimated $P_{DS,inlet}$ was 20 bar. This high $P_{DS,inlet}$ reduced the net driving force available for the water flux. From the Ergun equation, both the length and $Q_{DS,inlet}$ played a major role in determining the $P_{DS,inlet}$. The other important contributor to the large pressure drop in the module was its high packing density. As inferred from the Ergun equation, even a small increase in porosity significantly decreases the pressure drop in the module. However, at the lowest module length (< 0.4 m) and minimum flow rate (< 0.65 L/min), the required $P_{DS,inlet}$ was very small, less than the $P_{FS,\ inlet}$ and resulted in pressure-assisted osmosis, which favors the improvement of J_W.

The power consumption with respect to $Q_{DS,inlet}$ and module length is shown in Figure 4-5(c). The increment in power consumption was due to the increase in

$Q_{DS,inlet}$ and pressure drop. In accordance with the Ergun equation, a nonlinear increase of power consumption was observed for higher $Q_{DS,inlet}$ and larger module length. For the same membrane area, it should be noted that the decrease in the module length will increase the membrane area per unit length of the membrane. This will lead to a large permeation and a sudden increase in the shell side DS flow rate.

A similar trend was also followed by the SEC profile as presented in Figure 4-5 (d). The minimum SEC was obtained when both $Q_{DS,inlet}$ and module length are minimum, whereas the maximum SEC was obtained when both $Q_{DS,inlet}$ and module length are maximum. On the other hand, the maximum net permeate flow rate was observed at higher $Q_{DS,inlet}$ and larger module length (Figure 4-5 (a)). This implied that the optimal points of the SEC and net permeate flow rate are contradicting each other.

Further, it was also necessary to investigate the effect of $Q_{FS,inlet}$ on the FO key parameters mentioned previously. This was carried out by fixing the module length where the SEC was minimum and by varying both $Q_{DS,inlet}$ and $Q_{FS,inlet}$.

Initially, the permeate flow rate was simulated for the condition $Q_{DS,inlet}$ = 0.5 to 2 L/min, $Q_{FS,inlet}$ = 3 to 5 L/min, $C_{DS,inlet}$ = 50 kg/m^3, $C_{FS,inlet}$ = 0.01 kg/m^3 and module length = 0.3 m. The results of the permeate flow rate simulation with the corresponding contour plot are depicted in Figure 4-6 (a) and (b). For a given $Q_{DS,inlet}$, an insignificant increment in the net permeate flow rate was observed with the increase in $Q_{FS,inlet}$. The contour plot in Figure 4-5 (b) revealed that the ratio of permeate flow rate to $Q_{DS,inlet}$ was declining, as $Q_{DS,inlet}$ increased from 0.5 to 2 L/min. For example, an increment of ~ 0.13 L/min (from 0.6 to 0.73 L/min) was required at lower $Q_{DS,inlet}$ to increase the net permeate flow rate by 0.1 L/min (from 1.5 to 1.6 L/min). However, at higher $Q_{DS,inlet}$, an increment of 0.27 L/min (from 1.58 to 1.85 L/min) resulted in the same 0.1 L/min rise (from 2.1 to 2.2 L/min) in the net permeate flow rate.

Following this, the power consumption was also simulated for the above conditions and the result is shown in Figure 4-6 (c). As expected from the Ergun and Hagen-

Poiseulle equation, the required $P_{DS,inlet}$ and $P_{FS,inlet}$ increased non-linearly and linearly with respect to $Q_{DS,inlet}$ and $Q_{FS,inlet}$, respectively.

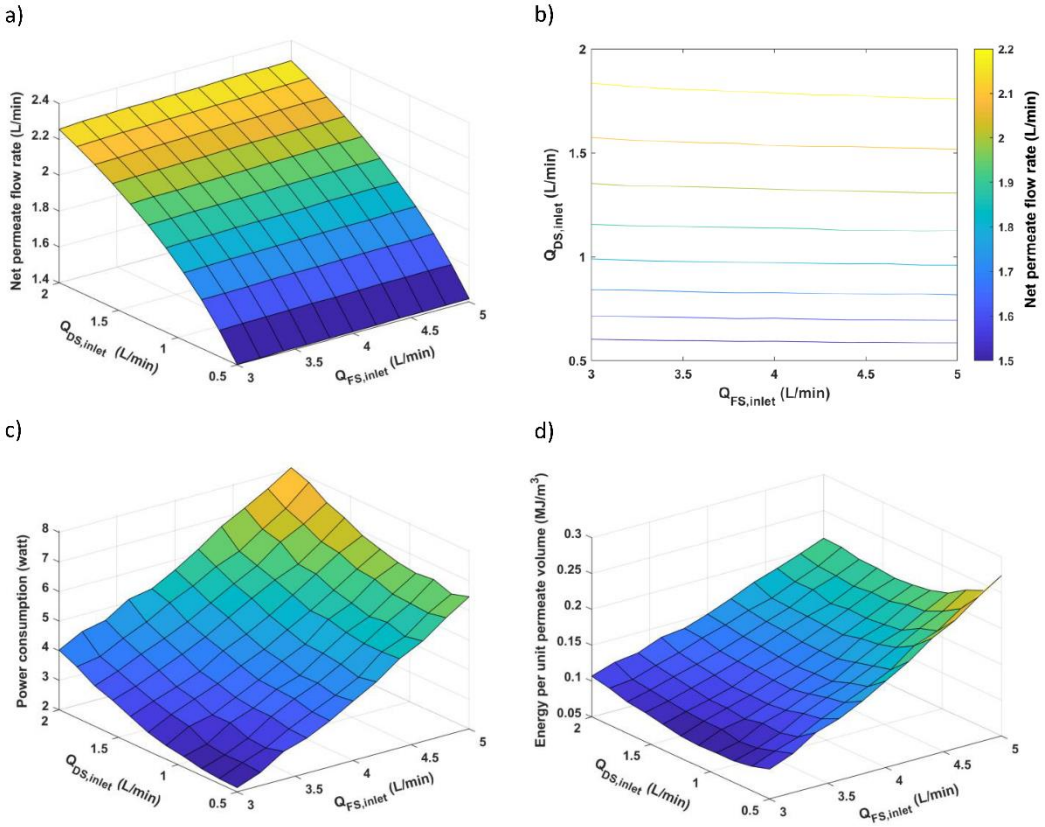

Figure 4-6. Simulation of the HF FO module performance in terms of net permeate flow rate (a and b (Contour plot)), power consumption (c) and energy per unit permeate volume (d) with respect to $Q_{DS,inlet}$ and $Q_{FS,inlet}$. Note: $C_{DS,inlet}$ = 45 kg/m^3, $C_{FS,inlet}$ = 0.34 kg/m^3 and $V_{DS,inlet}$ = 4.2 L, $V_{FS,inlet}$ = 10 L and T = 25 ± 0.5 °C.

Eventually, while increasing $Q_{DS,inlet}$ from 0.5 to 2 L/min, the SEC initially decreased until it reaches 1 L/min and then increased afterward, as shown in Figure 4-6 (d). The SEC follows a different trend compared to the power consumption, which was not observed in the previous case (Figure 4-5 (c) and (d)). The observed curvature can be attributed to the fact that the permeate flow rate is low at low $Q_{DS,inlet}$ (Qp << Power; Power/Qp is high) and the power consumption is large at high $Q_{DS,inlet}$ (Power >> Qp; Power/Qp is high). Hence, the optimum trade-off between these two parameters was observed at the minimum of the curvature.

The key points from the simulation study that demands for module optimization are:

(i) The $Q_{DS,inlet}$ has a minimum threshold value below which the considered module underperform due to concentration polarization effects. The upper $Q_{DS,inlet}$ limit depends on the manufacturer's decision on SEC expenditure.

(ii) The $Q_{FS,inlet}$ has a maximum threshold limit beyond which further increase will not result in significant improvement in the permeate flow rate. However, fixing a lower limit on the same can help in cost reduction.

(iii) The length of the module affects the pressure drop in both the shell and lumen sides, and hence should be kept small.

(iv) The inlet pressure for both DS and FS is generally the function of the inlet flow rate and module length. Thus, the only criteria for the optimization will be to maintain the inlet pressure at a minimum value.

The above key points revealed that there is a wide range of module design and operating conditions to conduct the FO operations. In addition, the simulation study explained the interconnections between these variables and their effect on permeate flow rate and corresponding power consumption. Overall, it can be seen that the power consumption for the FO process follows a contradicting and non-linear relation with the permeate flow rate. Thus, it requires a well-defined cost and profit objective function to find the optimum operating condition for a given HF FO module of a specific membrane area. The optimization of the operating conditions was further investigated by using multi-objective optimization with respect to the decision variables $P_{DS,inlet}$, $P_{FS,inlet}$, $Q_{DS,inlet}$, $Q_{FS,inlet,}$ and the module length.

4.3.3 Optimization Studies on the HF FO Module

The trade-off between the net permeate flow rate and corresponding power consumption for the FO membrane was analyzed based on the decision variables such as module length, $Q_{FS,inlet}$, $Q_{DS,inlet}$, $P_{FS,inlet}$, and $P_{DS,inlet}$. The conflicting nature of the two FO objectives: high net permeate flow rate and low power consumption, demand multi-objective analysis. Thus, a multi-objective optimization (MOO) problem was formulated with the objectives illustrated by Eq. 4.36 and 4.37.

The optimization study was carried out at C_{DS} = 50 kg/m^3 and C_{FS} = 0.01 kg/m^3. In the actual FO plant, the available C_{DS} and C_{FS} should be used for the MOO study. The decision variables for the MOO are module length in [m], P_{DS} and P_{FS} in [bar], and Q_{DS} and Q_{FS} in [L/min]. The corresponding lower and upper bounds were

$$0.1 \le L \le 0.8 \qquad 0.1 \le P_{DS,inlet} \le 5 \qquad 0.5 \le Q_{DS,inlet} \le 5$$
$$0.1 \le P_{FS,inlet} \le 5 \qquad 0.5 \le Q_{FS,inlet} \le 5$$

The above values should be close to the operating range prescribed by the HF FO manufacturer. The MOO decision variables were plotted against the permeate flow rate and power consumption, as shown in Figure 4-7 and Figure 4-8, respectively. The Pareto front between the permeate flow rate and power consumption followed an exponential curve as depicted in Figure 4-7 (a). The Pareto set provided a high permeate flow rate at the cost of large power consumption, which confirms the contradicting nature of maximizing the permeate flow rate and minimizing the power consumption. In Figure 4-7 (b), the maximum permeate flow rate was obtained at the shorter module length. The module length obtained from the Pareto was in the range of 0.3 - 0.5 m, which is less than the actual size (0.63 m). The module length at the lowest permeate flow rate was larger and continuously declined as the permeate flow rate increased. However, the effect of module length on the performance indicators ceased at 0.3 m, as shown in Figure 4-7 (b) and Figure 4-8 (a). The permeate flow rate and the power consumption were increasing without a further decrease in the module length. This might be due to the influence of the other decision variables such as FS and DS flow rate and pressure.

The FS and DS flow rate distribution was also plotted against the permeate flow rate and power consumption, as shown in Figure 4-7 (c) and Figure 4-8 (b). The minimum FS flow rate (1.5 L/min) was higher than the minimum DS flow rate (0.5 L/min) due to the constraint $Q_{FS,outlet}$ > 0.5 L/min, that guarantees a complete utilization of the membrane area. The DS flow rate was increasing steadily with the permeate flow rate (starting with 0.5 L/min), indicating the importance of DS flow rate as the driving force. Also, the DS flow rate in each of the Pareto points signifies the trade-off between the ECP and power consumption. The FS flow rate grows slowly with

respect to the permeate flow rate, up to 1.5 L/min, followed by a sudden increase towards the end.

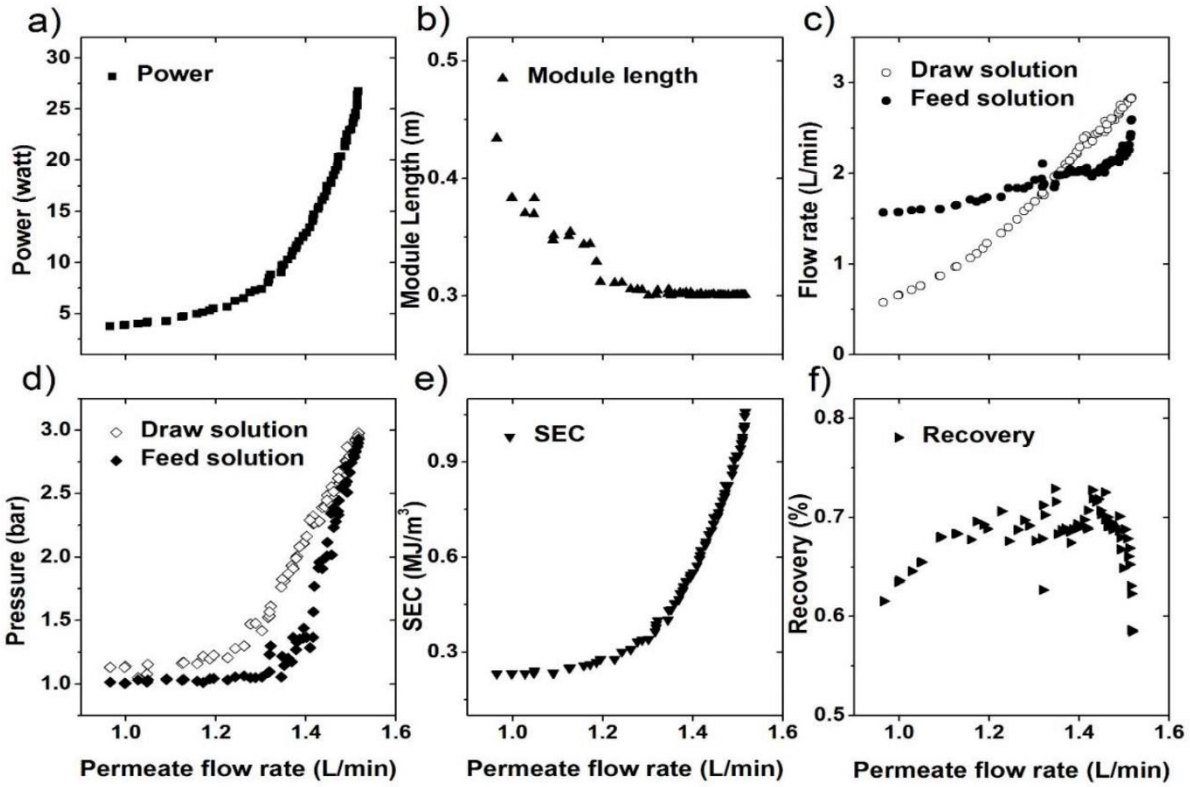

Figure 4-7 (a) FO Pareto set and (b - f) decision variables at optimal condition with respect to permeate flowrate (objective f(2))

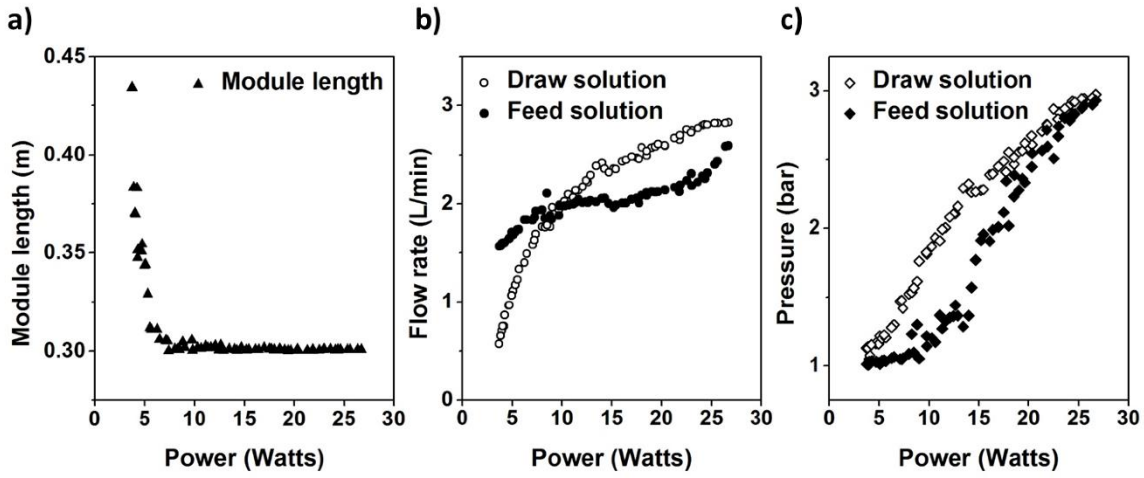

Figure 4-8. (a-c) Decision variables at optimal condition with respect to Power (objective f(1))

It is very important to investigate the specific energy consumption per unit permeate volume (SEC) against the permeate flow rate, as SEC is one of the important key parameters to assess the FO performance. The minimum SEC (0.23 MJ/m^3) of this module was observed at the lowest permeate flow rate (0.97 L/min) and, the maximum SEC (1.06 MJ/m^3) was observed at the highest permeate flow rate (1.52 L/min), as shown in Figure 4-7 (e). At the minimum SEC, the DS flow rate was minimum while the module length was maximum. The minimum SEC showed the worst scenario for the permeate flow rate but the best-case scenario in terms of power consumption. But maintaining a low SEC in a commercial production unit might require a large number of these modules as the net permeate flow rate per module is small. Thereby, it becomes necessary to decide the "target permeate flow rate" suitable enough to overcome high SEC and low production rates.

Further, at the optimum condition, the corresponding water recovery of the Toyobo HF FO module was plotted against the permeate flow rate (Figure 4-7 (f)). The recovery was calculated by dividing the permeate flow rate by the inlet FS flow rate, and it varied from 58.47 to 72.88 %. The initial DS flow rate in Figure 4-7 (c) exhibits the insufficient DS flow rate condition as discussed in the simulation section, and this resulted in low recovery. The plot also showed that a 50 % increment in the DS flow rate from minimum (0.5 L/min) to threshold value (1 L/min) was needed to improve the recovery by 10 %. The tail end of the FS flow rate plot represents the region of high permeate flow rate with low recovery. The maximum FS recovery from the Pareto results was observed between the threshold values of DS and FS flow rates. This region shows the optimum working conditions for the FO process.

The above discussion on the optimal points is carried out at C_{DS} = 50 kg/m^3 using the Toyobo membrane described in Table 4-1. At each optimal point of the FO plant, the cost of production will include the pumping cost, the initial investment cost for the modules, and the operational and maintenance cost. The number of modules can be calculated using the target permeate and permeate per unit module, and this number directly affects the maintenance cost. For example, if the target flux is 100 m^3/day (69.44 L/min), the above Pareto gives a range of 45-72 modules. Thus, to

obtain the best solution, the cost of production incurred for a given target flux has to be compared.

A procedure for identifying the optimal solution from a given pilot-scale experiment is shown in a flow sheet depicted in Figure 4-9. The described procedure provides the most profitable scenario in two steps. First, all the optimal points of operation and design for a given membrane area will be found. In this step, the external factors

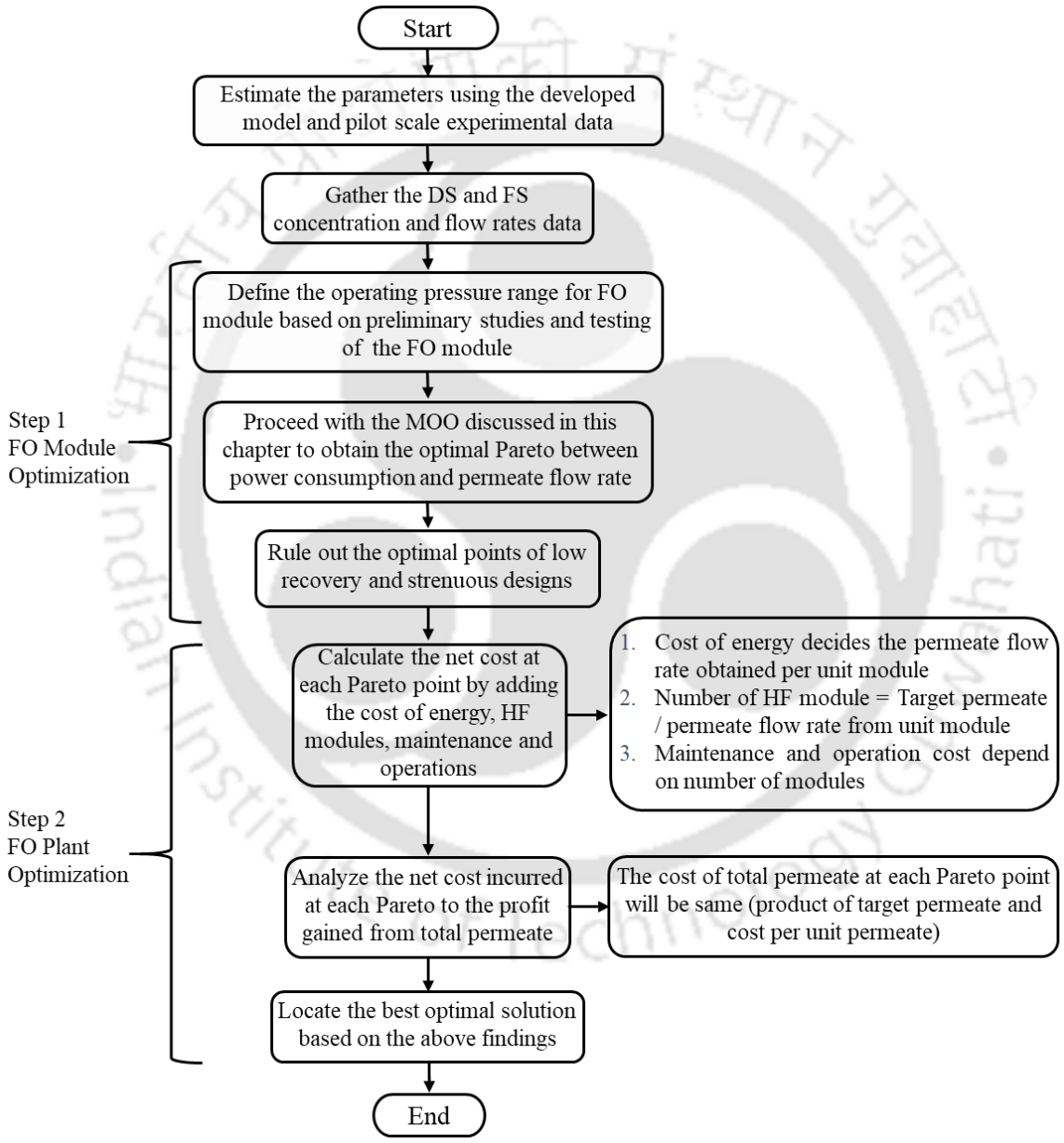

Figure 4-9. A flow chart for identifying the optimal solution of the FO plant from pilot-scale experiments

will be excluded, and focus will only be given to the internally coupled process of mass and momentum transform in the module and the corresponding energy consumed by the pump. In the second step, the number of modules, cost of energy, maintenance cost based on the first step will be included. This two-step technique enables the application of this procedure to any pure FO and FO-integrated process. In cases where the parameters are available in advance, the MOO study discussed can be applied. A sample example of this method is shown in the next section.

4.3.4 Sample Problem for FO Process Optimization

The application of Pareto results in the FO plant using a sample problem is discussed below. All the data provided here are assumptions. The calculation is based on permeate production of Q_{desire} = 10,000 m^3/day for the life span of t = 20 years. For simplification, cost factors like construction, piping, lining, pumps, etc., are lumped together with the operation and maintenance cost. The effect of interest rate, depreciation rate, and other fees are omitted from the cost calculations.

First, find the cost of FO modules required at each Pareto as,

$$\text{Number of modules } (N_m) = \frac{\text{Target flux}}{\text{Permeate flow rate from unit module}} \tag{4.40}$$

$$\text{Cost of FO module } (C_1) = N_m (\text{Cost of unit module}) \tag{4.41}$$

The power consumption for producing 1 m^3 of permeate volume can be calculated as,

$$\text{Power consumed per permeate volume} = \frac{\text{power consumed per hour}}{\text{permeate volume produced in one hour}} \tag{4.42}$$

where power consumed per permeate volume is in kWh/m^3, the power consumed is in kWh and permeate volume is in m^3. The power consumption cost of 10,000 m^3/day for 20 years (C_2) can be calculated using

$$C_2 = \text{Cost}_{energy} (\text{Power consumed per permeate volume}) Q_{desired}\, t \tag{4.43}$$

where C_2 is the power consumption cost for the specified duration in \$, $Cost_{energy}$ is in \$/kWh, C_1 is FO module cost in \$, Q_{desire} is the target permeate volume per day in m^3/day and t is the life span in days.

The cost of operation and maintenance (C_3) for 20 years is assumed to be

$$C_3 = X + N_m Y \tag{4.44}$$

where, X and Y are fixed and variable cost of operations in \$, respectively, and are dependent on elements number employed.

If the contribution of C_3 to the total cost is assumed to be 45 %, then the total cost (C_T) can be calculate using

$$C_T = \frac{C_1 + C_2}{0.55} \tag{4.45}$$

Table 4-5. Variable parameter for FO cost calculation

Parameter	Unit	Price (\$)
FO module	single module	1000
Energy Consumption	kWh	0.1

The optimal permeate flow rate for Table 4-5 conditions was shown in Figure 4-10.

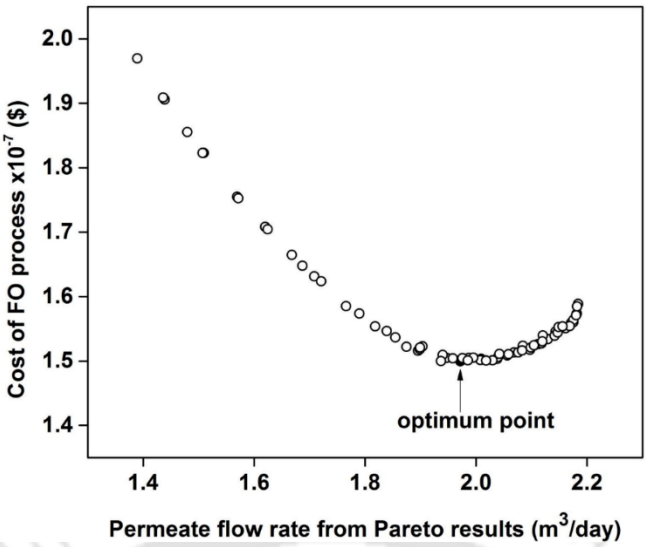

Figure 4-10. The cost of FO process estimation with respect to the permeate flow rate obtained from the Pareto result. At the optima, the module design and operating conditions were L = 0.3028 m, Q_{DS} = 2.17 L/min, Q_{FS} = 2.01 L/min, P_{DS} = 2.08 bar and P_{FS} = 1.35 bar

4.4 Summary

In this chapter, a mathematical model was successfully developed for the axial flow HF FO membrane module. The model, along with the experimental results, was used to estimate the membrane parameters. The estimated parameters were validated using another set of experimental data. The validated model was then used for simulation and optimization studies at various module lengths and operating conditions (pressure and flow rate of DS and FS). In addition, the applicability of the Ergun equation and Hagen-Poiseuille equation for estimating the pressure drop on the shell and lumen side, respectively, were experimentally investigated. The performance of the HF FO membrane was evaluated with respect to net permeate flow rate, total power consumption, and specific energy consumption. The simulation results indicated that the length of the module plays an important role in the performance of the HF FO module, and at the optimum length, the draw solution flow rate was found to be a major contributor to the FO water flux. Further, an optimum trade-off between the FO water flux and power consumption was found compulsory to ensure the economic feasibility of the FO process. Moreover, a two-

step procedure was developed to identify the optimal design and operational conditions from a given pilot-scale FO experiment.

Chapter 5 Experimentation, Modeling and Optimization Studies on Axial Flow Hollow Fiber Pressure Retarded Osmosis Process

Parts of this Chapter is published as research articles:

- **H. T. Aseffa**, D. K. Gautam, and S. Subbiah, "Optimization of Pressure Retarded Osmosis Process and Estimation of Indian Blue Energy Capacity" p. 114752, 2020 https://doi.org/10.1016/j.desal.2020.114752

Experimentation, Modeling and Optimization Studies on Axial Flow Hollow Fiber Pressure Retarded Osmosis Module

This chapter presents a mathematical model for an axial flow HF PRO module, which is capable of calculating the net hydraulic power generation by the PRO process. Similar to HF FO batch process modeling, the mathematical model of the PRO process combines the unsteady state tank model and the steady-state HF PRO module model. Due to the presence of high pressure in the shell side, the applicability of the Ergun equation and Hagen-Poiseuille equation (to estimate the pressure drop on the shell and lumen side, respectively) are experimentally investigated for the PRO conditions. Also, a flow chart is presented to solve the batch PRO process model equation and estimate the unknown parameter of the HF PRO module model. Then, the energy recovery system along with PRO process model is simulated to study the sensitivity of the PRO process operating condition and module length by calculating the net hydraulic power generation from the PRO process for the Indian River and seawater conditions. Finally, the optimized PRO process is used to estimate the Indian blue energy potential by mixing river and seawater before discharging into the sea.

5.1 Theory

In 1976, the PRO process was proposed by Loeb et al. [15] for generating hydraulic energy from the mixing of seawater and freshwater. In the FO process, there is no external force applied in either side of the solution, whereas, in PRO, the DS side is pressurized to produce power from the hydraulic turbine. In the case of the HF module, the high-pressure DS should be supplied through the shell side to avoid fiber burst. Applying high pressure in the shell side also results in fiber compression and a change in fiber shape and dimension. This phenomenon is expected to provide additional uncertainty while using the HF FO model proposed in this work for the PRO process. Hence, to take care of this effect in the PRO process, the effect of external pressure force in the HF shell side should be incorporated in the solvent flux, the Hagen Poiseuille, and the Ergun equation. This effect requires a modification of the proposed FO model equations in the previous chapter. In addition, the proposed optimization problem of the FO process is not applicable to

the PRO process. Therefore, the optimization problem for the PRO process is formulated to maximize the net hydraulic energy per unit quantity of freshwater.

5.1.1 Modeling of the PRO Batch Process

The mathematical model of an axial flow HF PRO module used in this chapter is expected to calculate the net power generation by PRO process for a given operating condition such as inlet flow rate, concentration, and pressure of the FS and DS, and model parameters such as the PRO membrane properties, module dimensions and coefficients of empirical correlation. The HF PRO mathematical model combines the unsteady state tank model and the steady-state HF PRO module model. The tanks, which act as continuous sources and sinks to the HF PRO module, are formulated as an unsteady state model owing to the continuous change in the tank solution concentration and volume.

The concentration and flow rate of FS and DS are expected to vary across the module length, and by assuming uniform fiber distribution across the radial position, the variation in the radial direction is assumed to be negligible. Also, the residence times of FS (0.12 s) and DS (0.45 s) in the HF module are lower than the FS and DS tank resistance, i.e., the response of the HF PRO module is observed much faster than both FS (300 s) and DS (212 s) tank at the standard operating condition. Therefore, 1-dimensional (1D) unsteady state PRO model equation is solved in this chapter and validated using experimental data generated in this work along with the tank model. The validated model will be used to improve the PRO module performance by maximizing net power generation while manipulating the operational condition (pressure and flow rate) and design variable (module length).

5.1.1.1 Assumptions Taken While Developing the 1D HF PRO Model

The 1D HF PRO model is established by solving mass and momentum balance equations along with the axial direction local membrane transport equation. In addition to the assumptions made for the HF FO model in section 4.1.1.3 (i.e.,

assumption (i) to (vii)), the following assumptions are made while developing the HF PRO model.

(i) Flow inside the lumen side is laminar such that modified Hagen-Poiseuille is used for lumen side pressure drop calculation [74].

(ii) Seawater and river water are assumed to be a single solute made of NaCl alone.

5.1.2 Membrane Transport Equations

The SD model is used to represent the solvent and solute movement through the semi-permeable membrane for the PRO process. As reported in various literature [55,109,110,123,124], J_W and J_S are affected by both ICP and ECP effects. The basic equations of the J_W and J_S incorporating these effects for ALDS orientation (as depicted in Figure 3-1) are shown in Eq. 5.1 and Eq. 5.2. The derivation for the solvent and solute flux is presented in Chapter 4, section 4.1.2.

$$J_W = A\left(\left(\frac{iRT}{M_W}\right)\left(\frac{C_{DS}\exp\left(-J_W/k_{DS}\right) - C_{FS}\exp\left[J_W\left(S/D_{diff} + 1/k_{FS}\right)\right]}{1+\frac{B}{J_W}\left(\exp\left[J_W\left(S/D_{diff} + 1/k_{FS}\right)\right] - \exp\left(-J_W/k_{DS}\right)\right)}\right) - \Delta P_{PRO}\right) \quad (5.1)$$

$$J_S = B\left(\frac{C_{DS}\exp\left(-J_W/k_{DS}\right) - C_{FS}\exp\left[J_W\left(S/D_{diff} + 1/k_{FS}\right)\right]}{1+\frac{B}{J_W}\left(\exp\left[J_W\left(S/D_{diff} + 1/k_{FS}\right)\right] - \exp\left(-J_W/k_{FS}\right)\right)}\right) \quad (5.2)$$

Where ΔP_{PRO} is the hydraulic pressure drop between the shell and lumen side in [Pa].

As explained in section 4.1.3, the solute permeability coefficient (B) is calculated using Eq. 4.16, and the FS and DS side mass transfer coefficients are estimated using Eq. 4.11. The structural parameter was also reported as a solute concentration-dependent by Xia et al. [120]. Hence, to incorporate such changes in this study, the solute diffusivity at the porous support layer is represented using a solute concentration (refer to section 4.1.2) [121]. The solute resistivity (K) is used to

quantify the FS solute accumulation in the porous support layer [55,109] using Eq. 3.7.

5.1.3 Mass Balance for the HF PRO Module

The schematic diagram representing the flow configuration of the HF PRO module is shown in Figure 4-1. The Toyobo pilot-scale HF FO module [Model No. HPC 3205] is used to conduct all the experimental studies. Though this module is made for FO process, in this study, the module is used to analyze the performance of the PRO process. In the HF module, the DS is flowing through the shell side, and the FS is flowing through the lumen side. The water and solute balance for both the shell side (DS) and lumen side (FS) is the same as the one given in Eqs. 4.18 – 4.21. However, the water and solute fluxes are estimated using Eq. 5.1 and Eq. 5.2, respectively.

5.1.4 Momentum Balance (Pressure Drop) Equations

As shown in Figure 4-1, the hollow fibers are packed in a structured manner with constant packing density by sealing both ends of packed fibers. This arrangement will allow both DS and FS to flow in an axial direction. The hydrodynamic in the shell side of the module can be assumed as flow over a packed bed with uniform packing density. Therefore, in this work, the Ergun equation is used for calculating the momentum loss (i.e., pressure drop) across the shell side. The Ergun equation (Eq. 4.22) that incorporates both kinetic and viscous losses terms is used to calculate the momentum loss in the shell side.

In the Ergun equation, the term porosity is assumed to be constant, but due to external compression, they are expected to increase as the shell pressure increases. The incorporation of such variation in the Ergun equation requires fiber compression data with respect to external pressure, and such data is not reported yet in literature. Due to this phenomenon, the pressure drop in the shell side was miscalculated by the Ergun equation [74], and further, the constants 150 and 1.75 were re-estimated to represent the experimental observation. Therefore, in this work, the Ergun equation constants are taken from the authors' previous study, which was estimated for the

same HF module by using pure water experimental data in RO mode, i.e., 186.06 and 97.91 [74].

For lumen side pressure calculation, the Hagen-Poiseuille equation (Eq. 4.23), (which is applicable for laminar flow condition, Re < 2100) is used [34,53,88]. Though the Hagen-Poiseuille equation can be used for the laminar regime, it assumes that the (i) liquid flows on a non-porous tube with smooth surfaces. But in the PRO process, water flux is expected across the membrane from the lumen side to the shell side. (ii) tubes are cylindrical, but due to external pressure, the fibers might be compressed, and that may result in a change in diameter and cylindrical structure. A correction factor is introduced in the Hagen-Poiseuille equation to calculate the actual lumen side pressure drop as follows [74]

$$\frac{dP_{lumen}}{dz} = HP_{factor}\frac{32\mu_{lumen}u_{lumen}}{d_i^2} \tag{5.3}$$

Where HP_{factor} is the Hagen-Poiseuille correction factor. It can be estimated during the model validation process by using PRO experimental data. The length of the epoxy seal at the entrance and exit of the lumen side is included while calculating the pressure value in the active portion of the module (middle portion of the HF module 'L' as shown in Figure 4-1). The pressure drop in the epoxy seal at the entrance and exit of the lumen side is given by,

$$\Delta P_{epoxyseal} = \frac{32\mu_{tube}u_{tube}}{d_i^2}l_s \tag{5.4}$$

Where, l_s is the length of the epoxy seal and the fiber before the DS inlet port (l_s = 0.055 m).

The above modifications in the predefined and well-characterized pressure drop equations are vital as these parameters, i.e., shell and lumen side pressure drop decide the productivity of the process.

5.1.5 Tank Mass Balance Equations

In developing the mathematical HF PRO model, a tank model is added to the HF module model to accurately represent the continuous re-circulation system. In the tank model, the tank outlet flow is directly connected to the module inlet flow and, the module outlet flow is connected to the tank inflow. The schematic diagram showing these tanks and module flow conditions is shown in Figure 4-3. In addition, the mass and solute balance for DS and FS tanks are expressed by Eqs. 4.24 – 4.28.

The net hydraulic power generation by stand-alone HF PRO module can be calculated using the below equation,

$$Pow_{Net,HF\,PRO} = P_{DS,outlet}Q_{DS,outlet} - P_{DS,inlet}Q_{DS,inlet} - P_{FS,inlet}Q_{FS,inlet} \quad (5.5)$$

5.1.6 Method for Solving the PRO Model Equation

All the model equations for the HF PRO process are coded and solved using MATLAB 2019a academic version (Mathworks, Natick, MA, USA) platform. The membrane parameters are estimated using the weight and concentration change of both the DS and FS tank measurements, which are measured from the batch PRO experiments. The model equations are solved using the method explained in Figure 4-2 with the following modification. (i) The error function (5.14) is modified to incorporate the deviation of the FS side pressure drop, (ii) HP_{factor} is estimated as an additional parameter, and (iii) the effect of the epoxy seal at the entrance and exit of the fiber is considered to calculate the FS side pressure ($P_{FS,i} = P_{FS,inlet} - \Delta P_{epoxy\ seal}$). The HF PRO module is divided into 'n' elements, and the mass and momentum balances are performed for the individual segment. The number of elements was fixed based on prior simulations carried to compare the value of water flux versus the number of elements. It was observed that the change in the HF module water flux was negligible beyond 100 numbers of elements. Thus, this value was fixed for all the further simulations. The model equation is solved by providing the following inputs: process operating conditions (such as $C_{DS,inlet}$, $C_{FS,inlet}$, $V_{DS,inlet}$ and $V_{FS,inlet}$), model parameters (such as molecular weight, membrane area, shell, and lumen size),

membrane transport parameter (such as A, B, S), module parameters (coefficient of mass transfer coefficient, constant of the Ergun and Hagen-Poiseuille equation) and solution physical properties (such as density, viscosity). Later, the unknown model parameters are predicted using batch PRO experimental data.

5.1.7 Modeling of PRO Process with Energy Recovery Device (ERD)

As shown in Figure 5-1, the PRO process is integrated with an energy recovery device (ERD) / pressure exchanger (PX) to maximize the net power generation from the overall system. Also, the pretreatment system for both river and seawater is required to minimize the membrane fouling with appropriate pumps and turbines for energy generation. The energy consumption and generation by pumps and turbines are presented in this section. As depicted in Figure 5-1, part of the high-pressure diluted seawater is passed through the turbine, and the balance amount is used to pressurize the input seawater by using ERD. The flow rate ratio between ERD and HF PRO module is defined as λ, and it has to be estimated to maximize the net power generation from the turbine. Hence, the flow ratio λ can be taken as one of the decision variables while optimizing the net hydraulic power generation from the PRO system.

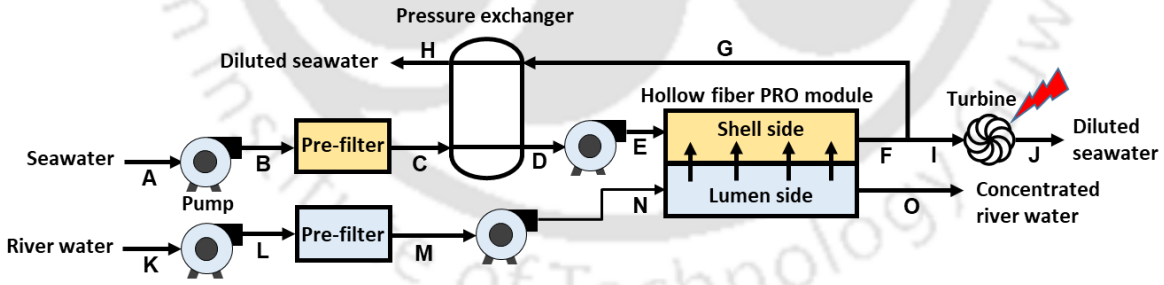

Figure 5-1. Process flow diagram of the ERD/PX integrated PRO process

$$\lambda = \frac{\left(Q_{DS,outlet}\right)_{PX}}{\left(Q_{DS,outlet}\right)_{HF\ PRO}} \tag{5.6}$$

The energy consumed by the pumps ($Energy_{Pump}$), energy recovered by the pressure exchanger ($Energy_{PX}$), energy generated by the turbine ($Energy_{Tur}$) and the energy generated by the PRO system ($Net\ Energy_{PRO\ system}$) can be calculated using

$$Energy_{DS,Pump} = \frac{\Delta P_{DS,Pump} Q_{DS,inlet}}{\eta_{DS,Pump}} \tag{5.7}$$

$$Energy_{FS,Pump} = \frac{\Delta P_{FS,Pump} Q_{FS,inlet}}{\eta_{FS,Pump}} \tag{5.8}$$

$$Energy_{DS,Filter,Pump} = \frac{\Delta P_{DS,Filter,Pump} Q_{DS,inlet}}{\eta_{DS,Filter,Pump}} \tag{5.9}$$

$$Energy_{FS,Filter,Pump} = \frac{\Delta P_{FS,Filter,Pump} Q_{FS,inlet}}{\eta_{FS,Filter,Pump}} \tag{5.10}$$

$$Energy_{PX} = \eta_{PX} \Delta P_{PX} \lambda Q_{DS,outlet} \tag{5.11}$$

$$Energy_{Turbine} = \eta_{Tur} \Delta P_{Tur} (1-\lambda) Q_{DS,outlet} \tag{5.12}$$

$$\begin{aligned} Net\ Energy_{PRO\ system} = {} & \eta_{Tur} \Delta P_{Tur} (1-\lambda) Q_{DS,outlet} - \left(\frac{\Delta P_{DS,Filter,Pump} Q_{DS,inlet}}{\eta_{DS,Filter,Pump}} \right) \\ & - \left(\frac{\Delta P_{DS,Pump} Q_{DS,inlet}}{\eta_{DS,Pump}} - \eta_{PX} \Delta P_{PX} \lambda Q_{DS,outlet} \right) \\ & - \left(\frac{\Delta P_{FS,Pump} Q_{FS,inlet}}{\eta_{FS,Pump}} \right) - \left(\frac{\Delta P_{FS,Filter,Pump} Q_{FS,inlet}}{\eta_{FS,Filter,Pump}} \right) \end{aligned} \tag{5.13}$$

Where $\Delta P_{DS,Pump}$, $\Delta P_{FS,Pump}$, $\Delta P_{DS,Filter,Pump}$, $\Delta P_{FS,Filter,Pump}$, ΔP_{PX} and ΔP_{Tur} are the pressure difference across the DS pump, FS pump, DS filter pump, FS filter pump, pressure exchanger and turbine, respectively. $\eta_{DS,Pump}$, $\eta_{FS,Pump}$, $\eta_{DS,Filter,Pump}$,

$\eta_{FS,Filter,Pump}$, $\eta_{PX,}$ and η_{Tur} are the efficiency of DS pump, FS pump, DS filter pump, FS filter pumps, pressure exchanger, and turbine, respectively.

5.1.8 Method for Membrane Parameter Estimation

The model parameters such as the intrinsic membrane properties (A, S, and B (C*, m, b_0)), Hagen-Poiseuille correction factor (HP_{factor}) and mass transfer coefficient parameters (α_{DS}, and α_{FS}) are unknown. The hydrodynamic membrane permeability (A) and the Ergun equation constants (e_1 and e_2) are estimated by using distilled water, as reported in the authors' previous study [73,74]. The remaining parameters are estimated (using the method shown in Figure 4-2) by formulating an objective function that minimizes the error between model outputs and experimental results, as given in Eq. 5.14. While estimating the parameter at high water permeability, the PRO model may result in a negative or zero FS outlet flow rate in the lumen side. Hence, to avoid such scenarios (or make $Q_{FS,outlet}$ > 0.5 L/min) during parameter estimation by GA, a penalty is added in terms of soft constraint in the error function. In this study, the GA library available in MATLAB (MATLAB R2019a-academic version - Optimization Toolbox 8.3) is used to reduce the error and estimate the model parameters.

$$Error = \sum_{t=0}^{n} \left[\left| \frac{C_{DS,\exp,t} - C_{DS,\mathrm{mod},t}}{C_{DS,\exp,t}} \right| + \left| \frac{C_{FS,\exp,t} - C_{FS,\mathrm{mod},t}}{C_{FS,\exp,t}} \right| + \left| \frac{\Delta V_{\exp,t} - \Delta V_{\mathrm{mod},t}}{\Delta V_{\exp,t}} \right| + \left| \frac{\Delta P_{DS,\exp,t} - \Delta P_{DS,\mathrm{mod},t}}{\Delta P_{DS,\exp,t}} \right| + \left| \frac{\Delta P_{FS,\exp,t} - \Delta P_{FS,\mathrm{mod},t}}{\Delta P_{FS,\exp,t}} \right| \right] + penalty\ for\ Q_{FS,outlet} \tag{5.14}$$

where P and the subscript t, exp and mod stands for pressure, batch time, experimental and model results, respectively.

The bounds for the model parameters are given below

$$1 \le HP_{factor} \le 5 \qquad 1 \le C^* \le 75 \qquad 10^{-11} \le b_0 \le 10^{-6} \qquad 0.01 \le \alpha_{FS} \le 0.99$$

$$10^{-14} \le m \le 10^{-8} \qquad 4x10^{-5} \le S \le 2x10^{-3} \qquad 0.01 \le \alpha_{DS} \le 0.99$$

5.1.9 Formulation of an Optimization Problem for the HF PRO Module

In this section, three different optimization problems are presented to calculate the optimal value of Q_{FS}, Q_{DS}, P_{FS}, P_{DS}, L, and λ to achieve maximum net hydraulic power production per unit $Q_{FS,inlet}$ from the PRO process. The first objective function is formulated by dividing the net hydraulic power generation by the FS inlet flow rate, as shown in Eq. 5.15. To study the importance of $Q_{FS,inlet}$ in the first objective function, the second objective function is formulated without $Q_{FS,inlet}$ in the denominator (Eq. 5.16). Finally, the third objective function is formulated to maximize the power density of the HF PRO module (Eq. 5.17). After evaluating all three objective function results, the best formulation will be chosen for calculating the blue energy potential of Indian river water.

$$Max\ f = \frac{Net\ Energy_{PRO\ system}}{Q_{FS,inlet}} - Penalty\ for\ P_{DS,D} - Penalty\ for\ Q_{FS,outlet} \quad (5.15)$$

$$Max\ f = Net\ Energy_{PRO\ system} - Penalty\ for\ P_{DS,D} - Penalty\ for\ Q_{FS,outlet} \quad (5.16)$$

$$Max\ f = J_W \Delta P - Penalty\ for\ P_{DS,D} - Penalty\ for\ Q_{FS,outlet} \quad (5.17)$$

$$Penalty\ for\ P_{DS,D} = 1x10^{10} \begin{cases} \left(P_{DS,D} - (P_{DS,G} - 1)\right) & if\ \left(P_{DS,G} - P_{DS,D}\right) < 1 \\ 0 & if\ \left(P_{DS,G} - P_{DS,D}\right) \geq 1 \end{cases}$$

$$Penalty\ for\ Q_{FS,outlet} = 1x10^{10} \begin{cases} \left(0.5 - Q_{FS,outlet}\right) & if\ Q_{FS,outlet} < 0.5 \\ 0 & if\ Q_{FS,outlet} \geq 0.5 \end{cases}$$

Where Net $Energy_{PRO\ system}$ is the net hydraulic power produced (Watt) from the PRO process as given in Eq. 5.13. $P_{DS,D}$ and $P_{DS,G}$ are the DS pressure at locations D and G, respectively (refer to Figure 5-1). The DS pressure at location D is calculating using

$$P_{DS,D} = \frac{Energy_{PX}}{Q_{DS,outlet}} + P_{DS,C} \quad (5.18)$$

Further, the penalty functions were introduced in the objective functions (Eq. 5.15-5.17) to incorporate the inequality constraints $Q_{FS,outlet} \geq 0.5$ L/min anywhere along the length of the module, and to assure that $(P_{DS,G} - P_{DS,D}) \geq 1$ bar. The above-defined optimization problems are solved using Indian seawater and river water conditions as DS and FS solutions, respectively. The TDS of Indian major river waters are reported in Table C. 2 (refer to appendix).

While manipulating the module length, the membrane surface area is expected to vary. In order to maintain constant membrane area throughout this study, the HF PRO module dimension (i.e., module diameter) was estimated by keeping the membrane area, the inner and outer diameter of the fiber, and module porosity constant. The surface area of the membrane (A_M) is calculated using Eq. 4.33 and the porosity (ε) of the module is fixed to a constant value as given in Eq. 4.34.

5.2 Materials and Methods

5.2.1 Specifications of the HF Module

All the PRO experimental studies are conducted using the HF FO module with specification shown in

Table 4-1.

5.2.2 Experimental Setup

The schematic diagram of the experimental setup for the HF PRO process is provided in Figure 4-3. The HF FO module was used for analyzing the performance of the PRO process. The main difference between FO and PRO experiments lies in the presence/absence of external pressure on the shell side. In the case of the FO experiment, the control valve, which is placed at the outlet of the shell side, is always fully open, whereas, in the case of the PRO experiment, the control valve is partially closed until the desired pressure is attained in the shell side. All the PRO experiments

are performed in co-current mode by circulating both DS and FS in the same direction through the axial flow HF FO module.

5.2.3 Experimental Procedure

In this study, before performing each experiment, deionized water is used to clean both the shell and lumens side flow path. Then, RO treated water with total dissolved solids (TDS) of 0.01 kg/m^3 (conductivity = 9.8 x 10^{-3} μS/m) is used to prepare the FS and DS of 0.01 kg/m^3 and 50 kg/m^3, respectively, by mixing analytical grade NaCl (Merck Life Science Pvt. Ltd, India, purity > 99.5%). As shown in Figure 4-3, the DS and FS were circulated through the shell and the lumen side, respectively. Before circulation, both solutions together; first, the DS is recirculated in the shell side until steady-state draw NaCl concentration is observed in the DS tank. During this process, the lumen side valves are kept closed. After stabilizing DS solution concentration in the flow path, both FS and DS circulated together. The shell side pressure is pressurized to 8.0 bar using a control valve.

Table 5-1. The experimental conditions for the HF PRO mode

	units	Shell side	Tube side
Solution type	-	Draw solution	Feed solution
Volume of solution	L	4.2	10
Concentration	kg/m^3	45 and 30	< 0.01
Flow rate	L/min	1.3	2.2
Pressure	bar	8.0	3.0
Temperature of solution	°C	25	25

As the batch process continues, due to DS dilution, the process condition changes dynamically. Dynamic variation in flow, pressure, temperature, tank weight and

conductivity are measured and recorded in the data acquisition system for every one-second interval. The experimental condition for the HF PRO process is shown in Table 5-1. Another set of PRO experiment is repeated with lower initial DS concentration, i.e., 30 kg/m^3. For better accuracy, each experimental set is repeated three times and the average is reported.

5.3 Results and Discussion

5.3.1 HF PRO Membrane Characterization and Model Validation

The unknown model parameters were estimated by minimizing the error function (Eq. 5.14) for PRO batch experiments data with an initial draw NaCl concentration of 50 kg/m^3. The tuned model is validated for PRO batch experiment data with an initial draw NaCl concentration of 30 kg/m^3. The bounds for the decision variable are given below

$$1 \le HP_{factor} \le 5 \qquad 1 \le C^* \le 75 \qquad 10^{-11} \le b_0 \le 10^{-6} \qquad 0.01 \le \alpha_{FS} \le 0.99$$
$$10^{-14} \le m \le 10^{-8} \qquad 4x10^{-5} \le S \le 2x10^{-3} \qquad 0.01 \le \alpha_{DS} \le 0.99$$

For this study, the water permeability value (1.108 x 10^{-12} m^3/m^{2}sPa) was taken from the experimental result found in Figure B. 1 (refer to appendix). Similarly, the empirical constant of the Ergun equation is taken from the authors' previous study, i.e., 186.06 and 97.91, as these constants are estimated for the same HF module using pure water RO experimental data [74]. The other parameters are estimated by GA at optimal error function, and the value are as follows: HP_{factor} = 2.38, C* = 0.01 kg/m^3, m = 2.75 x 10^{-10} m^4/(s kg), b_0 = 3.702 x 10^{-8} m^3/(m^2 s), S = 635 µm, α_{DS} = 0.246, and α_{FS} = 0.096.

As shown in Table 5-2, the results of these parameters are compared with the literature reported value for the HF module, similar to the one used in this study. The intrinsic membrane parameters estimated by Shibuya et al.,2016 [53] and Tanaka et al., 2018 [52] were found by preliminary RO and FO experiments using 720 fibers. In their study, the concentration of FS, dilution of DS, and pressure drop that are not negligible in the case of large modules were ignored. However, in this study, these

effects were incorporated into the model equations. Another factor might be due to the inclusion of external concentration polarization in the FS side. This might lower S as k_{FS} is taking care by the ECP on the FS side. In addition, in the current work, the PRO experimental data is used for the parameter estimation, and this might influence the results.

Table 5-2. Estimated parameter comparison from the model

Reference	Water permeability coefficient, A x 10^{12} $m^3/(m^2\ s\ Pa)$	Solute permeability coefficient, B x 10^9 $m^3/(m^2\ s)$	The structural parameter, S µm
This study	1.108	37.02 for $C_{DS,inlet} \geq 0.01$ kg/m^3 0.275 x $C_{DS,inlet}$ + 37.02 for $C_{DS,inlet} < 0.01$ kg/m^3	635
[53]	0.75	9.72	1024
Tanaka et al., with module 1 [52]	0.75	9.72	1024
Tanaka et al., with module 2 [52]	1.67	20	912
Note: The specifications of Module 1 and 2 are different			

The comparison between experimental results and model output is presented in Figure 5-2. Data used for parameter estimation is shown in Figure 5-2 (a) & (b). Similarly, the data used for model validation is shown in Figure 5-2 (c) and (d). The model was able to predict the water flux, DS, FS concentration, and DS outlet pressure with an average percentile error of less than 9.5% (Table 5-3). But the error on FS outlet pressure was observed to be ~17.15%, and this might be due to the low accuracy of the pressure sensor used for the FS line at the low-pressure range. For example, the observed FS pressure is less than 0.2 bar, and in this range, the error on the pressure sensor is expected to be around ±10 %. The HP_{factor} value indicates that the pressure drop in the lumen side is nearly 2.5 times the value estimated by the Hagen-Poiseuille equation in previous studies.

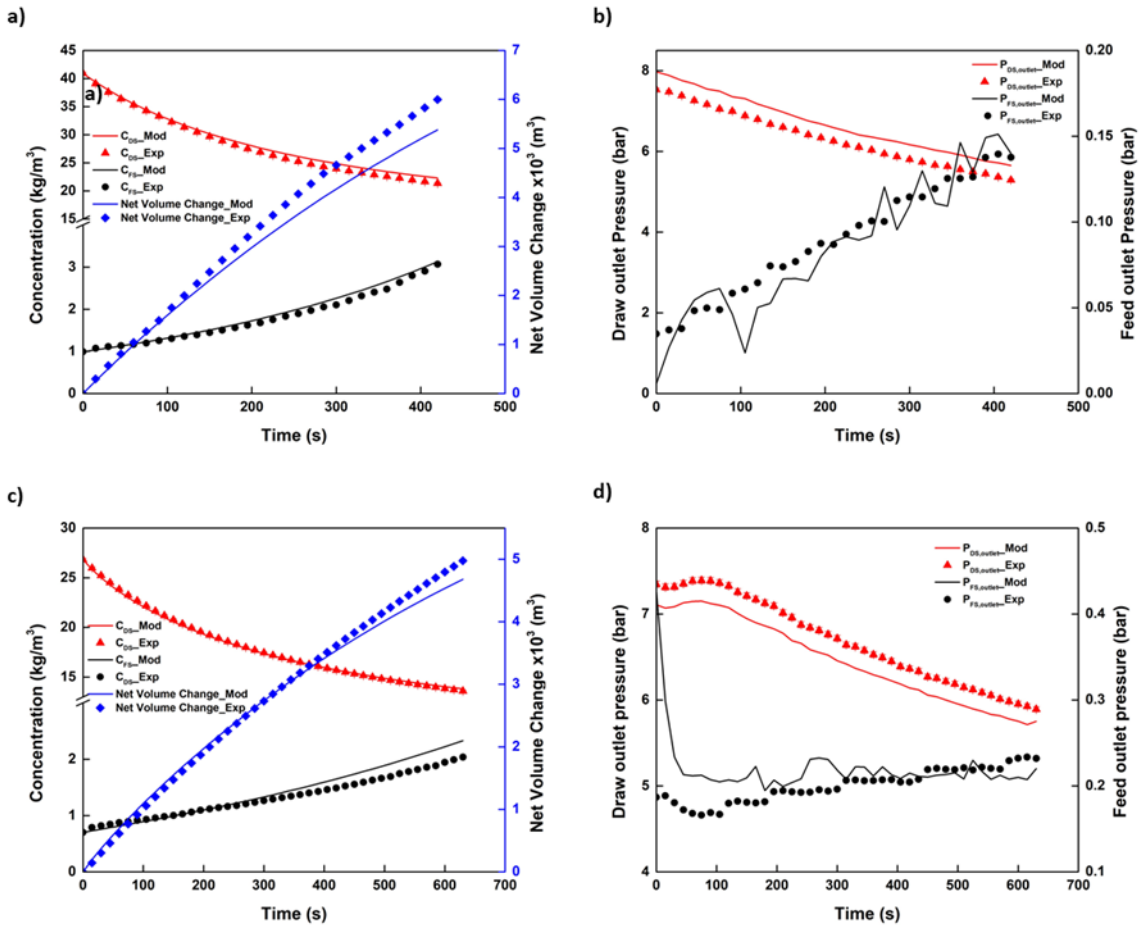

Figure 5-2. The HF PRO module experimental and model prediction comparison between C_{DS}, C_{FS}, net volume change and $P_{DS,outlet}$, $P_{FS,outlet}$ for experimentation condition (a and b): $C_{DS,inlet}$ = 50 kg/m³, $C_{FS,inlet}$ = 0.01 kg/m³, and validation condition (c and d): $C_{DS,inlet}$ = 30 kg/m³ $C_{FS,inlet}$ = 0.01 kg/m³

Table 5-3. Average percentile error between experimental results and model outputs for experimentation and validation of FS and DS concentration, outlet pressure, and net volume change.

	Average Percentile Error	
	Experimentation (50 kg/m^3)	Validation (30 kg/m^3)
C_{FS}	4.12	0.64
C_{DS}	2.44	9.45
Net volume change	8.25	2.7
P_{DS},out	9.04	3.51
P_{FS},out	20.5	6.64

Percentile Errors are calculated using

$$C_{FS}(\%) = \frac{100}{n}\sum_{i=1}^{n}\left|\left(\frac{C_{FS,\exp} - C_{FS,\mathrm{mod}}}{C_{FS,\exp}}\right)_i\right| \qquad P_{DS,outlet}(\%) = \frac{100}{n}\sum_{i=1}^{n}\left|\left(\frac{P_{DS,outlet,\exp} - P_{DS,outlet,\mathrm{mod}}}{P_{DS,outlet,\exp}}\right)_i\right|$$

$$C_{DS}(\%) = \frac{100}{n}\sum_{i=1}^{n}\left|\left(\frac{C_{DS,\exp} - C_{DS,\mathrm{mod}}}{C_{DS,\exp}}\right)_i\right| \qquad P_{FS,outlet}(\%) = \frac{100}{n}\sum_{i=1}^{n}\left|\left(\frac{P_{FS,outlet,\exp} - P_{FS,outlet,\mathrm{mod}}}{P_{FS,outlet,\exp}}\right)_i\right|$$

$$\text{Net volume change}\ (\%) = \frac{100}{n}\sum_{i=1}^{n}\left|\left(\frac{\text{Net volume change}_{\exp} - \text{Net volume change}_{\mathrm{mod}}}{\text{Net volume change}_{\exp}}\right)_i\right|$$

5.3.2 Simulation Studies on the HF-PRO Module

This simulation study aims to find the list of critical decision variables that impacts the net hydraulic power generation of the HF PRO module (Eq. 5.5). Also, the nature of the objective function with respect to the decision variable can be identified. The steady-state PRO model is used to compute the net hydraulic power generation by the PRO process. The following variables are considered for simulation: FS, DS flow rate, DS outlet pressure, and module length. Initially, the model was simulated by varying operational conditions such as draw flow rate, feed flow rate, and DS outlet pressure of the PRO module for a fixed module length. Then, the feed flow rate was

kept constant while varying the draw flow rate, module length, and DS outlet pressure. In addition to net power generation, the recovery of the PRO module is plotted with respect to $C_{DS,inlet}$. The recovery is defined as the ratio of permeate flow rate to FS inlet flow rate.

5.3.2.1 Effect of DS and FS Flow Rate

The net hydraulic power that can be generated using the HF PRO module (Eq. 5.5) was simulated for $C_{DS,inlet}$ = 50 kg/m^3, $C_{FS,inlet}$ = 0.01 kg/m^3, Q_{DS} = 1-8 L/min, Q_{FS} = 1.5-8 L/min and DS outlet pressures = 12.5-30 bar at fixed module length. The results of the simulation are presented in both surface and contour form. In the surface plot, multiple surfaces at different DS outlet pressure are provided at a fixed length refer Figure 5-3 (a) and (c)), and the contour plot for single DS outlet pressure is shown in Figure 5-3 (b) and (d)). It was found that, for lower module length, as the draw flow rate increases from1 to 8 L/min, the net hydraulic power generation is increasing and reaching an asymptotic value. However, for large module lengths, the net hydraulic power generated by PRO increases initially and later decreases as the draw flow rate increases. This behavior is observed due to the following two phenomena that occur in the HF PRO module while increasing the DS flow rate. (i) the overall osmotic pressure difference between DS and FS in the module increases due to less DS dilution. However, after achieving a sufficient DS flow rate, the dilution effect will be negligible. Therefore, net water flux (recovery) from FS to DS will increase and then reach an asymptotic value (refer to Figure 5-8). (ii) the increase in DS flow rate will also introduce more pressure drop in the shell side, and its impact will be high for larger module length, as shown in Figure 5-4. The increase in water flux will improve the net hydraulic power generation, and high-pressure drop will reduce the net hydraulic power generation. Overall, both phenomena are affecting in the opposite manner and result in an optimal point while manipulating the DS flow rate. The increase in the FS flow rate also results in a counter effect by both high FS dilution and high-pressure drop. Accordingly, initially, the net hydraulic power generation increased due to improved FS dilution effect, and later the power

generation has reduced due to high-pressure drop. Therefore, the optimum point is observed for a fixed DS flowrate.

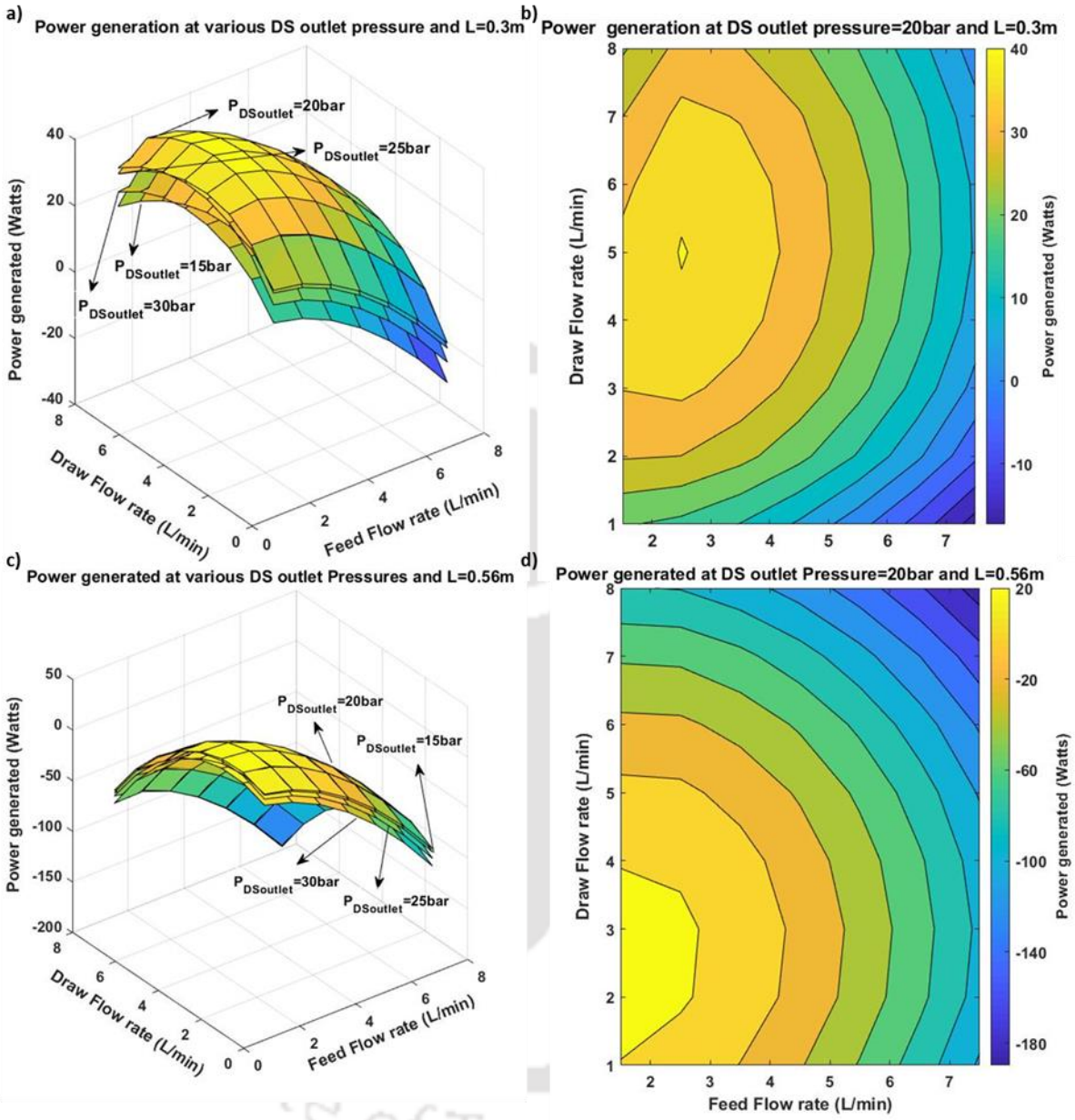

Figure 5-3. Net hydraulic power generation with respect to DS, FS flow rate, module length and DS outlet pressure (a) surface plot for L = 0.3 m, (b) Contour plot for L = 0.3 m and DS outlet pressure = 20 bar, (c) surface plot for L = 0.56 m and (d) contour plot for L = 0.56 m and DS outlet pressure = 20 bar

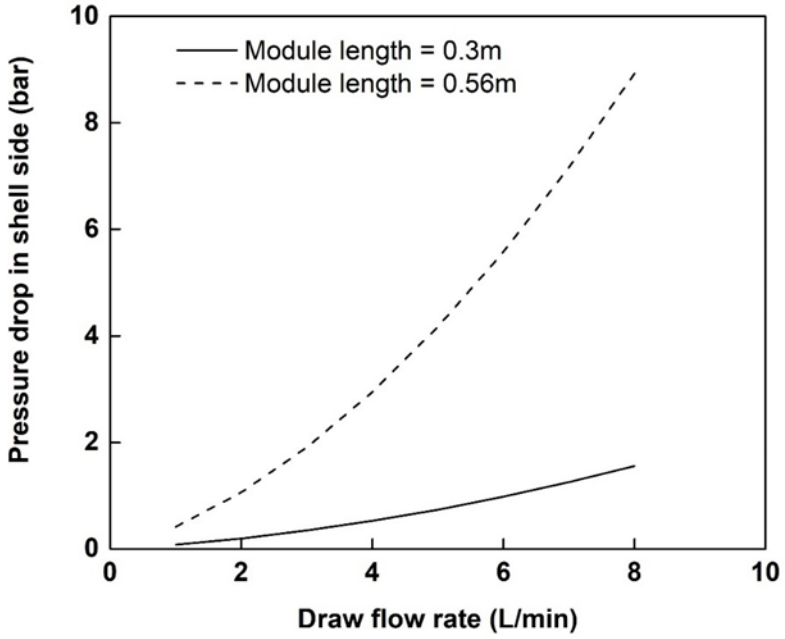

Figure 5-4. Pressure drop in the shell side of the hollow fiber module with respect to draw flow rate. [Note: feed flow rate = 2L/min and DS out pressure = 20bar]

5.3.2.2 Effect of Module Length (L)

In another aspect, the increase in module length for fixed membrane surface area is expected to have high DS and FS pressure drop, and that resulted in reduced net hydraulic power generation. For example, as shown in Figure 5-3 (b) and (d), the net power generation decreased from 40 to 20 W while changing L from 0.3 to 0.56 m. This result provides insight into how to fix the lower bound of module length based on limitation from module fabrication and PRO module installation practice in the actual PRO plant, and the optimum length is always expected to be near to lower bound. As shown in Figure 5-5, after providing a sufficient FS flow rate (for the given module length), further increment in the FS flow rate will reduce the net power generation. This reduction could be due to the rise in energy consumption by the FS pump. Therefore, in this study, the PRO HF module length will be taken as a decision variable to assess its impact on power generation.

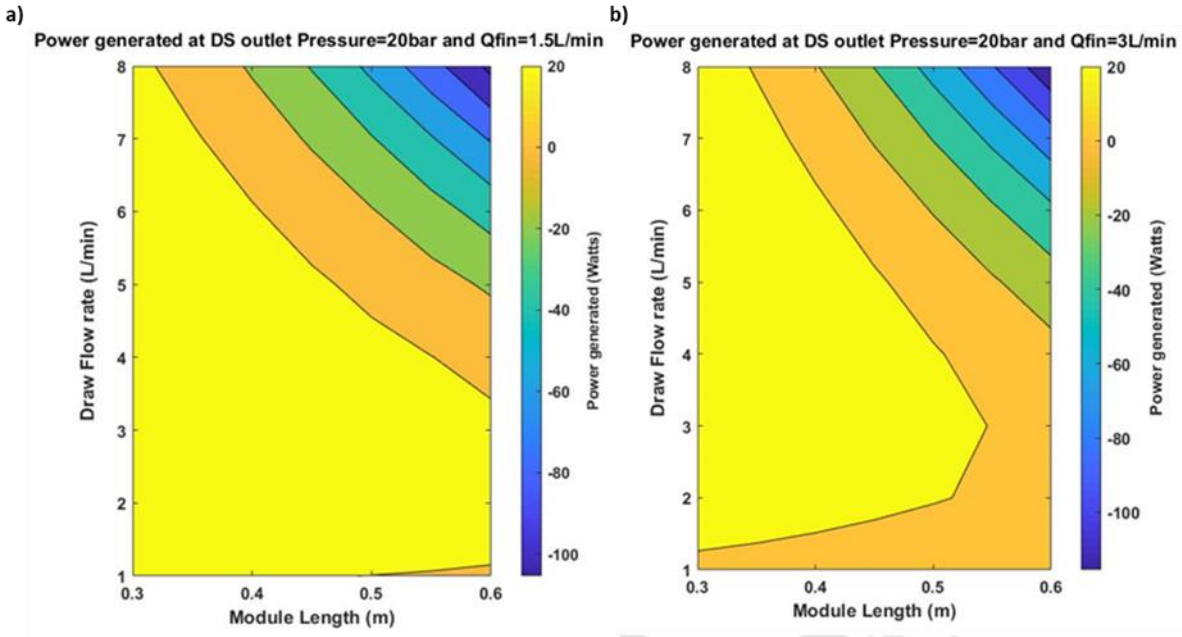

Figure 5-5. Contour plot of net hydraulic power generation at DS outlet pressures of 20 bar and feed flow rate of a) 1.5 L/min and b) 3 L/min

5.3.2.3 Effect of Feed Solution Concentration ($C_{FS,inlet}$)

Feed solution concentration is one of the critical parameters that drive the economics of the PRO process [90]. Considering the limitation in the PRO experimental facility, in our study, the experiments and the respective PRO process optimizations were executed using RO water as FS. However, to elaborate the importance of FS concentration in the PRO process, the impact of FS concentration on water flux and power generation is presented in Figure 5-6. The figure revealed that as the feed concentration increases, both the water flux and power generation declined as a result of a reduction in the driving force. Therefore, for a given PRO application with a fixed FS concentration, the generation of optimal Pareto is a must to implement optimization result into real applications.

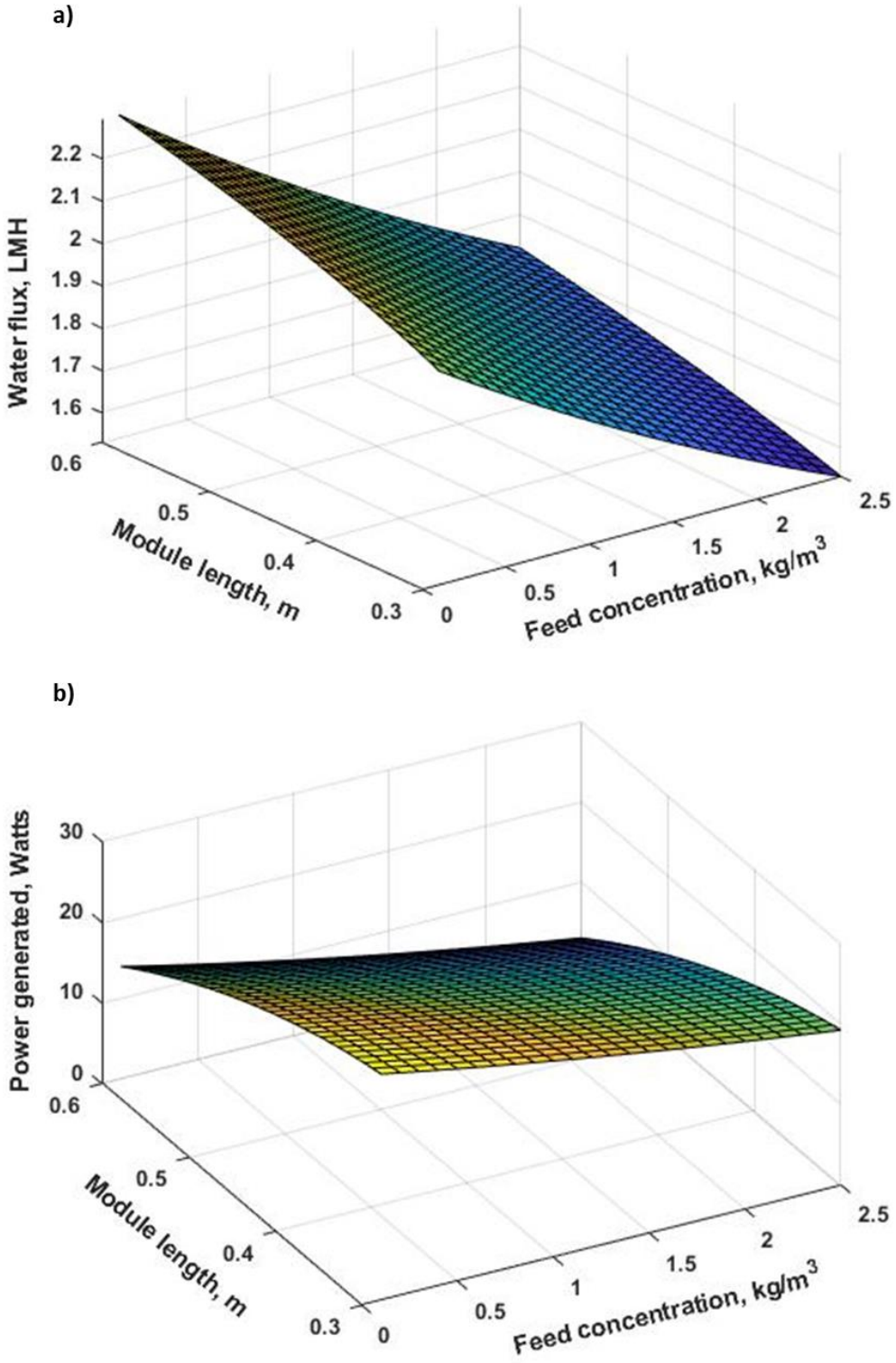

Figure 5-6 Water flux and net hydraulic power generation with respect to feed concentration and module length at $Q_{FS,inlet}$ = 3 L/min and $Q_{DS,inlet}$ = 2 L/min

5.3.2.4 Effect of DS Outlet Pressure

Similarly, as shown in Figure 5-7, the optimum net hydraulic power generation was observed to be increasing, reaching maximum, and then decreasing while increasing the DS outlet pressure. The optimal net hydraulic power generation was observed at DS outlet pressure of 20 bar, which is close to half of the osmotic pressure variation between FS and DS (i.e., $\Delta\Pi$ = 42.4 bar for C_{DS}= 50 kg/m^3). A similar observation is reported in the literature [8,62].

The reason might be due to the decline of (i) pressure drop in the DS side and (ii) the overall driving force between DS and FS. The former tries to improve the net hydraulic power generation, and the latter tries to reduce the net hydraulic power generation. Due to these counter-effects, the optimum net hydraulic power generation point is observed close to 20 bar DS outlet pressure.

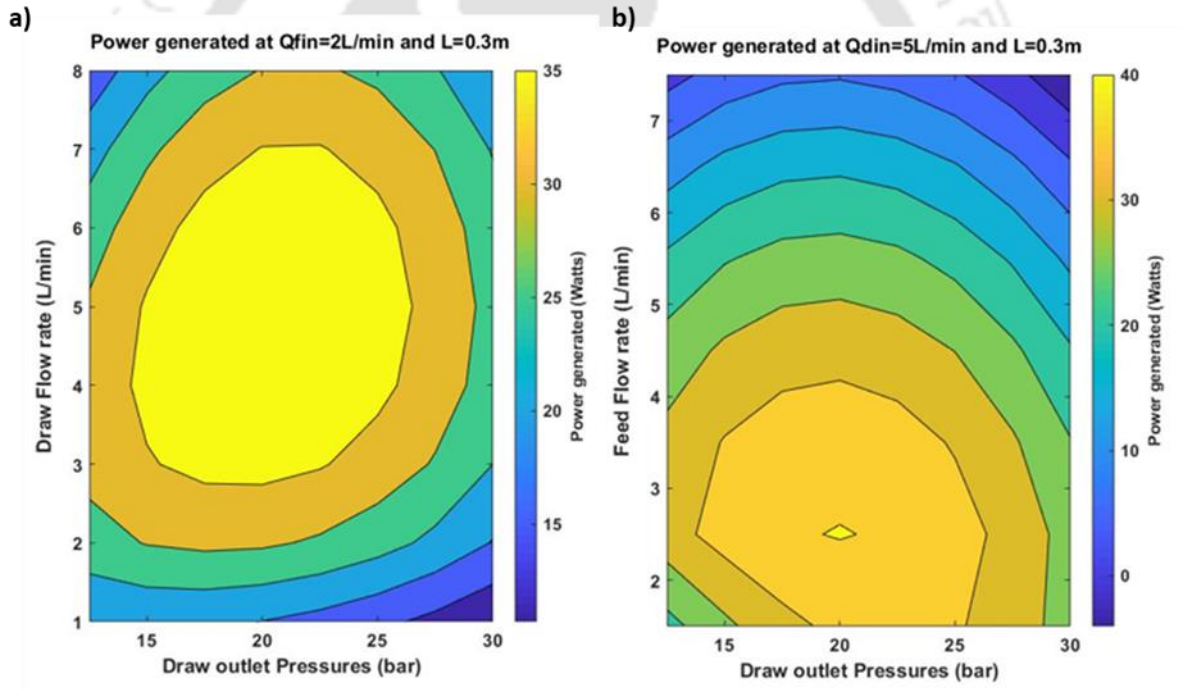

Figure 5-7. Contour plot of net hydraulic power generation at module length of 0.3 m and a) $Q_{FS,inlet}$ = 2 L/min and b) $Q_{DS,inlet}$ = 5 L/min

The contour plot of the net hydraulic power generation function with respect to the PRO module length and operating condition concludes that the power generation by PRO is observed to have a single optimum. Therefore, GA or any deterministic optimization technique is expected to provide the global optimum solution.

5.3.2.5 Permeate Recovery

The recovery of the FS is one of the vital parameters to regulate the fouling at the feed side. The high recovery might lead to severe fouling at the rear end of the HF lumen side. Therefore, the recovery of the FS was calculated using the simulation conditions described in the previous section, along with two DS concentrations (refer to Figure 5-8). As explained earlier, the recovery of the system was increasing when the FS flow rate was decreased. The improved FS flowrate had very minimal improvement in the water flux. But while increasing the DS flow rate, the water flux is expected to increase and reach an asymptotic value due to reduced DS dilution. Correspondingly, the recovery was increasing and moved towards asymptotic value with respect to DS flowrate. When the DS concentration increases, the driving force for the water permeation will increase, and the resultant recovery depicted in Figure 5-8 (a) and (b).

As it can be observed from the simulation results, the optimization of the design parameter (L) and operating conditions (flow rates and DS outlet pressures) are essential to achieve optimum power generation. This requires a well-defined objective function using the decision variables mentioned above.

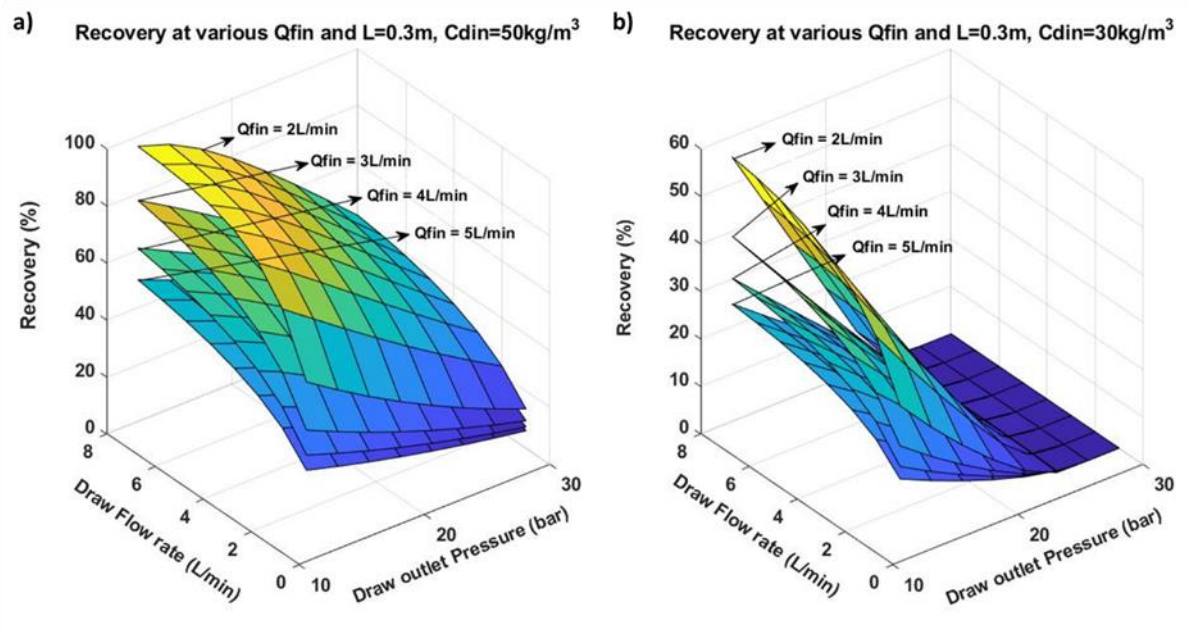

Figure 5-8. The Effect of draw flow rate and DS Outlet Pressure on the percentage recovery at DS concentration of (a) 50 kg/m^3 and (b) 30 kg/m^3

5.3.3 Optimization Studies on the HF-PRO module

Maximizing the net hydraulic power generation per unit $Q_{FS,inlet}$ (Eq. 5.15) with respect to the decision variable ($P_{DS,inlet}$, $Q_{DS,inlet}$, $P_{FS,inlet}$, $Q_{FS,inlet}$, module length, and λ) is one of the main objectives of this work. The result of this optimization is then compared with the optimization results based on Eq. 5.16 and Eq. 5.17. Thus, to find out the optimum results, the optimization problems presented in section 5.1.5 are solved as described in Figure C. 1 (refer to appendix). The flow chart illustrates the inclusive method where $P_{FS,inlet}$, and $P_{DS,inlet}$ are estimated based on the $P_{FS,outlet}$, and $P_{DS,outlet}$. Therefore, the pressure at the DS outlet, which will be directed to the turbine and pressure exchanger, can be tuned, and the estimated DS inlet pressure can be used for power calculation. The pressure at the FS outlet is set to a minimal value (~0.02 bar).

The optimization of the power generation per unit $Q_{FS,inlet}$ was carried out by manipulating draw and feed solution flow rates [L/min], DS outlet pressure [bar], module length [m], and λ as decision variables. The following lower and upper bounds were used for the decision variables:

$$0.5 \le Q_{DS,inlet} \le 8 \quad 0.5 \le Q_{FS,inlet} \le 8 \quad 10 \le P_{DS,outlet} \le 30 \quad 0.3 \le L \le 0.56 \quad 0.01 \le \lambda \le 0.99$$

Moreover, the concentrations of DS and FS were kept at 36 kg/m^3 and 0.338 kg/m^3, respectively, to replicate the Indian seawater [125,126] and river water (refer to Table C. 2 in appendix) salinity conditions. The genetic algorithm (GA) was first used to solve the optimization problem. The GA parameters were fixed as follows: population size = 100, maximum number of iterations = 100, crossover fraction = 0.8 and mutation operator = gaussian. The termination criteria were set based on the change in the objective function value in two consecutive steps, fixed to be less than 1 x 10^{-6}. Also, to confirm whether the result obtained from GA is global optima or not, the same problem was solved by using both Nelder–Mead method and SQP (Sequential Quadratic Programming) optimization techniques available in MATLAB.

When Eq. 5.15 was used as objective function, all the three optimization techniques gave the same optimum power generation per unit $Q_{FS,inlet}$ of 4.16 W/(L/min) at Q_{DS_inlet} = 1.13 L/min, Q_{FS_inlet} = 1.05 L/min, P_{DS_outlet} = 14.80 bar, module length = 0.3 m, and λ = 0.61. And, at this points the value of Q_{DS_outlet} = 1.69 L/min, P_{DS_inlet} = 14.89 bar, and P_{FS_inlet} = 0.31 bar. The power density for the optimized flow conditions was 0.45 W/m^2. The net power generated per unit $Q_{FS,inlet}$ with respect to the module length (0.3-0.56 m) is given in Figure C. 3 (refer to appendix). This figure revealed that for a fixed membrane area, shorter length and bigger diameter HF module provide improved power generation per $Q_{FS,inlet}$ due to lower pressure drop in the module. For example, the optimized net power generation is improved by 46.8 % (from 2.18 to 4.16 W/(L/min)) by reducing module length from 0.56 m to 0.3 m.

Besides this, the power generation was also maximized using the objective function given in Eq. 5.16 and Eq. 5.17. While optimizing second objective Eq. 5.16, the following optimal results were found: power generation = 4.48 W, power density = 0.44 W/m^2 at Q_{DS_inlet} = 1.07 L/min, Q_{FS_inlet} = 1.13 L/min, P_{DS_outlet} = 13.02 bar, module length = 0.3 m, and λ = 0.56. However, the power generation per unit $Q_{FS,inlet}$ based on Eq. 5.16 was 3.96 W/(L/min), which is less than the previous (Eq. 5.15) result (4.16 W/(L/min)). When the objective function (Eq. 5.17), which is based on

power density was used the following results were found at the optimal conditions: power density = 0.78 W/m^2, power generation = 0.0021 W at Q_{DS_inlet} = 3.32 L/min, Q_{FS_inlet} = 1.84 L/min, P_{DS_outlet} = 14.19 bar, module length = 0.3 m, and λ = 0.69. Even though high PRO power density was achieved by optimizing a third objective function, the net power generation per unit $Q_{FS,inlet}$ for the third objective function (Eq.5.17) was 0.0011 W/(L/min), which is less than both the previous objective functions. Therefore, the optimum results based on the first objective function Eq. 5.15, were then used to estimate the Indian blue energy potential using the PRO technology. The comparison among the optimal results of the three objective functions is given in Table C. 4 (refer to appendix).

5.3.4 Estimation of Indian Blue Energy Potential through Optimized Pressure Retarded Osmosis Process

The ten-year average annual water flow rates of major Indian rivers to sea are given in Table 5-4 [127]. Among the thirteen (13) rivers presented in this study, Brahmaputra and Ganga rivers were the two highest flow rivers with annual flow rates of 480.8 x 10^9 and 295.1 x 10^9 m^3/year, respectively. The abundant river water provides suitable conditions for blue energy extraction across the southern peninsula of the Indian sub-continent. In order to assess the feasibility, it is crucial to estimate the amount of blue energy that can be extracted using the optimized PRO process. This requires a mathematical model development, validation, and optimization of the operating conditions of the HF PRO module, which are covered in the previous section. In this section, the optimized conditions at river water ($C_{FS,inlet}$ = 0.338 kg/m^3) and seawater ($C_{DS,inlet}$ = 36 kg/m^3) were used to estimate the net power generated.

In this study, while estimating the net power production from the PRO process, the efficiency of the turbine, pressure exchanger, and pumps are assumed to be 95, 98, and 85 %, respectively [76,128,129]. The permeate produced in the PRO process is used for net power generation in the turbine and balance the power requirement by DS, FS, and pretreatment system. As shown in Figure 5-1, the part of the DS outlet

stream was used for power generation, and the remaining DS was used for pressurizing the DS inlet stream by coupling with a pressure exchanger and high-pressure pump. Using the optimized PRO conditions, the calculated total power generation from the PRO process was 15.52 W. However, the net power output from the PRO process was reduced after deducting the net power consumed by the FS and DS inlet pumps and pretreatment system pumps [76]. These factors were incorporated to estimate the net power generated by the PRO process. The net power consumed by the DS pump was 2.56 W, as 23.12 W was energy exchanged by the pressure exchanger from DS out to DS in (refer to Table C. 3). The integration of a pressure exchanger in the PRO process can enable a direct hydraulic energy exchange between the DS outlet and the inlet stream with minimal energy loss. The net power consumed by the FS pump was estimated 0.02 W, respectively. Further, to account for the power consumption by the pretreatment system, the micro-filtration process was considered as a pretreatment technology for both DS and FS [60,76,130–134]. If a pressure requirement of 2.0 bar is assumed for the pretreatment, then the DS and FS pumps require 4.45 W and 4.13 W, respectively. Hence, the net power generation by the PRO process was reduced to 4.37 W.

To estimate the power generation potential by the Indian major rivers, an analogy has been formulated from $Q_{FS,inlet}$. If Q_{FS_inlet} = 1.0543 L/min can generate a net power of 4.365 W, then 1m^3 of river water can potentially generate 0.07 kWh. Accordingly, the net power generation for all the rivers was estimated and depicted in Table 5-4. The total net power generation for all the thirteen Indian rivers was estimated to be 67.36 TWh/year. However, the well-known Indian perennial rivers such as Brahmaputra, Ganga, and Teesta are discharged outside the Indian coastal area. Hence, deducting the possible power generating by these three rivers gives a net power of 12.34 TWh/year, which is equal to 4.72 % of the Indian renewable power generation capacity during the 2018-19 fiscal year, i.e., 261.7 TWh/year [135].

Table 5-4. Power estimation of the major Indian rivers

S. No.	Rivers	Name of State	Average Annual Flow of River 10 Years from 2009 to 2019		Net power generation	Is discharge within Indian territory?
			MCM	x 10^9 m^3	TWh/year	
1	Brahmaputra	Assam	480798	480.80	33.18	No
2	Ganga	West Bengal	295114	295.11	20.36	No
3	Godavari	Andhra Pradesh	74015	74.02	5.11	Yes
4	Mahanadi	Odisha	43867	43.87	3.03	Yes
5	Teesta	West Bengal	21413	21.41	1.48	No
6	Narmada	Gujarat	14759	14.76	1.02	Yes
7	Brahmani	Odisha	14254	14.25	0.98	Yes
8	Krishna	Andhra Pradesh	10848	10.85	0.75	Yes
9	Subernrekha	Jharkhand	6812	6.81	0.47	Yes
10	Cauvery	Tamilnadu	4573	4.57	0.32	Yes
11	Baitarni	Odisha	3974	3.97	0.27	Yes
12	Mahi	Gujarat	3784	3.78	0.26	Yes
13	Sabarmati	Gujarat	1892	1.89	0.13	Yes
				Total	67.36	

Note: Year has been taken as Water Year from June to May

MCM: million cubic meters

Source: Department of Water Resources, River Development & Ganga Rejuvenation, Government of India Lok Sabha [136]

5.4 Summary

In this chapter, a mathematical model was successfully developed for the PRO process using the axial flow HF FO membrane module. The model output and the experimental results were used to estimate the membrane parameters. The estimated parameters were validated using another set of experimental data. The mathematical model developed in this work was capable of calculating the net hydraulic power generation by the PRO process. Also, the PRO model was simulated to study the sensitivity of the PRO process operating condition and module length by calculating the net hydraulic power generation from the PRO process. The minimization of pressure drop across the HF module was found to be one of the critical parameters to maximize the PRO hydraulic power generation. Initially, the Ergun equation and Hagen Poiseuille equation were used to calculate the pressure drop in the shell and lumen side of the module. However, the applicability of the Ergun equation and Hagen-Poiseuille equation for estimating the pressure drop on the shell and lumen side, respectively, were experimentally investigated. Unfortunately, both equations were underpredicting the actual pressure drop in the module. Hence, both equations were modified in this work. Among the three objective functions considered in this work, the objective function with net energy generation per unit river water supply (Eq. 5.15) was capable of providing an overall optimized solution for the integrated PRO+ERD system. In another aspect, the maximization of power density or net power density alone may lead to a sub-optimal solution for the integrated PRO+ERD system. The net power generation by mixing the Indian river and seawater was estimated to be 12.34 TWh/year, which is equal to 4.72 % of the Indian renewable power generation capacity during the 2018-19 fiscal year.

Chapter 6 Conclusions and Scope of Future Work

Conclusions and Suggestions

This chapter presents the main conclusions that can be drawn from the detailed experimental investigation, modeling, and optimization studies covered in this thesis. It also provides some suggestions towards the scope for future research.

6.1 Conclusions

6.1.1 Uncertainty Analysis in Forward Osmosis Membrane Characterization Using Test Cell

A mathematical model for the FO process was developed by combining the model equation for the following components: membrane transport, concentration polarization, and unsteady state tank mass balance. In this study, evaporation loss from the solution tank is incorporated in the unsteady-state tank mass balance equations. The variations in mass and concentration of FS and DS were used to estimate the FO membrane mass transport parameters. Based on the experimental and simulation analysis, the following observations were made:

- In the FO membrane characterization experiments using the open circulatory system, neglecting the evaporation loss from the solution tank could add significant errors in the estimated membrane transport parameters. Hence, its effect should be considered when calculating the solvent and reverse solute fluxes.
- The proposed model equations were able to predict the mass and concentration variations of solutions in the tank with maximum relative errors of 0.37 and 5.69 %, respectively.
- The estimated parameters of the steady-state model were found to have maximum deviations of 390.5 and −6.9 % in the solvent and solute permeability, respectively, in comparison to the parameters estimated using the unsteady state model in the presence of evaporation losses.

- The incorporation of evaporation loss and the dynamic nature of DS properties in the FO model equation could reduce the overall error in the estimated membrane transport parameters.
- Compared to FS, DS-based measurements could help in reducing the uncertainties of the flux measurement and the errors in the corresponding estimated membrane transport parameters in the presence of evaporation loss for high flux FO experiments.

6.1.2 Experimentation, Modeling, and Optimization Studies on Axial Flow Hollow Fiber Forward Osmosis Module

A mathematical model was successfully developed for the axial flow HF FO membrane module. The model, along with the experimental results, was used to estimate the membrane parameters. The estimated parameters were validated using another set of experimental data. The validated model was then used for simulation and optimization study at various module lengths and operating conditions (pressure and flow rate of DS and FS). The main findings of this work are summarized below

- An optimum trade-off between the FO water flux and power consumption was found compulsory to ensure the economic feasibility of the FO process. Moreover, a two-step procedure was developed to find the optimal design and operational condition of the FO process.
- The simulation results indicated that the length of the module plays an important role in the performance of the HF FO module, and at the optimum length, the draw solution flow rate was found to be a major contributor to the FO water flux.
- The minimum energy consumption per unit permeate volume (SEC = 0.23 MJ/m^3) of this module was observed at the lowest permeate flow rate (0.97 L/min), and the maximum SEC (1.06 MJ/m^3) was observed at the highest permeate flow rate (1.52 L/min).

- The optimal Pareto showed that when the FO water flux increases, the corresponding optimal power requirement increases exponentially. Hence, the optimum point should be derived based on the cost of energy and permeate flow rate.
- The optimization study revealed that the shorter module length provided better FO performance. But in situations where the net energy spent per unit permeate has to be kept as small as possible, a slightly larger module with a low DS flowrate can be considered. The best approach is to fix the module length as minimum as possible based on the module fabrication limitation.
- There is a minimum threshold for DS flow rate and a maximum threshold for FS flow rate, which have to be maintained to obtain an optimal permeate recovery.

6.1.3 Experimentation, Modeling, and Optimization Studies on Axial Flow Hollow Fiber Pressure Retarded Osmosis Module

A mathematical model was successfully developed for the PRO process using the commercial HF FO module. Based on the experimental and simulation analysis, the following observations were made:

- The pressure drop in the shell and lumen side were found to be more than the pressure drop estimated by the standard Ergun and Hagen-Poiseuille equation, respectively.
- The model developed in this study was able to predict the DS and FS concentration, water permeation, and DS outlet pressure with an average percentile error of less than 9.5%, and the FS outlet pressure with an average percentile error of ~17.2%.
- Based on the simulation results, the DS flow rate, DS outlet pressure and module length were found to be the main performance-limiting factors of the HF PRO module.

- The energy consumption (pumping) of FS bounds the upper limit of FS flow rate while the lower limit is set by the minimum FS flow required for adequate permeation and reduced fouling.
- Among the three objective functions considered in this work, the objective function with net energy generation per unit river water supply (Eq. 30) was capable of providing an overall optimized solution for the integrated PRO+ERD system. In another aspect, the maximization of power density or net power density alone may lead to a sub-optimal solution for the integrated PRO+ERD system.
- The optimized condition for the HF PRO module using $C_{DS,inlet}$ = 36 kg/m^3 and $C_{FS,inlet}$ = 0.338 kg/m^3 was found at $Q_{DS,inlet}$ = 1.13 L/min, $Q_{FS,inlet}$ = 1.05 L/min, DS outlet pressure = 14.80 bar, module length = 0.30 m, and λ = 0.61.
- Module length is one of the important variables to maximize the power generation, i.e., for a fixed membrane area, shorter length and bigger diameter HF module provide improved power generation per $Q_{FS,inlet}$ due to lower pressure drop in the module.
- The optimization result revealed that the lower bound of the module length was observed to be the optimal length to achieve maximum energy from the PRO process. Therefore, the best approach is to fix the module length as minimum as possible based on the module fabrication limitation.
- The net power generation by mixing the Indian river and seawater is estimated to be 12.34 TWh/year, which is equal to 4.72 % of the Indian renewable power generation capacity during the 2018-19 fiscal year, i.e., 261.7 TWh/year.

6.2 Overview and Suggestions for Future Works

In this work, the membrane surface area and porosity were maintained constant in the simulation and optimization studies by modifying the shell side diameter and number of fibers. However, the membrane surface area is expected to vary when the

module length varies. Also, fixing the porosity will affect the pressure drop in the shell side, which in turn affects the pumping power requirement.

Thus, in further investigations, the effect of HF module porosity on power consumption, FO water flux, and PRO net hydraulic power generation should be incorporated to obtain the best possible results.

- It was observed in this study that the lumen side pressure drop was 2.5 times greater than the value estimated by the Hagen-Poiseuille equation. Hence, further investigation is required to estimate the overall impact of the HF diameter on FO and PRO performance.
- The shell side pressure drop for the axial flow hollow fibers module is estimated by modifying the Ergun equation. Hence, further investigation is required to establish a well-known equation that will take care of the shell side pressure drop for the axial flow HF module.
- While estimating the Indian blue energy potential through the optimized HF PRO process, the viability in terms of cost was overlooked. Therefore, further investigation is required regarding the techno-economics analysis for the net hydraulic power generation.

In addition to the errors that arise during membrane characterization experiments, such as the uncertainties related to water evaporation, solution volume, and concentration, the non-ideality of NaCl in water should have been considered. The non-idealities assumption in a solution due to electrolytes might influence the osmotic pressure and density estimation in the model. Hence, neglecting the non-ideality of the solution due to electrolyte might contribute some fraction (maybe a very small fraction) to the total error. However, this must be confirmed with additional experiments. Hence, further investigation is required to confirm the same.

Moreover, in this study, the temperature of both FS and DS were fixed while studying the effect of water evaporation on the performance of the FO process. Thus, additional studies are required to assess the impact of varying the solution temperature on water evaporation.

References

[1] Y.C. Kim, M. Elimelech, Potential of osmotic power generation by pressure retarded osmosis using seawater as feed solution: Analysis and experiments, J. Memb. Sci. 429 (2013) 330–337. https://doi.org/10.1016/j.memsci.2012.11.039.

[2] S. Qianhong, J. Xue, T.C. Y., Osmotic power production from salinity gradient resource by pressure retarded osmosis: Effects of operating conditions and reverse solute diffusion, J. Memb. Sci. 401–402 (2012) 262–273. https://doi.org/http://dx.doi.org/10.1016/j.memsci.2012.02.014.

[3] T.Y. Cath, M. Elimelech, J.R. McCutcheon, R.L. McGinnis, A. Achilli, D. Anastasio, A.R. Brady, A.E. Childress, I. V. Farr, N.T. Hancock, J. Lampi, L.D. Nghiem, M. Xie, N.Y. Yip, Standard Methodology for Evaluating Membrane Performance in Osmotically Driven Membrane Processes, Desalination. 312 (2013) 31–38. https://doi.org/10.1016/j.desal.2012.07.005.

[4] D. Xiao, C.Y. Tang, J. Zhang, W.C.L. Lay, R. Wang, A.G. Fane, Modeling salt accumulation in osmotic membrane bioreactors: Implications for FO membrane selection and system operation, J. Memb. Sci. 366 (2011) 314–324. https://doi.org/10.1016/j.memsci.2010.10.023.

[5] D. Attarde, M. Jain, K. Chaudhary, S.K. Gupta, Osmotically driven membrane processes by using a spiral wound module - Modeling, experimentation and numerical parameter estimation, Desalination. 361 (2015) 81–94. https://doi.org/10.1016/j.desal.2015.01.025.

[6] S. Qianhong, J. Xue, L. Qinghua, T.C. Y., Relating reverse and forward solute diffusion to membrane fouling in osmotically driven membrane processes, Water Res. 46 (2012) 2478–2486. https://doi.org/10.1016/j.watres.2012.02.024.

[7] J.R.. M.E. Mccutcheon, Modeling Water Flux in Forward Osmosis: Implications for Improved Membrane Design, AIChE J. 53 (2007) 1736–1744. https://doi.org/10.1002/aic.11197.

[8] A. Achilli, A.E. Childress, Pressure retarded osmosis: From the vision of Sidney Loeb to the first prototype installation - Review, Desalination. 261 (2010) 205–211. https://doi.org/10.1016/j.desal.2010.06.017.

[9] T.Y. Cath, A.E. Childress, M. Elimelech, Forward osmosis: Principles, applications, and recent developments, J. Memb. Sci. 281 (2006) 70–87. https://doi.org/10.1016/j.memsci.2006.05.048.

[10] Z. Shuaifei, Z. Linda, T.C. Y., M. Dennis, Recent developments in forward osmosis: Opportunities and challenges, J. Memb. Sci. 396 (2012) 1–21. https://doi.org/http://dx.doi.org/10.1016/j.memsci.2011.12.023.

[11] T.-S. Chung, S. Zhang, K.Y. Wang, J. Su, M.M. Ling, Forward osmosis processes: Yesterday, today and tomorrow, Desalination. 287 (2012) 78–81. https://doi.org/10.1016/j.desal.2010.12.019.

[12] C. Klaysom, T.Y. Cath, T. Depuydt, I.F.J. Vankelecom, Forward and pressure retarded osmosis: potential solutions for global challenges in energy and water supply, Chem. Soc. Rev. 42 (2013) 6959. https://doi.org/10.1039/c3cs60051c.

[13] W.A. Phillip, J.D. Schiffman, M. Elimelech, High Performance Thin-Film Membrane, Environ. Sci. Technol. 44 (2010) 3812–3818. https://doi.org/10.1021/es1002555.

[14] J.R. McCutcheon, R.L. McGinnis, M. Elimelech, A novel ammonia-carbon dioxide forward (direct) osmosis desalination process, Desalination. 174 (2005) 1–11. https://doi.org/10.1016/j.desal.2004.11.002.

[15] L. SIDNEY, Production of energy from concentrated brines by pressure-retarded osmosis, J. Memb. Sci. 1 (1976) 49–63. https://doi.org/10.1016/S0376-7388(00)82257-7.

[16] A. Ali, Z. Guillermo, S. Adel, Pressure retarded osmosis for power generation and seawater desalination: Performance analysis, Desalination. 344 (2014) 108–115. https://doi.org/http://dx.doi.org/10.1016/j.desal.2014.03.022.

[17] A. Achilli, T.Y. Cath, A.E. Childress, Power generation with pressure retarded osmosis: An experimental and theoretical investigation, J. Memb. Sci. 343 (2009) 42–52. https://doi.org/10.1016/j.memsci.2009.07.006.

[18] A. Achilli, T.Y. Cath, E.A. Marchand, A.E. Childress, The forward osmosis membrane bioreactor: A low fouling alternative to MBR processes, Desalination. 238 (2009) 10–21. https://doi.org/10.1016/j.desal.2008.02.022.

[19] A.. Lee, H. Nikraz, BOD: COD Ratio as an Indicator for River Pollution, Int.

Proc. Chem. Biol. Environ. Eng. 51 (2015) 139–142. https://doi.org/10.7763/IPCBEE.

[20] A. Altaee, G. Zaragoza, H.R. van Tonningen, Comparison between Forward Osmosis-Reverse Osmosis and Reverse Osmosis processes for seawater desalination, Desalination. 336 (2014) 50–57. https://doi.org/10.1016/j.desal.2014.01.002.

[21] R.K. McGovern, J.H. Lienhard V, On the potential of forward osmosis to energetically outperform reverse osmosis desalination, J. Memb. Sci. 469 (2014) 245–250. https://doi.org/10.1016/j.memsci.2014.05.061.

[22] S. Qianhong, W.Y.K. Willis, Z. Shuaifei, T.C. Y., Organic fouling in pressure retarded osmosis: Experiments, mechanisms and implications, J. Memb. Sci. 428 (2013) 181–189. https://doi.org/10.1016/j.memsci.2012.10.045.

[23] G. Han, J. Zhou, C. Wan, T. Yang, T.S. Chung, Investigations of inorganic and organic fouling behaviors, antifouling and cleaning strategies for pressure retarded osmosis (PRO) membrane using seawater desalination brine and wastewater, Water Res. 103 (2016) 264–275. https://doi.org/10.1016/j.watres.2016.07.040.

[24] D. Attarde, M. Jain, S.K. Gupta, Modeling of a forward osmosis and a pressure-retarded osmosis spiral wound module using the Spiegler-Kedem model and experimental validation, Sep. Purif. Technol. 164 (2016) 182–197. https://doi.org/10.1016/j.seppur.2016.03.039.

[25] B. Jiao, A. Cassano, E. Drioli, Recent advances on membrane processes for the concentration of fruit juices: A review, J. Food Eng. 63 (2004) 303–324. https://doi.org/10.1016/j.jfoodeng.2003.08.003.

[26] E.M. Garcia-Castello, J.R. McCutcheon, M. Elimelech, Performance evaluation of sucrose concentration using forward osmosis, J. Memb. Sci. 338 (2009) 61–66. https://doi.org/10.1016/j.memsci.2009.04.011.

[27] R.W. Holloway, A.E. Childress, K.E. Dennett, T.Y. Cath, Forward osmosis for concentration of anaerobic digester centrate, Water Res. 41 (2007) 4005–4014. https://doi.org/10.1016/j.watres.2007.05.054.

[28] T.Y. Cath, S. Gormly, E.G. Beaudry, M.T. Flynn, V.D. Adams, A.E. Childress,

Membrane contactor processes for wastewater reclamation in space: Part I. Direct osmotic concentration as pretreatment for reverse osmosis, J. Memb. Sci. 257 (2005) 85–98. https://doi.org/10.1016/j.memsci.2004.08.039.

[29] R.E. Kravath, J.A. Davis, Desalination of sea water by direct osmosis, Desalination. 16 (1975) 151–155. https://doi.org/10.1016/S0011-9164(00)82089-5.

[30] D. Cohen, C. Ross, Mixing moves osmosis technology forward, Chem. Process. 67 (2004) 29–32. https://www.chemicalprocessing.com/articles/2004/346/.

[31] A. Tiraferri, N.Y. Yip, A.P. Straub, S. Romero-Vargas Castrillon, M. Elimelech, A method for the simultaneous determination of transport and structural parameters of forward osmosis membranes, J. Memb. Sci. 444 (2013) 523–538. https://doi.org/10.1016/j.memsci.2013.05.023.

[32] S. Senthilmurugan, S.K. Gupta, Modeling of a radial flow hollow fiber module and estimation of model parameters for aqueous multi-component mixture using numerical techniques, J. Memb. Sci. 279 (2006) 466–478. https://doi.org/10.1016/j.memsci.2005.12.041.

[33] A. Chatterjee, A. Ahluwalia, S. Senthilmurugan, S.K. Gupta, Modeling of a radial flow hollow fiber module and estimation of model parameters using numerical techniques, J. Memb. Sci. 236 (2004) 1–16. https://doi.org/10.1016/j.memsci.2004.01.006.

[34] M. Sekino, Study of an analytical model for hollow fiber reverse osmosis module systems, Desalination. 100 (1995) 85–97. https://doi.org/10.1016/0011-9164(96)00010-0.

[35] K.J. Kim, A.G. Fane, R. Ben Aim, M.G. Liu, G. Jonsson, I.C. Tessaro, A.P. Broek, D. Bargeman, A comparative study of techniques used for previous termporous membrane characterization: pore characterization, J. Memb. Sci. 87 (1994) 35–46. https://doi.org/10.1016/0376-7388(93)E0044-E.

[36] J.R. McCutcheon, R.L. McGinnis, M. Elimelech, Desalination by ammonia-carbon dioxide forward osmosis: Influence of draw and feed solution concentrations on process performance, J. Memb. Sci. 278 (2006) 114–123. https://doi.org/10.1016/j.memsci.2005.10.048.

[37] W.J. Jakobs, E., & Koros, Ceramic membrane characterization via the bubble point technique, J. Memb. Sci. 124 (1997) 149–159. https://doi.org/10.1016/S0376-7388(96)00203-7.

[38] W. Phillip, J.S. Yong, M. Elimelech, Reverse Draw Solute Permeation in Forward Osmosis: Modeling and Experiments, Environ. Sci. Technol. 44 (2010) 5170–5176. https://doi.org/10.1021/es100901n.

[39] J. Wei, C. Qiu, C. Tang, R. Wang, A.F.-J. of M. Science, U. 2011, Synthesis and characterization of flat-sheet thin film composite forward osmosis membranes, J. Memb. Sci. 372 (2011) 292–302. https://doi.org//10.1016/j.memsci.2011.02.013.

[40] B. Gu, D.Y. Kim, J.H. Kim, D.R. Yang, Mathematical model of flat sheet membrane modules for FO process: Plate-and-frame module and spiral-wound module, J. Memb. Sci. 379 (2011) 403–415. https://doi.org/10.1016/j.memsci.2011.06.012.

[41] Z. Shan, G. Yangshuo, X. Dezhong, T.C. Y., The role of physical and chemical parameters on forward osmosis membrane fouling during algae separation, J. Memb. Sci. 366 (2011) 356–362. https://doi.org/10.1016/j.memsci.2010.10.030.

[42] K.P. Lee, T.C. Arnot, D. Mattia, A review of reverse osmosis membrane materials for desalination — Development to date and future potential, J. Memb. Sci. 370 (2011) 1–22. https://doi.org/10.1016/j.memsci.2010.12.036.

[43] S.S. Shenvi, A.M. Isloor, a. F. Ismail, A review on RO membrane technology: Developments and challenges, Desalination. 368 (2015) 10–26. https://doi.org/10.1016/j.desal.2014.12.042.

[44] B. Peñate, L. García-Rodríguez, B. Penate, L. Garcia-Rodriguez, Current trends and future prospects in the design of seawater reverse osmosis desalination technology, Desalination. 284 (2012) 1–8. https://doi.org/10.1016/j.desal.2011.09.010.

[45] R. Sabry, A.G. Gadallah, S.S. Ali, H.M. Ali, H. Gadallah, Application of forward/reverse osmosis hybrid system for brackish water desalination using El-Salam canal water, Sinai, Egypt, Part (2): Pilot scale investigation, Int. J. ChemTech Res. 8 (2015) 102–112.

[46] L. Setiawan, R. Wang, K. Li, A.G. Fane, Fabrication of novel poly(amide-imide) forward osmosis hollow fiber membranes with a positively charged nanofiltration-like selective layer, J. Memb. Sci. 369 (2011) 196–205. https://doi.org/10.1016/j.memsci.2010.11.067.

[47] J. Su, Q. Yang, J.F. Teo, T.S. Chung, Cellulose acetate nanofiltration hollow fiber membranes for forward osmosis processes, J. Memb. Sci. 355 (2010) 36–44. https://doi.org/10.1016/j.memsci.2010.03.003.

[48] K.Y. Wang, T.S. Chung, J.J. Qin, Polybenzimidazole (PBI) nanofiltration hollow fiber membranes applied in forward osmosis process, J. Memb. Sci. 300 (2007) 6–12. https://doi.org/10.1016/j.memsci.2007.05.035.

[49] R. Wang, L. Shi, C.Y. Tang, S. Chou, C. Qiu, A.G. Fane, Characterization of novel forward osmosis hollow fiber membranes, J. Memb. Sci. 355 (2010) 158–167. https://doi.org/10.1016/j.memsci.2010.03.017.

[50] S.A. Muztuza, J. Eun, S. Phuntsho, A. Jang, J. Young, H. Kyong, Forward osmosis system analysis for optimum design and operating conditions, Water Res. 145 (2018) 429–441. https://doi.org/10.1016/j.watres.2018.08.050.

[51] J. Eun, S. Phuntsho, S. Muztuza, J. Young, H. Kyong, Forward osmosis membrane modular configurations for osmotic dilution of seawater by forward osmosis and reverse osmosis hybrid system, Water Res. 128 (2018) 183–192. https://doi.org/10.1016/j.watres.2017.10.042.

[52] Y. Tanaka, M. Yasukawa, S. Goda, H. Sakurai, M. Shibuya, T. Takahashi, M. Kishimoto, M. Higa, H. Matsuyama, Experimental and simulation studies of two types of 5-inch scale hollow fiber membrane modules for pressure-retarded osmosis, Desalination. 447 (2018) 133–146. https://doi.org/10.1016/j.desal.2018.09.015.

[53] M. Shibuya, M. Yasukawa, S. Goda, H. Sakurai, T. Takahashi, M. Higa, H. Matsuyama, Experimental and theoretical study of a forward osmosis hollow fiber membrane module with a cross-wound configuration, J. Memb. Sci. 504 (2016) 10–19. https://doi.org/10.1016/j.memsci.2015.12.040.

[54] Y. Lv, X. Yu, S.T. Tu, J. Yan, E. Dahlquist, Experimental studies on simultaneous removal of CO2and SO2in a polypropylene hollow fiber

membrane contactor, Appl. Energy. 97 (2012) 283–288. https://doi.org/10.1016/j.apenergy.2012.01.034.

[55] J.R. McCutcheon, M. Elimelech, Influence of concentrative and dilutive internal concentration polarization on flux behavior in forward osmosis, J. Memb. Sci. 284 (2006) 237–247. https://doi.org/10.1016/j.memsci.2006.07.049.

[56] D. Xiao, W. Li, S. Chou, R. Wang, C.Y. Tang, A modeling investigation on optimizing the design of forward osmosis hollow fiber modules, J. Memb. Sci. 392–393 (2012) 76–87. https://doi.org/10.1016/j.memsci.2011.12.006.

[57] R. Valladares Linares, Z. Li, V. Yangali-Quintanilla, N. Ghaffour, G. Amy, T. Leiknes, J.S. Vrouwenvelder, Life cycle cost of a hybrid forward osmosis - low pressure reverse osmosis system for seawater desalination and wastewater recovery, Water Res. 88 (2016) 225–234. https://doi.org/10.1016/j.watres.2015.10.017.

[58] G. Blandin, A.R.D. Verliefde, C.Y. Tang, P. Le-Clech, Opportunities to reach economic sustainability in forward osmosis-reverse osmosis hybrids for seawater desalination, Desalination. 363 (2015) 26–36. https://doi.org/10.1016/j.desal.2014.12.011.

[59] S.E. Skilhagen, Osmotic power - a new, renewable energy source, Desalin. Water Treat. 15 (2010) 271–278. https://doi.org/10.5004/dwt.2010.1759.

[60] N.Y. Yip, M. Elimelech, Thermodynamic and energy efficiency analysis of power generation from natural salinity gradients by pressure retarded osmosis, Environ. Sci. Technol. 46 (2012) 5230–5239. https://doi.org/10.1021/es300060m.

[61] S. Chou, R. Wang, A.G. Fane, Robust and High performance hollow fiber membranes for energy harvesting from salinity gradients by pressure retarded osmosis, J. Memb. Sci. 448 (2013) 44–54. https://doi.org/10.1016/j.memsci.2013.07.063.

[62] N.Y. Yip, A. Tiraferri, W.A. Phillip, J.D. Schiffman, L.A. Hoover, Y.C. Kim, M. Elimelech, Thin-film composite pressure retarded osmosis membranes for sustainable power generation from salinity gradients, Environ. Sci. Technol. 45 (2011) 4360–4369. https://doi.org/10.1021/es104325z.

[63] H. Gang, Z. Sui, L. Xue, C. Tai-Shung, Progress in pressure retarded osmosis (PRO) membranes for osmotic power generation, Prog. Polym. Sci. 51 (2015) 1–27. https://doi.org/10.1016/j.progpolymsci.2015.04.005.

[64] C.F. Wan, T.S. Chung, Osmotic power generation by pressure retarded osmosis using seawater brine as the draw solution and wastewater retentate as the feed, J. Memb. Sci. 479 (2015) 148–158. https://doi.org/10.1016/j.memsci.2014.12.036.

[65] S. Sarp, Z. Li, J. Saththasivam, Pressure Retarded Osmosis (PRO): Past experiences, current developments, and future prospects, Desalination. 389 (2016) 2–14. https://doi.org/10.1016/j.desal.2015.12.008.

[66] S. Chou, R. Wang, L. Shi, Q. She, C. Tang, A.G. Fane, Thin-film composite hollow fiber membranes for pressure retarded osmosis (PRO) process with high power density, J. Memb. Sci. 389 (2012) 25–33. https://doi.org/10.1016/j.memsci.2011.10.002.

[67] Y.C. Kim, Y. Kim, D. Oh, K.H. Lee, Experimental investigation of a spiral-wound pressure-retarded osmosis membrane module for osmotic power generation, Environ. Sci. Technol. 47 (2013) 2966–2973. https://doi.org/10.1021/es304060d.

[68] Y. Xu, X. Peng, C.Y. Tang, Q.S. Fu, S. Nie, Effect of draw solution concentration and operating conditions on forward osmosis and pressure retarded osmosis performance in a spiral wound module, J. Memb. Sci. 348 (2010) 298–309. https://doi.org/10.1016/j.memsci.2009.11.013.

[69] M. Higa, D. Shigefuji, M. Shibuya, S. Izumikawa, Y. Ikebe, M. Yasukawa, N. Endo, A. Tanioka, Experimental study of a hollow fiber membrane module in pressure-retarded osmosis: Module performance comparison with volumetric-based power outputs, Desalination. 420 (2017) 45–53. https://doi.org/10.1016/j.desal.2017.06.015.

[70] T.S. Han, G., Zuo, J., Wan, C. and Chung, Hybrid pressure retarded osmosis–membrane distillation (PRO–MD) process for osmotic power and clean water generation, Environ. Sci. Water Res. Technol. 1 (2015) 507–515. https://doi.org/10.1039/c5ew00127g.

[71] M. Lin, S., Yip, N.Y., Cath, T.Y., Osuji, C.O. and Elimelech, Hybrid Pressure Retarded Osmosis−Membrane Distillation System for Power Generation from Low-Grade Heat: Thermodynamic Analysis and Energy Efficiency, Environ. Sci. Technol. 48 (2014) 5306–5313. https://doi.org/10.1021/es405173b.

[72] H.W. Chung, J. Swaminathan, L.D. Banchik, J.H. Lienhard, Economic framework for net power density and levelized cost of electricity in pressure-retarded osmosis, Desalination. 448 (2018) 13–20. https://doi.org/10.1016/j.desal.2018.09.007.

[73] H. Teklu, D.K. Gautam, S. Subbiah, Axial flow hollow fiber forward osmosis module analysis for optimum design and operating conditions in desalination applications, Chem. Eng. Sci. 216 (2020) 115494. https://doi.org/10.1016/j.ces.2020.115494.

[74] D.K. Gautam, H. Teklu, S. Subbiah, Analysis of reverse osmosis process in hollow fiber module with and without secondary permeate outlet, J. Water Process Eng. 36 (2020) 101336. https://doi.org/10.1016/j.jwpe.2020.101336.

[75] A. Ansari, M. Abbaspour, Modelling and economic evaluation of pressure-retarded osmosis power plant case study: Iran, Int. J. Ambient Energy. 40 (2019) 69–81. https://doi.org/10.1080/01430750.2017.1354323.

[76] Q.A. Khasawneh, B. Tashtoush, A. Nawafleh, B. Kan'an, Techno-economic feasibility study of a hypersaline pressure-retarded osmosis power plants: Dead sea–red sea conveyor, Energies. 11 (2018). https://doi.org/10.3390/en11113118.

[77] B. Tylkowski, I. Tsibranska, Overview of main techniques used for membrane characterization, J. Chem. Technol. Metall. 50 (2015) 3–12.

[78] L. Fortunato, N. Pathak, Z. Ur Rehman, H. Shon, T.O. Leiknes, Real-time monitoring of membrane fouling development during early stages of activated sludge membrane bioreactor operation, Process Saf. Environ. Prot. 120 (2018) 313–320. https://doi.org/10.1016/j.psep.2018.09.022.

[79] L. Zheng, D. Yu, G. Wang, Z. Yue, C. Zhang, Y. Wang, J. Zhang, J. Wang, G. Liang, Y. Wei, Characteristics and formation mechanism of membrane fouling in a full-scale RO wastewater reclamation process: Membrane autopsy and

fouling characterization, J. Memb. Sci. 563 (2018) 843–856. https://doi.org/10.1016/j.memsci.2018.06.043.

[80] W. Chen, C. Qian, K.G. Zhou, H.Q. Yu, Molecular Spectroscopic Characterization of Membrane Fouling: A Critical Review, Chem. 4 (2018) 1492–1509. https://doi.org/10.1016/j.chempr.2018.03.011.

[81] T. Ruprakobkit, L. Ruprakobkit, C. Ratanatamskul, Carboxylic acid concentration by forward osmosis processes: Dynamic modeling, experimental validation and simulation, Chem. Eng. J. 306 (2016) 538–549. https://doi.org/10.1016/j.cej.2016.07.091.

[82] M. Al-Shammiri, Evaporation rate as a function of water salinity, Desalination. 150 (2002) 189–203. https://doi.org/10.1016/S0011-9164(02)00943-8.

[83] A.M. Salhotra, E.E. Adams, D.R.F. Harleman, The alpha, beta, gamma of evaporation from saline water bodies, Water Resour. Res. 23 (1987) 1769–1774. https://doi.org/10.1029/WR023i009p01769.

[84] A. Salman, M.A. Al-Shammiri, New Computational Intelligence model for predicting evaporation rates for saline water, Desalination. 214 (2007) 273–286. https://doi.org/10.1016/j.desal.2006.11.011.

[85] ForwardOsmosisTech, (2014). https://www.forwardosmosistech.com/the-4-different-designs-of-forward-osmosis-fo-membrane-modules/.

[86] C. Bhattacharjee, V.K. Saxena, S. Dutta, Fruit juice processing using membrane technology: A review, Innov. Food Sci. Emerg. Technol. 43 (2017) 136–153. https://doi.org/10.1016/j.ifset.2017.08.002.

[87] Richard W. Baker, Membrane technology and Applications, Wiley A John Wiley & Sons, Ltd., Publication, 2012.

[88] M. Sekino, Precise analytical model of hollow fiber reverse osmosis modules, J. Memb. Sci. 85 (1993) 241–252. https://doi.org/10.1016/0376-7388(93)85278-5.

[89] M. Shibuya, M. Yasukawa, T. Takahashi, T. Miyoshi, M. Higa, H. Matsuyama, Effect of operating conditions on osmotic-driven membrane performances of cellulose triacetate forward osmosis hollow fiber membrane, Desalination. 362 (2015) 34–42. https://doi.org/10.1016/j.desal.2015.01.031.

[90] S. Senthil, S. Senthilmurugan, Reverse Osmosis-Pressure Retarded Osmosis hybrid system: Modelling, simulation and optimization, Desalination. 389 (2016) 78–97. https://doi.org/10.1016/j.desal.2016.01.027.

[91] Y.G. Park, K. Chung, I.H. Yeo, W.I. Lee, T.S. Park, Development of a SWRO-PRO hybrid desalination system: Pilot plant investigations, Water Sci. Technol. Water Supply. 18 (2018) 473–481. https://doi.org/10.2166/ws.2017.115.

[92] C.F. Wan, T.-S. Chung, Techno-economic evaluation of various RO+PRO and RO+FO integrated processes, Appl. Energy. 212 (2018) 1038–1050. https://doi.org/10.1016/j.apenergy.2017.12.124.

[93] J. Benjamin, M.E. Arias, Q. Zhang, A techno-economic process model for pressure retarded osmosis based energy recovery in desalination plants, Desalination. 476 (2020). https://doi.org/10.1016/j.desal.2019.114218.

[94] K. Touati, H.S. Usman, C.N. Mulligan, M.S. Rahaman, Energetic and economic feasibility of a combined membrane-based process for sustainable water and energy systems, Appl. Energy. 264 (2020) 114699. https://doi.org/10.1016/j.apenergy.2020.114699.

[95] B. Blankert, Y. Kim, H. Vrouwenvelder, N. Ghaffour, Facultative hybrid RO-PRO concept to improve economic performance of PRO: Feasibility and maximizing efficiency, Desalination. 478 (2020). https://doi.org/10.1016/j.desal.2019.114268.

[96] M. Kishimoto, Y. Tanaka, M. Yasukawa, S. Goda, M. Higa, H. Matsuyama, Optimization of Pressure-Retarded Osmosis with Hollow-Fiber Membrane Modules by Numerical Simulation, Ind. Eng. Chem. Res. 58 (2019) 6687–6695. https://doi.org/10.1021/acs.iecr.9b00139.

[97] R. Long, X. Lai, Z. Liu, W. Liu, Pressure retarded osmosis: Operating in a compromise between power density and energy efficiency, Energy. 172 (2019) 592–598. https://doi.org/10.1016/j.energy.2019.01.169.

[98] H. Wang, Y. Wang, D. Ma, Q. Zhang, S. Xu, Optimization on the operating conditions of pro process: Towards improved net power density, Desalin. Water Treat. 114 (2018) 19–30. https://doi.org/10.5004/dwt.2018.22316.

[99] Y. Chen, A.A. Alanezi, J. Zhou, A. Altaee, M.H. Shaheed, Optimization of

module pressure retarded osmosis membrane for maximum energy extraction, J. Water Process Eng. 32 (2019) 100935. https://doi.org/10.1016/j.jwpe.2019.100935.

[100] W. Yang, L. Song, J. Zhao, Y. Chen, B. Hu, Numerical analysis of performance of ideal counter-current flow pressure retarded osmosis, Desalination. 433 (2018) 41–47. https://doi.org/10.1016/j.desal.2017.12.058.

[101] A. Altaee, A. Cippolina, Modelling and optimization of modular system for power generation from a salinity gradient, Renew. Energy. 141 (2019) 139–147. https://doi.org/10.1016/j.renene.2019.03.138.

[102] M. Li, Optimization of multi-stage hybrid RO-PRO membrane processes at the water–energy nexus, Chem. Eng. Res. Des. 137 (2018) 1–9. https://doi.org/10.1016/j.cherd.2018.06.042.

[103] T. Holt, W. Thelin, G. Brekke, Modelling mass transport in hollow fibre membranes used for pressure retarded osmosis, J. Memb. Sci. 417–418 (2012) 69–79. https://doi.org/10.1016/j.memsci.2012.06.014.

[104] W. He, Y. Wang, M.H. Shaheed, Modelling of osmotic energy from natural salt gradients due to pressure retarded osmosis: Effects of detrimental factors and flow schemes, J. Memb. Sci. 471 (2014) 247–257. https://doi.org/10.1016/j.memsci.2014.08.002.

[105] P.M. Pardeshi, A.A. Mungray, A.K. Mungray, Determination of optimum conditions in forward osmosis using a combined Taguchi-neural approach, Chem. Eng. Res. Des. 109 (2016) 215–225. https://doi.org/10.1016/j.cherd.2016.01.030.

[106] Y. Wang, W. He, H. Zhu, Computational fluid dynamics (CFD) based modelling of osmotic energy generation using pressure retarded osmosis (PRO), Desalination. 389 (2016) 98–107. https://doi.org/10.1016/j.desal.2016.02.002.

[107] A. Sagiv, W. Xu, P.D. Christofides, Y. Cohen, R. Semiat, Evaluation of osmotic energy extraction via FEM modeling and exploration of PRO operational parameter space, Desalination. 401 (2017) 120–133. https://doi.org/10.1016/j.desal.2016.09.015.

[108] G.D. Mehta, S. Loeb, Internal polarization in the porous substructure of a semipermeable membrane under pressure-retarded osmosis, J. Memb. Sci. 4 (1978) 261–265. https://doi.org/10.1016/S0376-7388(00)83301-3.

[109] C.Y. Tang, Q. She, W.C.L. Lay, R. Wang, A.G. Fane, Coupled effects of internal concentration polarization and fouling on flux behavior of forward osmosis membranes during humic acid filtration, J. Memb. Sci. 354 (2010) 123–133. https://doi.org/10.1016/j.memsci.2010.02.059.

[110] C.H. Tan, H.Y. Ng, Modified models to predict flux behavior in forward osmosis in consideration of external and internal concentration polarizations, J. Memb. Sci. 324 (2008) 209–219. https://doi.org/10.1016/j.memsci.2008.07.020.

[111] G. Schock, A. Miquel, Mass transfer and pressure loss in spiral wound modules, Desalination. 64 (1987) 339–352. https://doi.org/10.1016/0011-9164(87)90107-X.

[112] S.K. Murthy, Z. V. P., & Gupta, Estimation of mass transfer coefficient using a combined nonlinear membrane transport and film theory model, Desalination. 109 (1997) 39–49. https://doi.org/10.1016/S0011-9164(97)00051-9.

[113] X. Zhang, J. Tian, Z. Ren, W. Shi, Z. Zhang, Y. Xu, S. Gao, F. Cui, High performance thin-film composite (TFC) forward osmosis (FO) membrane fabricated on novel hydrophilic disulfonated poly(arylene ether sulfone) multiblock copolymer/polysulfone substrate, J. Memb. Sci. 520 (2016) 529–539. https://doi.org/10.1016/j.memsci.2016.08.005.

[114] C. Rowher, Evaporation from free water surface., US Dep. Agric. Coop. with Color. Agric. Exp. Station. Tech. Bull. 271 (1931) 96–101.

Appendix

Appendix A

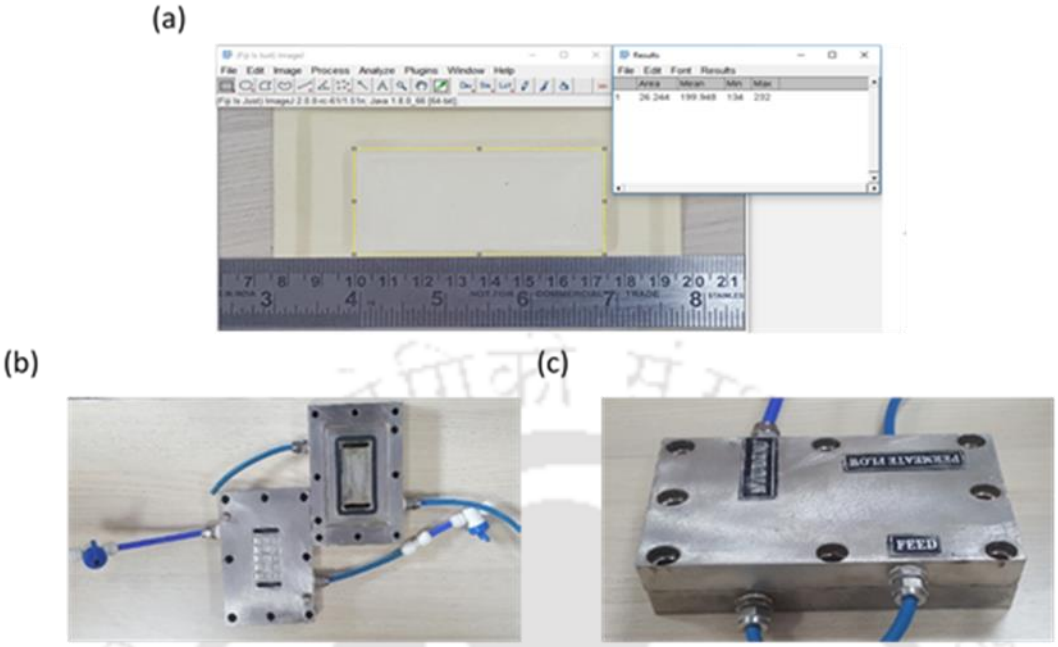

Figure A. 1. (a) Flat sheet membrane with ruler for measuring the active area, (b) membrane test cell when open, and (c) membrane test cell when closed

Table A. 1. The accuracy of measuring devices used in this study

Measuring devise	Parameter	Unit	Accuracy	Range
Micro-Flo flow meter	Flow rate	mL/min	± 6 %	100 – 5000
Eutech CON 700	Concentration	mS	± 1 %	0 – 200
Virgo	Mass	g	± 1 g	0 – 10,000

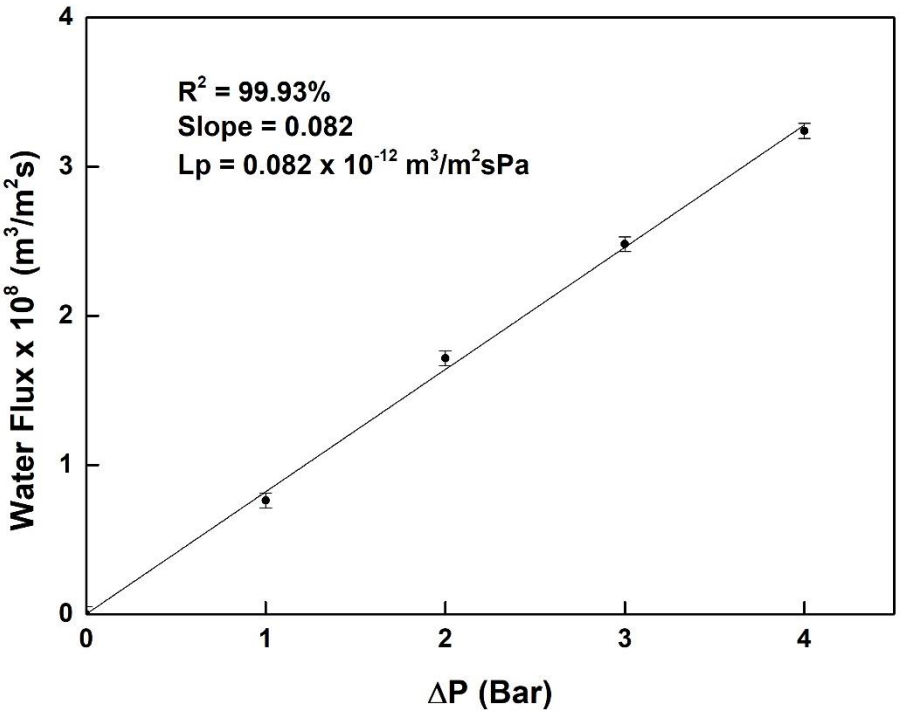

Figure A. 2. Water permeability coefficient estimation using RO mode

Appendix B

Table B. 1. The accuracy of measuring devices used in this study

Measuring device	Parameter	Unit	Accuracy	Range
Digital pressure gauge	Pressure	Psi	± 0.25 %	0 - 400
PP helical flow meter	Flow rate	L/h	± 0.5 %	0 – 400
Hanna HI5321 conductivity meter	Concentration	µS/cm	± 0.01 %	0 – 10^6
Data logging weighing system	Mass	g	± 0.5 g	0 – 10^4

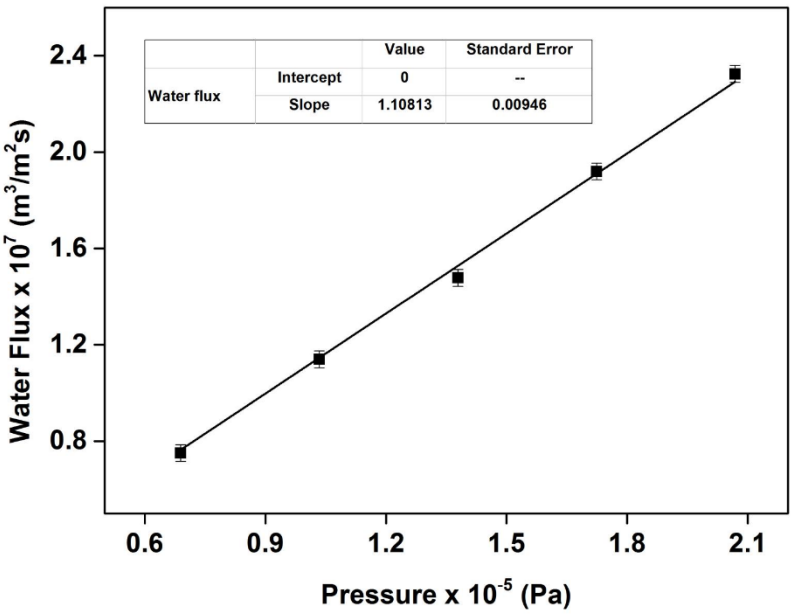

Figure B. 1. Water permeability estimation using distilled water

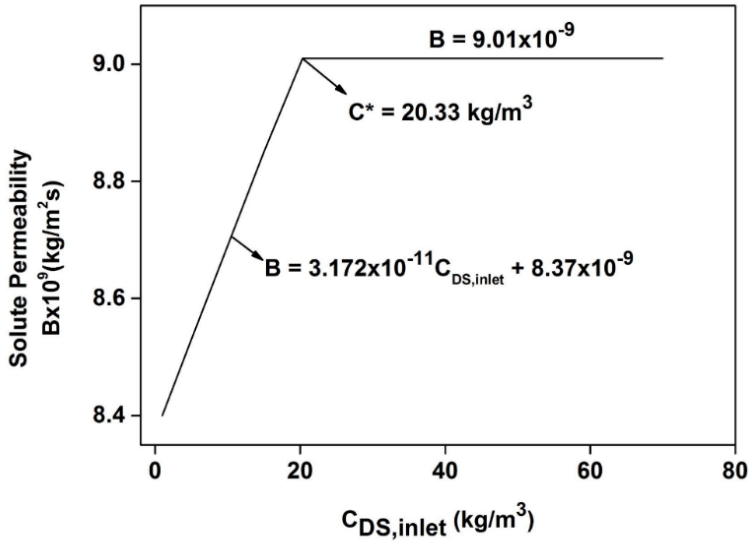

Figure B. 2. Solute permeability with respect to inlet draw solution concentration

Table B. 2. Pressure drop based on Ergun and Modified Ergun equation for different draw solution flow rate ($Q_{DS,inlet}$)

$Q_{DS,inlet}$	$P_{DS,inlet}$	$P_{DS,outlet}$	ΔP	ΔP Based on the Ergun Equation	ΔP Based on Modified Ergun Equation	Error
L/min	bar	bar	bar	bar	bar	%
2.59	3.45	0.29	3.16	0.28	3.15	0.32
2.44	3.10	0.26	2.84	0.26	2.83	0.35
2.29	2.67	0.21	2.46	0.25	2.50	1.63
1.99	2.13	0.17	1.96	0.21	1.93	1.53
1.68	1.54	0.12	1.42	0.18	1.41	0.70
1.38	1.04	0.07	0.97	0.15	0.99	2.06

Note: porosity = 0.4709, viscosity = 0.00089 cP, length = 0.56 and do = 175 µm

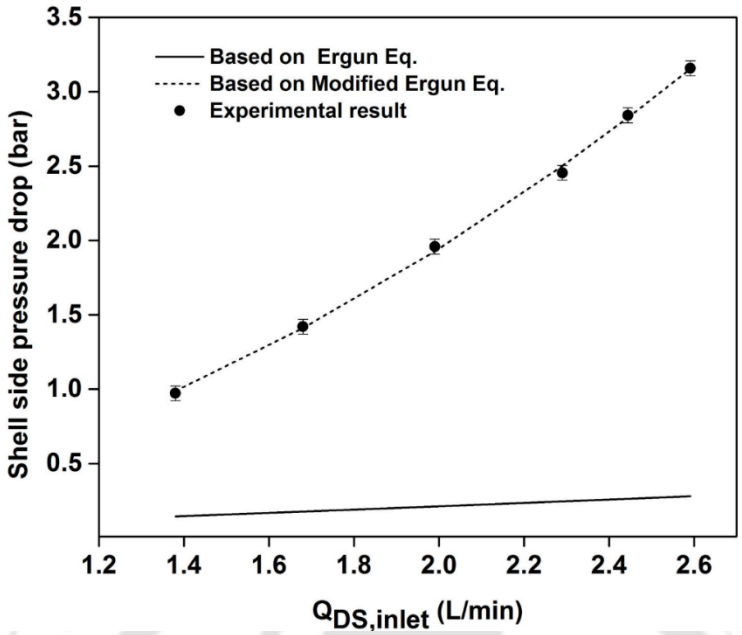

Figure B. 3. Pressure drop comparison based on Ergun and modified Ergun equation for HF module

Appendix C

Table C. 1. The experimental conditions for the HF PRO mode

	units	Shell side	Tube side
Solution type	-	Draw solution	Feed solution
Volume of solution	L	4.2	10
Concentration	kg/m^3	45 and 30	< 0.01
Flow rate	L/min	1.3	2.2
Pressure	bar	8.0	3.0
Temperature of solution	°C	25	25

Table C. 2. TDS summary for Indian major rivers

S. No	River	Minimum TDS (mg/L)	Maximum TDS (mg/L)	Average TDS (mg/L)	Duration	Reference
1	Brahmaputra	6.76	296	97.48	2008 - 2017	RDC-II Office
2	Ganga	52	500	192.36	2008 - 2017	RDC-II Office
3	Godavari	11	1616	217.06	2008 - 2017	RDC-II Office
4	Mahanadi	311.7	2461.3	1386.5	2001 - 2003	[137]
5	Teesta	36.47	84.17	60.32	2018	[138]
6	Narmada	54	513	158.05	2008 - 2017	RDC-II Office
7	Brahmani	74	365.4	219.7	2007 - 2008	[139]
8	Krishna	34.8	1762	427.34	2008 - 2017	RDC-II Office
9	Subernarekha	241	285	263	2012 - 2013	[140]
10	Cauvery	22	529	277.5	2008 - 2017	RDC-II Office
11	Baitarni	74	247	160.5	2014 - 2015	[141]
12	Mahi	116	456	279.23	2008 - 2017	RDC-II Office
13	Sabarmati	141	1168	654.5	1969 - 1978	[142]
	Average	90.36	790.99	337.96		

Source: River Data Compilation II (RDC-II) Directorate, Rama Krishna Puram, New Delhi 110605

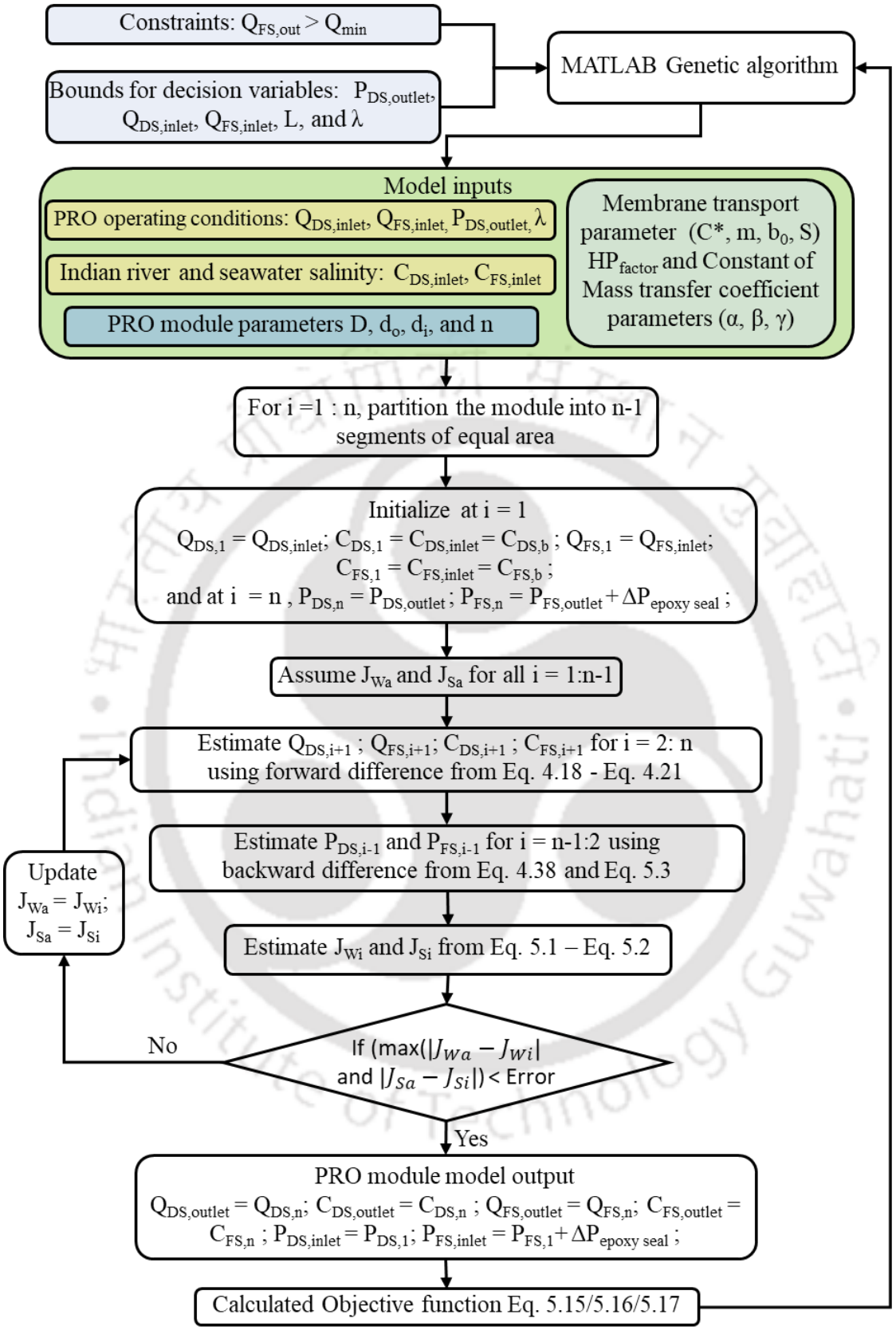

Figure C. 1. Flow chart for solving PRO HF module model equation and process optimization

Pressure drop in shell side

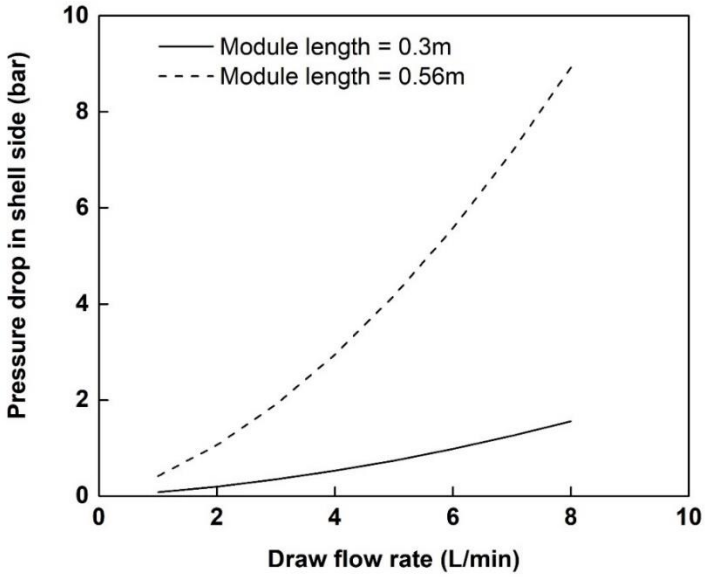

Figure C. 2. Pressure drop in shell side of the hollow fiber module with respect to draw flow rate. [Note: feed flow rate = 2 L/min and DS out pressure = 20 bar]

Table C. 3. Mass-Energy balance at the optimal condition

Location	Flow rate (L/min)	Salinity (kg/m^3)	Pressure (bar)	Stream Energy (W)	Actual Energy (W)	Energy Required (W)	Net Energy Generated (W)
A	1.1336	36	0	0	0		
B	1.1336	36	2.0	3.7787	4.4455	4.4455	
C	1.1336	36	1.5	2.834	2.834		
D	1.1336	36	13.7388	23.1232	23.1232		
E	1.1336	36	14.8901	2.1752	2.559	2.559	
F	1.6879	23.704	14.8041	41.6464	41.6464		
G	1.0256	23.704	14.8041	23.5951	23.1232		
H	1.0256	23.704	1.0	1.7093	1.6751		
I	0.6623	23.704	14.8041	16.342	15.5250		4.365
J	0.6623	23.704	0.1	0.1104	0.1049		
K	1.0543	0.338	0	0	0		
L	1.0543	0.338	2.0	3.5143	4.1345	4.1345	
M	1.0543	0.338	0.3	0.5272	0.5272		
N	1.0543	0.338	0.3101	0.5449	0.0209	0.0209	
O	0.5	2.31	0.016	0.0133	0.0133		
						Net Generated	4.365 W

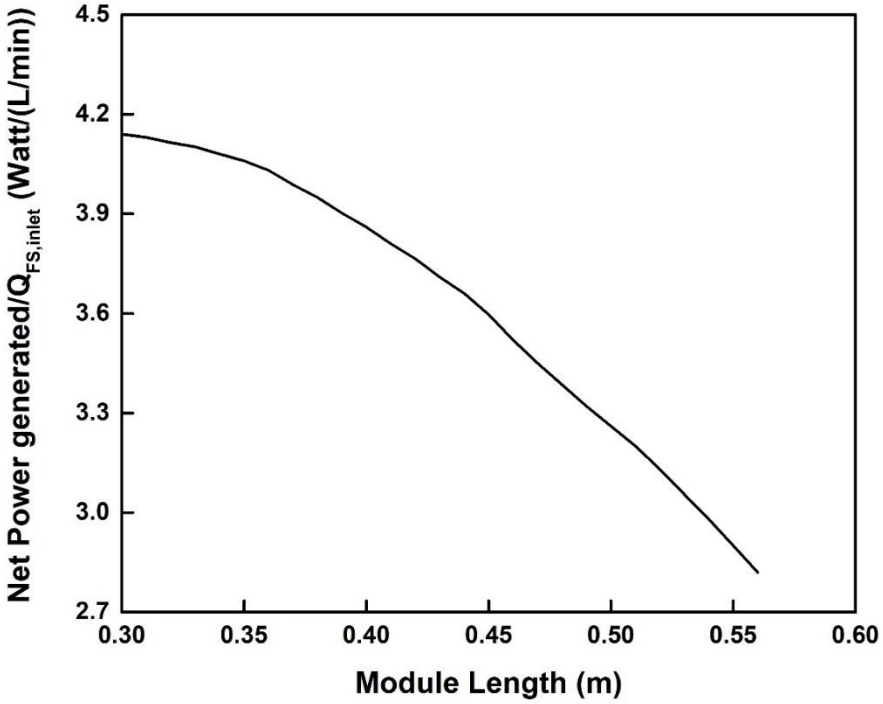

Figure C. 3. The net hydraulic power generated per unit FS inlet flow rate with respect to the module length

Table C. 4. Comparison between the optimal results based on the three objective functions

Objective function	Net Power W	Net power per $Q_{FS,inlet}$ W/(L/min)	Power density W/m^2	L m	λ	$P_{DS,inlet}$ bar	$Q_{DS,inlet}$ L/min	$P_{FS,inlet}$ bar	$Q_{FS,inlet}$ L/min
Eq. 5.15	4.37	4.16	0.45	0.3	0.61	14.89	1.13	0.31	1.05
Eq. 5.16	4.48	3.96	0.44	0.3	0.56	13.1	1.07	0.12	1.13
Eq. 5.17	0.0021	0.0011	0.78	0.3	0.69	14.55	3.22	0.56	1.84

Publications and Conferences

Journals Articles

- **H. Teklu**, D. K. Gautam, and S. Subbiah, Axial flow hollow fiber forward osmosis module analysis for optimum design and operating conditions in desalination applications, Chem. Eng. Sci., vol. 216, p. 115494, 2020 https://doi.org/10.1016/j.ces.2020.115494
- **H. T. Aseffa**, D. K. Gautam, and S. Subbiah, "Optimization of Pressure Retarded Osmosis Process and Estimation of Indian Blue Energy Capacity" p. 114752, 2020 https://doi.org/10.1016/j.desal.2020.114752
- D. K. Gautam, **H. Teklu**, and S. Subbiah, Journal of Water Process Engineering Analysis of reverse osmosis process in hollow fiber module with and without secondary permeate outlet, J. Water Process Eng., vol. 36, no. March, p. 101336, 2020, https://doi.org/10.1016/j.jwpe.2020.101336
- **H. T. Aseffa** and S. Subbiah, Error analysis during forward osmosis membrane characterization in open recirculatory system (Revision-Submitted to Membranes and Membrane Technologies Journal)

International and National Conferences

1. **H. Teklu** and S. Subbiah, Unsteady State Approach for Characterization of Forward Osmosis Membrane and Experimental Error Minimization, presented in Research Conclave March 14-17, 2019 at IIT Guwahati
2. **H. Teklu**, D. K. Gautam, and S. Subbiah, Forward Osmosis Process Using Axial Flow Hollow Fiber Module: Membrane Parameter Estimation, Validation and Simulation Studies, presented in Reflux Sept 28-29, 2019 at IIT Guwahati (First price in oral presentation)
3. **H. Teklu**, D. K. Gautam, and S. Subbiah, Experimentation, modeling, and optimization of axial flow hollow fiber module for forward osmosis process, Poster Accepted at 4th International conference on desalination using membrane technology, Perth, Australia